Dynamic Model Identification and Trajectory Correction for Virtual Process Planning in Multi-Axis Machine Tools

by

Mustafa Hakan Turhan

A thesis
presented to the University of Waterloo
in fulfillment of the
thesis requirement for the degree of
Doctor of Philosophy
in
Mechanical and Mechatronics Engineering

Waterloo, Ontario, Canada, 2019

Examining Committee Membership

The following served on the Examining Committee for this thesis. The decision of the Examining Committee is by majority vote.

External Examiner   Chinedum Okwudire

                                       Associate Professor, Mechanical Engineering

                                       University of Michigan

Supervisor(s)   Kaan Erkorkmaz

                                       Professor, Mechanical and Mechatronics Engineering

                                       University of Waterloo

                                       Baris Fidan

                                       Associate Professor, Mechanical and Mechatronics Engineering

                                       University of Waterloo

Internal Member   Soo Jeon

                                       Associate Professor, Mechanical and Mechatronics Engineering

                                       University of Waterloo

Internal Member   Michael Mayer

                                       Associate Professor, Mechanical and Mechatronics Engineering

                                       University of Waterloo

Internal-external Member   John McPhee

                                       Professor, System Design Engineering

                                       University of Waterloo

Author's Declaration

This thesis consists of material all of which I authored or co-authored: see Statement of Contributions included in the thesis. This is a true copy of the thesis, including any required final revisions, as accepted by my examiners.

I understand that my thesis may be made electronically available to the public.

Statement of Contributions

During the course of this PhD thesis, the author Mustafa Hakan Turhan has collaborated with MASc student Ms. Ginette Tseng. The result of this collaboration has led to one journal paper which is currently under review, and two conference papers which have been presented by the author:

[J1] M. H. Turhan, G. W. Tseng, K. Erkorkmaz, B. Fidan, "Identification of Virtual Machine Tool Feed Drives from In-Process Signals," Submitted to *Mechatronics*, April 2019. Under Review.

[C1] M. H. Turhan, G. W. Tseng, K. Erkorkmaz, B. Fidan, "Identification of Virtual Machine Tool Feed Drives from In-Process Gathered Data," in *Proc. ASPE 2016 Spring Topical Meeting*, April 2016, Boston, MA.

[C2] M. H. Turhan, G. W. Tseng, K. Erkorkmaz, B. Fidan, "Reduced Parameter GMS Friction Model", in *Proc. VMPT 2018 7th International Conference on Virtual Machining Process Technology*, May 2018, Hamilton, ON.

[J1] and [C1] are the publication of the new transfer function identification method presented in Chapter 3. The theory of this method was developed by the author, and experimental results presented from a gear grinding machine were obtained by the author. Additional experimental results reported from a Deckel Maho 80P hi-dyn 5-axis machining center were obtained by Ginette Tseng.

[C2] presents the reduced parameter GMS friction modeling approach proposed in Chapter 4. The theory behind this approach was developed by the author and relevant open loop experiments were also performed by the author. In Chapter 5, this model is integrated with the closed-loop transfer function identification method developed in Chapter 3, and used in the estimation of the machine tool feed drive response from in-process data. These experiments were conducted together with Ginette Tseng, who played the lead role in designing and executing these tests.

In Chapter 5, the integration of the reduced parameter GMS friction model with high-order dynamics identification is investigated. The high order model estimation algorithm and vibratory response measurement experiments had been conducted by Ginette Tseng as part of her MASc thesis. In this PhD thesis, as acknowledged in Chapter 5, this methodology and data have been used to investigate the effectiveness of the reduced parameter GMS friction model, in the context of identifying the positioning response for feed drive systems where both stick-slip friction and vibratory dynamics are present.

The author gratefully acknowledges the above contributions made by Ms. Tseng, which have also positively impacted his PhD research. All other contributions in this thesis were made by the author.

Abstract

In today's industry, the capability to effectively reduce production time and cost gives a manufacturer a vital advantage against its competitors. Specifically, in the machining industry, the ability to simulate the dynamic performance of machine tools, and the physics of cutting processes, is critical to taking corrective actions, achieving process and productivity improvements, thereby enhancing competitiveness. In this context, being able to estimate mathematical models which describe the dynamic response of machine tools to commanded tool trajectories and external disturbance forces plays a key role in establishing virtual and intelligent manufacturing capability. These models can also be used in virtual simulations for process improvement, such as compensating for dynamic positioning errors by making small corrections to the commanded trajectory. This, in turn, can facilitate further productivity improvement and part quality in multi-axis manufacturing operations, such as machining.

This thesis presents new methods for identifying the positioning response and friction characteristics of machine tool servo drives in a nonintrusive manner, and an approach for enhancing dynamic positioning accuracy through commanded trajectory correction via Iterative Learning Control (ILC).

As the first contribution, the linear transfer functions correlating the positioning response to the commanded trajectory and friction disturbance inputs are identified using a new pole search method in conjunction with least squares (LS) projection. It is validated that this approach can work with in-process collected data, and demonstrates superior convergence and numerical characteristics, and model prediction accuracy, compared to an earlier 'rapid identification' approach based on the application of classical Least Squares for the full model. Effectiveness of the new method is demonstrated in simulations, and in experimental case studies for planar motion on two different machine tools, a gear grinding machine and a 5-axis machining center. Compared to the earlier approach, which could predict servo errors with 10-68% closeness, the new method improves the prediction accuracy to 0.5-2%.

In the simulation of feed drives used in multi-axis machines, high fidelity prediction of the nonlinear stick-slip friction plays an important role. Specifically, time-dependent (i.e., dynamic) friction models help to improve the accuracy of virtual predictions. While many elaborate models have been proposed for this purpose, such as the generalized Maxwell-slip (GMS) model, their parameters can be numerous and difficult to identify from limited field data. In this thesis, as the second contribution, a new and highly efficient method of parameterizing the pre-sliding (hysteretic) portion of the GMS friction model

is presented. This approach drastically reduces the number of unknown variables to identify, by estimating only the affective breakaway force, breakaway displacement, and 'shape factor' describing the shape of the pre-sliding virgin curve. Reduction in the number of unknowns enables this 'reduced parameter' GMS model to be identified much more easily from in-process data, compared to the fully parameterized GMS model, and the time-dependent friction dynamics can still be simulated accurately.

Having improved the positioning response transfer function estimation and friction modeling, as the third contribution of this thesis, these two elements are combined together in a 3-step process. First, the servo response is estimated considering simplified Coulomb friction dynamics. Then, the friction model is replaced and identified as a reduced parameter GMS model. In the third step, the transfer function poles and zeros, and the reduced parameter GMS model, are concurrently optimized to replicate the observed experimental response with even greater fidelity. This improvement has been quantified as 12-44% in RMS and 28-54% in MAX values. This approach is successful in servo systems with predominantly rigid body behavior. However, its extension to a servo system with vibratory dynamics did not produce an immediately observed improvement. This is attributed to the dominance of vibrations in response to the commanded trajectory, and further investigation is recommended for future research.

Having an accurate model of a multi-axis machine's feed drive response allows for the dynamic positioning errors, which can lead to workpiece inaccuracy or defects, to be predicted and corrected ahead of time. For this purpose, ILC has been investigated. It is shown that through ILC, 1-2 orders of magnitude reduction in the servo errors is possible. While ILC is already available in certain commercial CNC systems, its training cycle (which is performed during the operation of the machine tool) can lead to part defects and wasted productive machining time. The new idea proposed in this thesis is to perform ILC on a virtual model, which is continuously updated via real-time production data using the identification methods developed in this work. This would minimize the amount of trial and error correction needed on the actual machine.

In the course of this thesis research, after validating the effectiveness of ILC in simulations, to reliably and safely migrate the virtual modeling and trajectory correction results into industry (such as on a gear grinding machine tool), the author initiated and led the design and fabrication of an industry-scale testing platform, comprising a Siemens 840D SolutionLine CNC with a multi-axis feed drive setup. Majority of this implementation has been completed, and in near future work, the dynamic accuracy and productivity improvements facilitated with 'virtually' tuned ILC are expected to be demonstrated experimentally and tested in industry.

Acknowledgments

Dedication

To my beloved wife and daughter.

Table of Contents

List of Figures

List of Tables

Chapter 1
Introduction

1.1.   Background

The principal goal of virtual manufacturing technology is to side-step the labour, capital, and time-intensive stages of machine and process physical prototyping, and to establish new production machinery and/or processes, in which the desired quality, accuracy, and functions are achieved from the very first manufactured part onwards. This concept is illustrated in Fig. 1.1.

Establishing a comprehensive virtual manufacturing system is challenging and requires technical sophistication in terms of developing highly accurate digital (i.e., virtual) models of machinery, processes, and coupling these models (to capture their interactions) inside a digital computation environment. Building an accurate virtual machine tool (VMT) prototype alone requires competence in several technical disciplines, including multi-body dynamics, finite element analysis, modal analysis, sensors, instrumentation, control systems, and trajectory planning algorithms (as conceptually shown in Fig. 1.2). Efforts in this direction have been going on in several research centers across Europe, Asia, and North America over the last two decades, as summarized in [1]. Fully developed VMT prototypes have now just started to emerge.
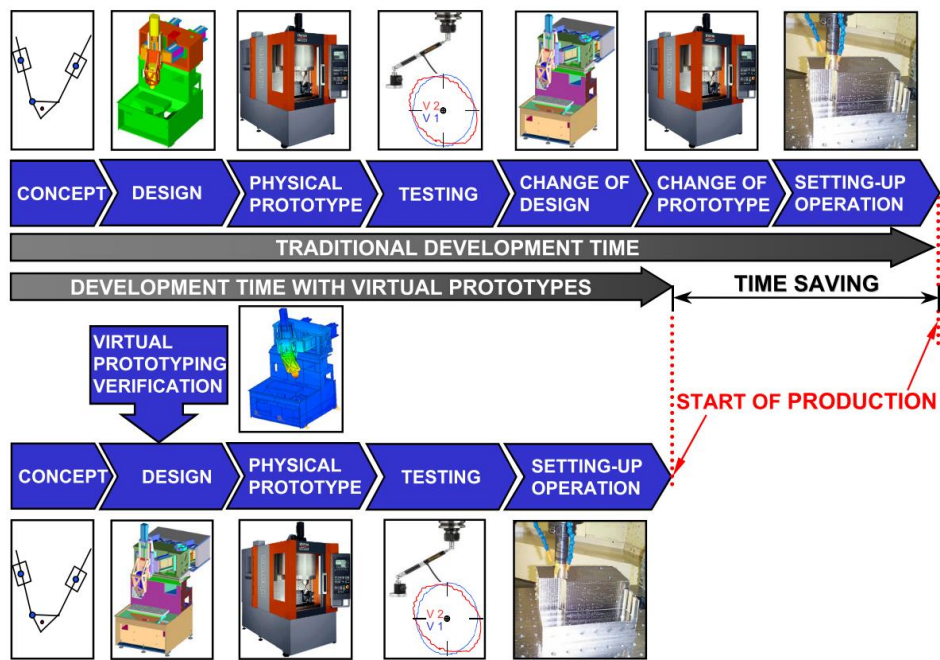
Fig. 1.1. Time savings enabled by Virtual Manufacturing [1].

1
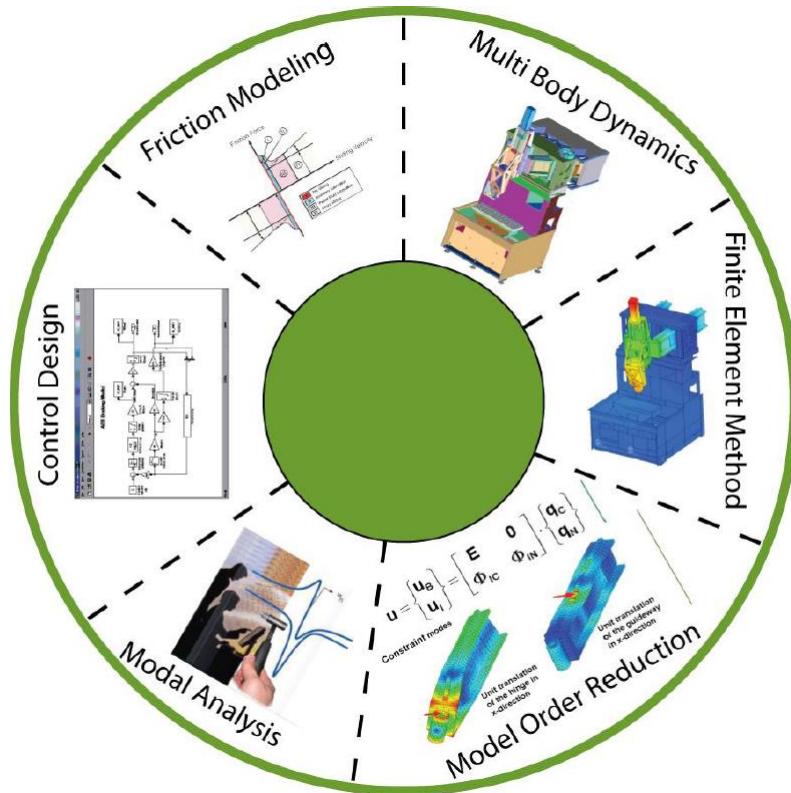
Fig. 1.2. Multi-disciplinary approach followed in Virtual Prototyping of machine tools (Sub-figures from [1]).

Parallel to capturing the dynamics of production machinery, virtual modeling of manufacturing processes is also very important. There have been numerous mathematical models for the processes alone, such as turning [2], milling [3][4], drilling [5], broaching [6], and grinding [7]. Recently, the integration of such models into virtual machine tools has also started to take place, resulting in Virtual Machining Systems (VMS) [8][9]. In VMS, considering the tool positioning relative to the workpiece, a complex workpiece is updated by discretizing and calculating the cutter-workpiece engagement geometry. From this geometry, the material properties, and the tool and workpiece structural transfer functions, it is possible to determine the cutting forces, deformations (i.e. machined surface finish), as well as stable versus unstable (i.e., chatter) machining conditions.

A critical component linking the virtual machine tool (VMT) to a virtual machining system (VMS, i.e. process model) is understanding the instantaneous multi-axis relative motions that are generated between the tool and workpiece at every time instant. These motions are determined by the kinematic structure of the machine tool / tooling / workpiece assembly, the dynamic response of the servo drives to generated trajectory commands and external disturbances (like friction and cutting process forces),

and also the nature of the trajectory inputs that are applied to the servo control system. In an effort to simulate the spatial dynamic response of machine tools considering all of these effects, a Virtual CNC (VCNC) system was proposed in [10]. Correct identification of the feed drive dynamics results in high prediction accuracy by VCNC, and can allow necessary corrective or optimization actions to be taken to further increase throughput and/or part quality. However, accurately identifying feed drive models for machine tools is typically time-consuming, and can also result in loss of productivity while a dedicated machine tool is taken off the production schedule to perform the necessary model building and identification experiments. There have been earlier studies to identify machine tool feed drive models in a nonintrusive manner, as such [11] (i.e., referred to as 'rapid identification'). While successful to a limited extent, these methods deteriorate, especially when measurement signals are noisy.

In this thesis, more robust and effective methods of identifying feed drive models from in-process data are proposed. Specifically, the position tracking and disturbance (i.e., friction) response are estimated, the servo errors that occur due to stick-slip friction at zero-velocity crossings (e.g., toolpath corners and arc quadrants) are predicted more accurately through the use of a new reduced parameter GMS (Generalized Maxwell Slip) friction model. This friction model approximation is first validated in Chapter 4 using a single axis ball-screw drive in open-loop tests, followed by data collected from a linear drive in closed-loop control experiments. Afterwards, in Chapter 5 the reduced parameter GMS friction model parameters are estimated jointly with the tracking and disturbance transfer functions based on in-process data collected from a 5-axis machine tool in closed-loop control. It is demonstrated that such virtual feed drive models can also be used for correcting commanded multi-axis trajectories in a virtual environment using Iterative Learning Control (ILC), thereby freeing up the machine production to continue without trial-and-error based corrective actions.

1.2.   Thesis Overview and Contributions

Chapter 2 presents the literature review. In Chapter 3, the earlier work on non-intrusive 'rapid identification', and the proposed new methodology are presented. Afterwards, comparative results in simulation studies, and experimental data obtained from two industrial machine tools, are presented. It is shown that the proposed new method is highly successful (to 2% accuracy) in predicting servo errors due to trajectory commands. During friction transitions, however, the prediction accuracy degrades due to stick slip friction. While elaborate methods have been proposed to model stick-slip friction, such as the GMS model, the large number of parameters that requires identification hinders their practical use. Thus, in Chapter 4, a new method to characterize the most important (pre-sliding) portion of the GMS

model, using only three parameters, is proposed. Experimental validation of this method, and correlation to earlier data presented in literature, is provided. Chapter 5 combines the new transfer function estimation method with the proposed reduced parameter GMS friction model, and demonstrates that 12-54% further accuracy in servo response prediction is attainable in cases where rigid body dynamics are dominant. Chapter 6 explores the use of ILC for trajectory correction with the estimated virtual models. The conclusions for this thesis are presented in Chapter 7.

The main contributions of this thesis can be listed as follows:

C1. A new approach to formulate and estimate closed-loop models of servo systems by utilizing pole-search in conjunction with least squares projection. The new approach provides better robustness against measurement noise, and also improved convergence of the model parameters.

C2. A reduced parameter approach to capture the pre-sliding dynamics of the generalized Maxwell Slip (GMS) friction model. This approach reduces the number of unknown parameters from $2N$ (N: number of GMS elements, typically $N \geq 6$) to 3. This enables more expedient estimation of friction.

C3. Combination of reduced parameter GMS model with the pole search algorithm for joint estimation of linear dynamics and stick-slip friction, and its experimental validation. This approach yields 12-54% in the prediction accuracy improvement over applying C1 alone.

C4. The use of iterative learning control (ILC) based on estimated virtual models to improve the dynamic positioning accuracy in multi-axis contouring applications. Using ILC with a virtual model rather than the machine's own drive system frees up productivity of the machine. In simulation, ILC predicts 1-2 orders of magnitude improvement, as expected. Experimental implementation of this contribution is on-going.

Chapter 2

Literature Review

2.1.   Introduction

In applications like high-speed finish machining, the process forces are small. Yet, the servo errors, which are influenced largely by the commanded velocity, acceleration, jerk, and the friction, can become significant and cause deterioration of the part accuracy and quality. With the advent of more powerful computers, virtual prototyping and process planning have become viable solutions for the manufacturing community. Using a virtual CNC (VCNC), the process planner can evaluate modifications to a toolpath as well as feed, acceleration, and jerk levels at different points along the part program, in order to obtain the desired tool positioning accuracy while minimizing the motion cycle time. However, in order to obtain accurate predictions, it is critical to have correct models that describe the feed drive dynamics.

In Section 2.2, literature on the modeling and identification for machine tool feed drives is presented. Once a system model is known, corrective and optimizing actions can be taken to enhance productivity and quality outcomes. In this line of thought, Section 2.3 covers Iterative Learning Control (ILC). ILC can be applied to progressively correct for servo errors, which occur in response repeating commanded trajectories. The ability to implement ILC on a virtual model frees up the actual machine's time, enabling process improvements to be achieved without sacrificing productive manufacturing resources.

2.2.   Modeling and Identification of Machine Tool Feed Drives and Structural Assemblies

In this section, the virtual CNC concept, bottom-up approaches for capturing the essential dynamics of the motion delivery (i.e. feed drive) systems through various time- and frequency-domain measurements, and the more efficient albeit relatively closed top-down identification approach are presented.

2.2.1.   Virtual CNC Systems

Accurate simulation of the moving axes of a machine tool is critical for establishing the dynamic interaction between a machine tool and the manufacturing process. In order to meet this objective, the Virtual CNC (VCNC) was developed by the Manufacturing Automation Laboratory at the University of British Columbia (UBC) [10] (Fig. 2.1). The VCNC is a simulation tool that allows users to prototype a real CNC, selecting standard modules out of libraries of trajectory generation algorithms, control

laws, feed drive models, and feedback devices. Using the VCNC, a machine tool's performance can be predicted and enhanced during design, development, and end use stages [10][11]. In addition, this tool is able to simulate different nonlinear effects such as Stribeck friction, amplifier saturation, and quantization errors. Following the design of the VCNC, contour error prediction can be performed and the performance of a machine tool can be optimized for different NC part programs [11][12].
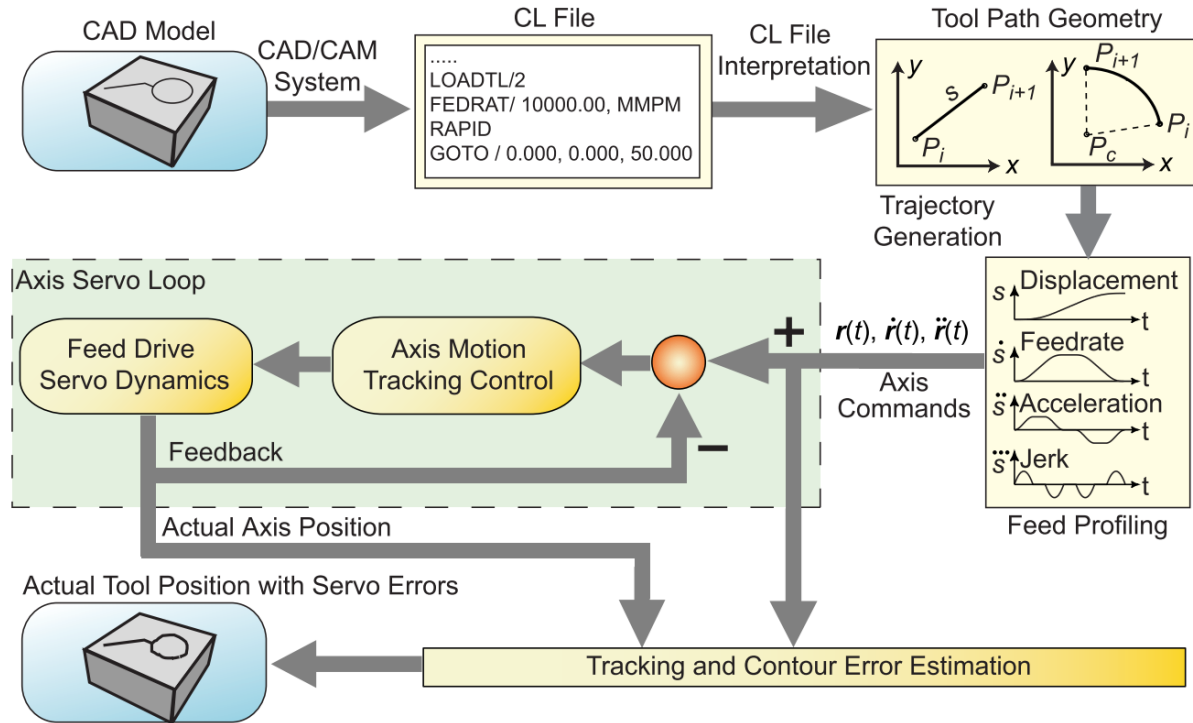
Fig. 2.1. Virtual Computer Numerical Control (VCNC) developed by Yeung et al. [10].

As shown in Fig. 2.1, the VCNC enables the reconfiguration of the feed drive dynamic model, a trajectory generation algorithm, and a tracking control algorithm. The reference tool path is constructed using a CAD/CAM software. This tool path is prepared in Cutter Location (CL) format, which contains prior information about NC block numbers, toolpath segments, feedrates, etc. According to the toolpath geometry, such as linear, circular, or spline types, the trajectory generation algorithm (i.e., interpolator) constructs discrete position commands as a function of jerk, acceleration and feed speed specifications. Generated axis commands are applied to the control law and the feed drive dynamic response is simulated. Here, each machine actuator has specific jerk, acceleration and velocity limits. It is important not to violate these limits. Violation may cause poor surface finish due to vibrations, and likely "deviations" in the achieved toolpath due to excessive tracking error [1].

6

In the following sections, two different feed drive modeling techniques will be discussed: bottom-up and top-down. Bottom-up approach refers to modeling and identifying the dynamic behaviour of each subcomponent, and afterwards determining the overall (i.e., collective) response of the system as a whole, by establishing the interconnections between the individual components. On the other hand, top-down approach refers to directly estimating a model for the overall system behavior, without having to identify models for the individual components.

2.2.2. Bottom-Up Approach in Modeling Feed Drive Dynamics

Correct construction of the feed drives' dynamic model allows accurate prediction of a real machine tool's response by the VCNC. This enables correction of trajectories ahead of time. Hence, modeling and identification of feed drive dynamics have a crucial role in building high-fidelity predictive models for CNCs. The following sections present different approaches for modeling feed drive systems: specifically considering the rigid body dynamics, friction, and structural vibration modes.

Rigid Body Dynamics

One of the simplest methods for modeling feed drives is considering the rigid body dynamics, which dominates the low frequency range. Rigid body dynamic models have typically been used to design model-based controllers, such as pole placement [13][14], generalized predictive [15], and sliding mode [16] control schemes. One of the commonly adopted rigid body models has been given in [17], and re-used in [18].
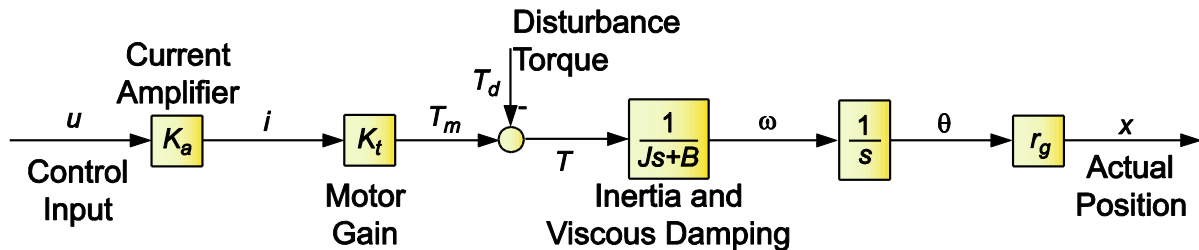
Fig. 2.2. Rigid body dynamic model.

A simplified rigid body dynamic model is shown in Fig. 2.2. In this model, the control input is injected into an amplifier (performing current regulation) which results in the armature current (i). It is assumed that the current regulation takes place at a much higher bandwidth than the mechanical response. This holds for most drive systems, where the mechanical frequencies are typically below 150 Hz, and the current regulation bandwidth is around 500 Hz. Thus, by neglecting the effect of the motor's back

e.m.f., and the current loop dynamics, the amplifier can be approximated (in many cases) as a pure gain (K_a). The armature current is then converted into actuation torque (T_m) through the motor torque constant (K_t). T_d represents disturbance torques in the system as felt by the motor, which may originate from the friction in the guideways, the cutting forces, as well as reaction forces due to vibration. The remainder (net) torque then actuates the drive system. The rigid body dynamics are modeled in terms of the equivalent inertia (J) and viscous friction (B) coefficients as felt by the motor. Theoretical prediction of viscous friction is very difficult and also sensitive to the operating conditions (such as lubricant temperature). While theoretical calculation of the inertia may be possible from machine drawings and data, accumulating uncertainty margins (from individual component inertias) may lead to errors in the estimation. Also, in many cases such machine drawings and data are not available or are difficult to obtain. Thus, it is more common to experimentally identify the values of J and B. One identification strategy, devised by Erkorkmaz and Altintas [18], uses a least square approach in which the rigid body model parameters and a simple Coulomb friction model are estimated using time domain data.

Another approach for estimating the rigid body parameters is frequency domain analysis, which provides insight into not only the low frequency behavior, but also gives an indication of the frequencies of vibration modes, uncertainty boundaries, and how the response varies with machine posture. The identification procedure is performed by matching the Frequency Response Function (FRF) gathered from the drive to the FRF obtained from an analytical model [13]. There is also a wealth of frequency domain curve fitting algorithms available for characterizing the rigid body behavior and structural modes of electro-mechanical systems [19][20].

Rigid body modelling is appropriate when there are no disturbance signals that excite the system resonances. Although this approach successfully captures the low frequency system response, it fails to predict the structural vibrations which occur when the commanded trajectory or more frequently the disturbance (process) forces contain high frequency content, such as high acceleration rates or cutting force harmonics. More advanced models, which also consider the effect of structural flexibilities are discussed in the next section.

Vibratory dynamics

In order to identify structural vibrations, the lumped-mass (2 Degree of Freedom (DOF)) model has been extensively used in the literature [13][21][22]; due to its simplicity and ability to correlate well with experimental effects. One of the simplest lumped (2 DOF) mass models used for ball screw drives

8

is shown in Fig. 2.3. In this Figure, m_1 and m_2 are the inertia of the rotating and translating components, respectively. b_1 and b_2 are the viscous friction coefficients. k represents the overall stiffness of the feed drive mechanism. Damping between motor shaft and the load is represented by c. u is the equivalent control signal. d_1 and d_2 are the disturbances on the motor and the load side, respectively [21]. Experimental identification of lumped mass model parameters is essential in order to have reliable models for control or prediction purposes. Okwudire [23] and afterwards Gordon and Erkorkmaz [24] used least squares identification to determine the lumped-mass, stiffness, and damping parameters from the measured FRF data for both ball screw and linear motor drives.
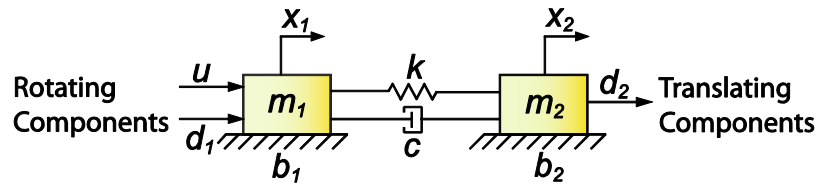
Fig. 2.3. Lumped (2-DOF) mass model.

Another model, the distributed mass model, was analytically developed by Varanasi and Nayfeh [25] with the intention of capturing the first mode of vibration in ball-screw drives. They derived second order wave equations for the system in the frequency domain for longitudinal and torsional dynamics, by considering the corresponding boundary conditions. These equations considered the compliance of the bearings and the nut. Although their method achieved reasonable closeness in predicting the first vibration mode, the main disadvantage is that the mathematical derivations are complex and tedious [13]. In addition, the remainder modes are not adequately captured. Hence, this approach is not convenient when higher order dynamics need to be analyzed and simulated.

Acknowledging that most feed drive systems contain more than one dominant vibration mode, Frey et al. [26] and Halroyd [27] used a higher-order lumped-mass (i.e., discrete/3 DOF) model, as shown in Fig. 2.4, which is an extension of the two-mass model in Fig. 2.3. While the two-mass model identifies only the first vibration mode, the multiple mass lumped model captures the first two dominant structural modes. Also, in this model, the vibratory dynamics, which are predominantly in the axial and torsional directions, have been clearly identified and can be constructed with reasonable closeness based on estimated inertia and catalog stiffness parameters. In this case, m_t and m_s are the table and ball-screw masses, respectively. J_s is the rotary inertia of the shaft. J_m is the inertia of the motor. k_{rot} and k_{ax} represent the rotational and axial stiffness values, respectively, and r_g is the transformation factor from

rotational to linear motion. The rotational and axial damping factors are c_{rot} and c_{ax}, which need to be experimentally 'tuned' based on experience and/or measurement. Also, while some qualitative predictions can be achieved with this model based on nominal inertia and catalog stiffness values, it is well-known that during the operational lifetime of a machine tool the feed drive stiffness can vary significantly, hence the parameters would in overall require updating.
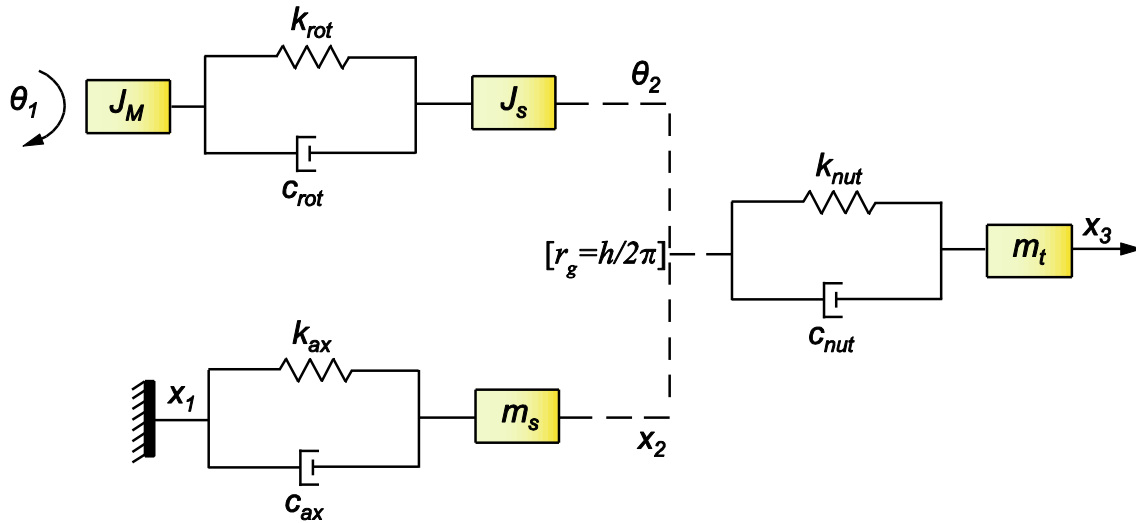
Fig. 2.4. Lumped (3-DOF) mass model [25].

The motion delivery mechanisms in ball-screw feed drives is more complex than the one analyzed by Varanasi et al. [25] or Frey et al. [26]. As the carriage changes position, the contact points along the screw with the preloaded nut also vary, and so does the transmission of reaction forces from one body to another. Also, the stiffness distribution changes. All of these effects impact the drive's vibration modes. To be able to capture such detailed and complex effects, Finite Element Modeling (FEM) can be used [13][28][29]. Van Brussel et al. used FEM to construct stiffness and modal mass matrices for a three-axis milling machine [30]. To reduce the complexity of the equations, the authors integrated reduced order models together. The disadvantage of applying pure FE is that such models may possess thousands of degrees of freedom (DOF)s, which makes the analysis too computationally intensive. After construction of individual component models, it has been preferable to represent each component with only its dominant modal characteristics (by order reduction), and to combine these components with each other along with discrete mass, stiffness, and damping elements (when applicable, to approximate simplified boundary conditions); using receptance coupling (also known as sub-structuring) techniques. These efforts have led to the development of hybrid FE models, which can also be updated on the fly for dynamic response analysis as a function of machine posture [31][32][33]. In

10

this approach, as demonstrated in Fig. 2.5, the rotor, table, nut, and frame can be modeled as rigid body elements. On the other hand, couplings, fasteners, bearings, and guideways can be represented as linear springs [20].
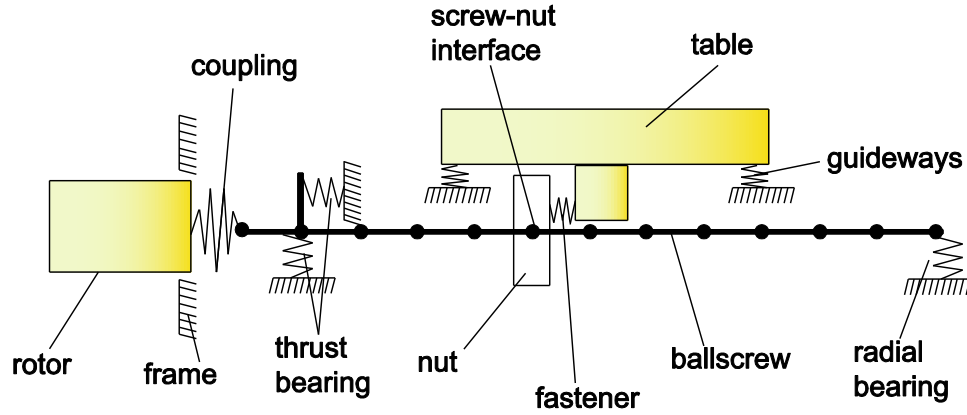
Fig. 2.5. Hybrid finite element model [23].

Pislaru et al. [34] used this approach and modeled the ball-screw as a distributed-mass system. However, this model did not consider the variation of dynamics with the nut and table assembly being at different locations of ball screw. Similarly, Kamalzadeh [29] performed FE analysis and represented the nut and table as an equivalent rotational mass, which was connected to the ball-screw by a torsional spring. Zaeh et al. [33] took FE analyses one step forward and derived the stiffness elements for the preloaded nut interface. Their model contained the cross-coupling effects in the axial and torsional direction while deriving the stiffness matrix. Later, Okwudire [20][23] expanded Zaeh's work to also consider the effect of lateral stiffness. By doing so, this model was able to capture additional cross-coupling terms between the deformations in the axial, lateral, and torsional directions.

In this thesis, the developed identification methods target mainly the rigid body dynamics of feed drives. Nevertheless, understanding the vibratory behaviour is integral to extending the methodology to higher order models in the future, thus focusing also on the vibratory dynamics.

Friction

In machine tools, friction is among the main sources of disturbance that causes positioning errors during motion. Especially, during velocity reversals, at sharp corners or circular arc quadrants in the toolpaths, the direction of friction force changes almost discontinuously. As a result, the control law (which may contain integral action or some kind of disturbance estimation and cancellation scheme) momentarily

applies compensation in the wrong direction, which further compounds the tracking error caused by the sudden change in friction disturbance, and results in oscillatory settling behavior afterwards. Hence, in order to be able to predict and reduce such errors, accurate modeling and identification of the friction is necessary.
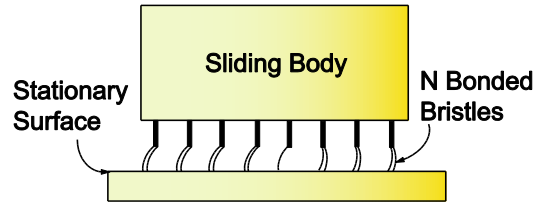
Fig. 2.6. Bristle model [41].

Currently, researchers are using physically motivated models in order to identify and compensate friction effects [35]. Armstrong's survey [36] gives detailed descriptions for different friction models. In this survey, friction is divided into two main categories: static (classical) and dynamic friction models. In classical friction models, the friction force is a function of the applied force and velocity. There is no memory (i.e., internal dynamics type of) effect, as opposed to dynamic friction models. A focus of this thesis is prediction of the effect of friction on the dynamic accuracy of machine tools. Dynamic friction models (which allow higher simulation fidelity over static ones) are reviewed in the proceeding paragraphs.

Friction can be described considering two main regimes; pre-sliding (or sticking) and sliding regimes. During pre-sliding, the surface contact points (at which micro-welds are hypothesized) act like springs which are being broken one by one and there is displacement dependence until the sliding regime begins. As sliding regime becomes dominant, solid-to-solid contact between the adjoining surfaces starts to disappear. Dynamic friction models are formulated to characterize both pre-sliding and sliding regimes.

An early attempt for describing the pre-sliding regime was proposed by Dahl in 1968 [37]. During his experiments, Dahl realized a connection between the stress-strain curve and friction force-displacement [37]. Then, he came up with the hysteresis representation of the friction force- versus displacement relationship for the pre-sliding regime. The Dahl model had a pivotal role in describing position dependent hysteresis loops. One of the main limitations of this model, however, was the lack of consideration for the Stribeck and breakaway force. Further modifications and discussions for this model have also been proposed in [38][39][40].

De Wit et al. [41] incorporated the Stribeck effect, which was the main missing element in Dahl's model, resulting in the 'LuGre' model (named after the collaboration between Lund and Grenoble Universities). In this model, friction bristles as illustrated in Fig. 2.6 are used to represent surface contact at the microscopic level. The friction force is defined as:

$$F_f = \sigma_0 z + \sigma_1 \frac{dz}{dt} + \sigma_2 v \tag{2.1}$$

where σ_0, σ_1 and σ_2 are the asperity stiffness, micro-viscous friction and viscous friction coefficients, respectively. z is the average deflection of the asperities and v is the velocity. The average deflection of the bristles is modeled by

$$\frac{dz}{dt} = v - \sigma_0 \frac{|v|}{s(v)} z \tag{2.2}$$

Here, $s(v)$ is the Stribeck function and it is generally defined as

$$s(v) = sgn(v)(F_c + (F_s - F_c)e^{-\left|\frac{v}{vs}\right|^\delta}) \tag{2.3}$$

Above, F_s and F_c are the static and Coulomb friction forces. v_s and δ represent the Stribeck and velocity shape factor, respectively.

One major drawback of the LuGre model is that it does not represent the hysteresis effect with nonlocal memory for the pre-sliding regime. Swevers et al. proposed a new model called "Leuven model" to capture the hysteresis effect with nonlocal memory [42]. Further research noted that the Leuven model needed to be extended to also take into consideration the stack size, which is the number of successive hysteresis loops during motion. In order to consider the stack size in advance to prevent stack overflow, Al-Bender et al. proposed the Generalized Maxwell Slip (GMS) model [43], which is currently one of the state-of-the-art dynamic friction models. This friction model has been cited and applied by many researchers, including in [43][44][45].

The capability of demonstrating three main characteristics of friction, namely the Stribeck effect, hysteresis with non-local memory, and frictional lag, has enabled the GMS model to be amongst the most effective friction models. The GMS model is a combination of individual single state models, as illustrated in Fig. 2.7. Each single state sub-model designates whether that particular element is in a sticking or a slipping condition. In this figure, there are N elementary spring block units. The forces of

13

these N elementary units (i.e. elements) are added together to obtain the equivalent friction force [46] [47].
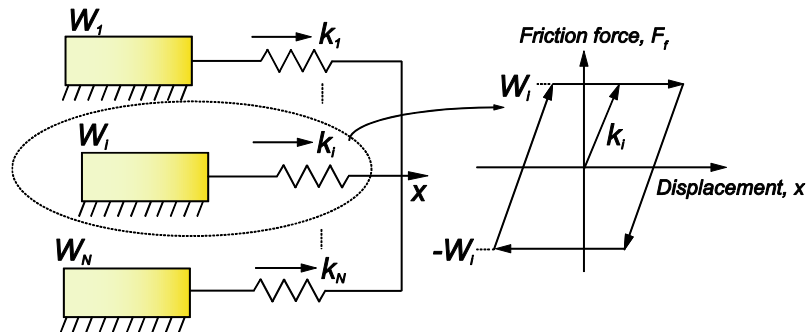
Fig. 2.7. GMS model representation [47].

Although the GMS model has become very popular recently, the main disadvantages of this model are: 1) discontinuous switching between pre-sliding and sliding regimes that make gradient-based state and parameter estimation challenging, and 2) the large number of parameters required to characterize all of the elements. These factors make the GMS model difficult to parameterize and simulate. In the literature, to overcome the first drawback, there have been attempts to simplify the GMS model without changing its main characteristics. In [48], to obtain continuous switching between sticking (pre-sliding) and sliding regimes, Boegli et al. presented the smoothed GMS (S-GMS) model. S-GMS approach makes the original GMS model more suitable for gradient based state and parameter estimation by using a sigmoid function. Piatkowski [49] has further analyzed the effectiveness of six different sigmoid (smooth) functions, resulting in the so-called modified GMS (M-GMS) model. In [48] and [49], in addition to the GMS model parameters, smooth functions introduce extra parameters to be identified, which further increases the estimation and computational complexity. Villegas et al. [50] have taken a different path, and instead of smoothing the switching dynamics with respect to the states, the authors have proposed to decrease the multi-state structure of the original model by means of algebraic manipulations, leading to the 'two-state GMS model'. There has also been other work to reduce the number of unknown parameters of the GMS friction model, such as [51]. In this study, rather than constructing the hysteresis characteristics based on the breakaway forces, the hysteresis curve is constructed based on breakaway displacements, which can be observed from experimental tracking data. Also, each element's friction force is constructed based on an activation matrix, which contains elemental velocities. This approach bypasses a burden to identify $2N$ parameters and only stiffness parameters need to be estimated, which reduces the number of unknowns to N. However, actual breakaway displacements should be carefully extracted from the pre-sliding portion and after that, the

activation matrix needs to be constructed. This approach simplifies the model, but requires high temporal and displacement resolution data collection, and a careful analysis to estimate breakaway displacements from the experimental data. Automation of this approach is possible, but requires a suitable heuristic algorithm.

The parameter identification of the GMS model based on both time and frequency domain data has been studied in [52]. In this study, small amplitude sinusoidal signals have been applied to the experimental setup with a low bandwidth controller to avoid drift until the setup comes to the verge of sliding. Until the breakaway (i.e. the point where there is a transition from pre-sliding to sliding), the hysteresis curve is fully constructed and the most recent hysteresis curve is selected to extract GMS parameters. In time-domain identification, a combination of linear segments have been fitted to the experimental hysteresis curve to capture the variation in effective stiffness as individual elements disengage.
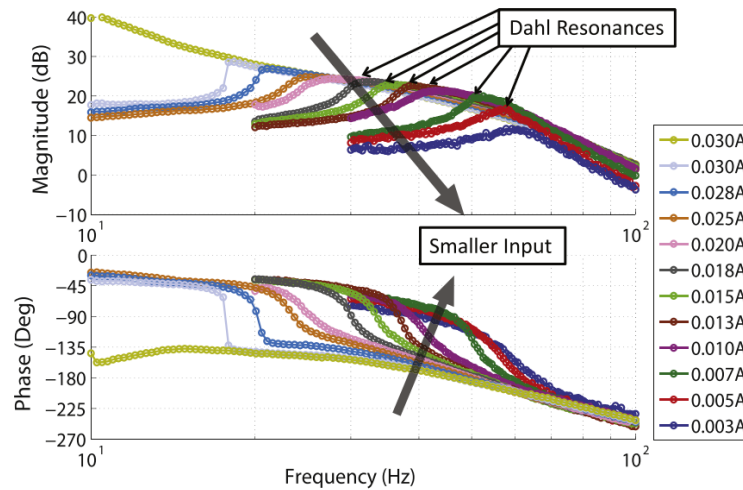
Fig. 2.8. Dahl Resonances [44].

Frequency-domain identification, in some cases, can offer a simpler estimation process compared to time-domain approaches. Yoon and Trumper [44] also developed a frequency domain identification method (i.e., the Dahl resonance identification technique) to obtain GMS model parameters. Dahl resonances based on FRF data are shown in Fig. 2.8. In this technique, the system (i.e., servo-motor with high resolution encoder and motor driver) is excited with sinusoidal input and then FRF data is gathered. For small input amplitudes, since the data exhibits pre-sliding friction characteristics, the equivalent pre-sliding stiffness at each excitation amplitude can be derived from the apparent resonance

frequency, from which the GMS model parameters can be obtained. The performance assessment of the proposed model was experimentally validated with and without a model-based friction compensator in both the frequency and the time domains. The result showed that the model parameters, which were identified using Dahl resonances, contributed to significant improvement in the dynamic accuracy for the friction-compensated system.

Apart from the GMS model identification and parametrization, identification of friction model parameters, in general, has a vital role in model-based control for compensation of friction in high precision positioning applications. Such identification for different friction models using experimentally gathered time domain data has been studied extensively in the literature [18][53][54]. These studies can be divided into two main groups; black-box and grey-box techniques (also referred to as physics based) [55][56][57]. Comparisons between the two strategies were made based on prior knowledge of the friction dynamics. If there is no prior information, black-box models were used and grey-box models in the other case.

There have also been studies for the identification of other friction models based on FRF data [58][59][60][61]. Kim et. al. [58] and Chen et. al. [59] took basic Coulomb and viscous friction into account in order to identify servo drive dynamics with friction. The LuGre dynamic model was also considered in [60] based on frequency domain analyses.

In this thesis, a new approach is proposed for parametrizing the pre-sliding portion of the GMS friction model with a reduced number of parameters. Rather than discretizing the pre-sliding virgin curve through a multitude of spring elements (typically requiring 8, 10, 12, …, parameters), a single shape factor is proposed, which together with the knowledge of the breakaway force and breakaway displacement, can adequately represent the experimentally observed pre-sliding behavior. This is explained in Chapter 4.

2.2.3. Top-Down Approach in Modeling and Identification of Feed Drive Dynamics

In today's industry, there is a significant need to digitize manufacturing systems and processes as technology evolves rapidly. As computers become more powerful than before, the manufacturing sector is moving towards its forth revolution, also called 'Industry 4.0'. In this era, computers are interconnected. Based on data transmitted, they make decisions to increase productivity and reliability in the manufacture of high quality products. There are four main components of Industry 4.0 [62]: a) Cyber-physical systems (CPS): This refers to the integration of computers and networks with the

physical process of manufacturing operations, where there is autonomous information exchange and triggering actions. b) Internet of Things (IoT): Enhancing objects' and machines' capabilities (for example, mobile phones and sensors) to communicate with people and each other. c) The Internet of Services (IoS): This feature enables systems and machines that are in service to be remotely reprogrammed with new functionalities during their life cycle. d) Smart factory: This is related to creating a system that can deal with the physical world and as well as the CPS over the IoT, which allows the execution of tasks even more effectively, efficiently, and with intelligence.

Some of the design principles that relate to the main theme of this thesis can be summarized as follows: a) Virtualization: CPSs should be able to simulate and construct the virtual entity of an actual system. b) Real-time capability: A smart factory should collect real-time data and be able to make decisions and present new outcomes by post-processing the collected data sets. c) Modularity: The system should transition itself to new changing conditions and environment. There are also other design principle that can be seen in [62]. However, especially virtualization and real-time capability fall in-line with the idea of estimating feed drive dynamics in a virtual environment using the top-down approach.

In the following, a brief literature of the top-down approach is given. The objective is to estimate one or several of the closed-loop transfer functions belonging to the feed drive control systems. Since this thesis proposes a new technique based on the top-down identification approach, and makes a direct comparison with an earlier proposed "rapid identification" strategy, more detailed explanation of the earlier method will be presented in Chapter 3, in context with the new methodology development.

As mentioned in previous sections, for finding the dynamics of feed drives, there are various techniques already proposed. One open-loop identification strategy for finding rigid body dynamic parameters uses the least squares (LS) approach in which the rigid body model parameters and a simple Coulomb friction model are estimated jointly from time-domain data [17][18]. There are also frequency domain curve fitting algorithms available for characterizing the rigid body behaviour and structural modes of electro-mechanical systems [19]. However, accurate structural mode identification requires broadband excitation, which is difficult to achieve via smooth CNC trajectories.

System identification techniques can be classified into three main groups: the prediction error, subspace [63], and the nonparametric correlation and spectral analysis techniques [64]. Some open-loop techniques, such as the subspace method, do not work well when closed-loop data is used due to the fundamental complication of correlating measurement noise and the applied input [65]. Closed-loop

17

identification techniques, in the prediction error framework, have attracted the attention of researchers due to common interests in industrial applications.
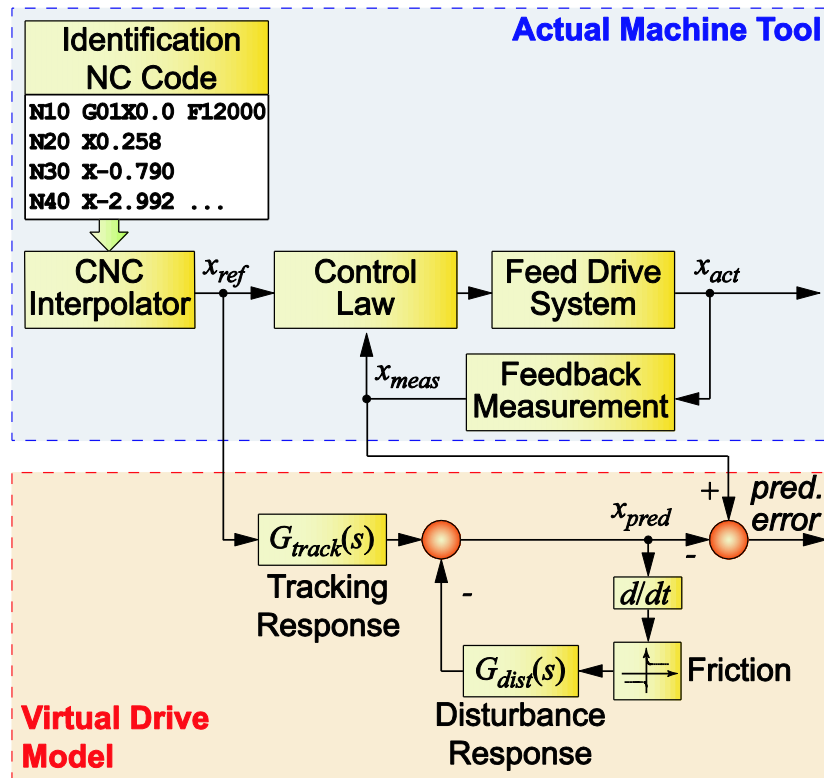
Fig. 2.9. General scheme for top-down technique [73].

In general, closed-loop identification methods are divided into three main categories: direct, indirect, and joint input-output based techniques [66]. In the direct identification method, the feedback loop is ignored and the open-loop system parameters are identified using input and output measurements. In [67], a direct identification technique is proposed where a step is applied to the system as a command input, a frequency response measurement of the output is obtained, and the continuous-time transfer function is identified. In the indirect method, a few of the closed-loop transfer function parameters are identified, then the open-loop parameters are determined using a priori knowledge of the system's linear controller. When noisy measurements are present, Silva et al. proposed the use of the Laguerre series expansions to analyze the closed-loop model through identification by applying a step response [68]. In the joint input-output approach, the plant input and the process output are considered as the outputs of the system and the reference and the noisy signals are treated as inputs of the system. Based on this joint correlation, the process model is estimated [64][65].

According to Forsell et al. [69], the first step of the system identification problem is the experiment design to maximize the information in the data to obtain the system's best possible dynamic model. All of the aforementioned work typically require a command input that delivers sufficient excitation to be applied to the closed-loop system, such as a step input, or a pseudo random binary sequence (PRBS). However, in CNC machine tools, motion commands are typically smooth up to acceleration level, which renders the identification of multiple transfer function parameters even more challenging [70] due to lack of excitation. There are also other studies to reduce dependency on the system's excitation during regular operation [71][72]. The authors achieve this goal by imposing different performance criteria prior to experimental validation. While generally successful, the method proposed in these papers requires extensive amount of data for training the model. In a practical manufacturing environment, it is preferable to identify reliable virtual models with the minimal amount of data.
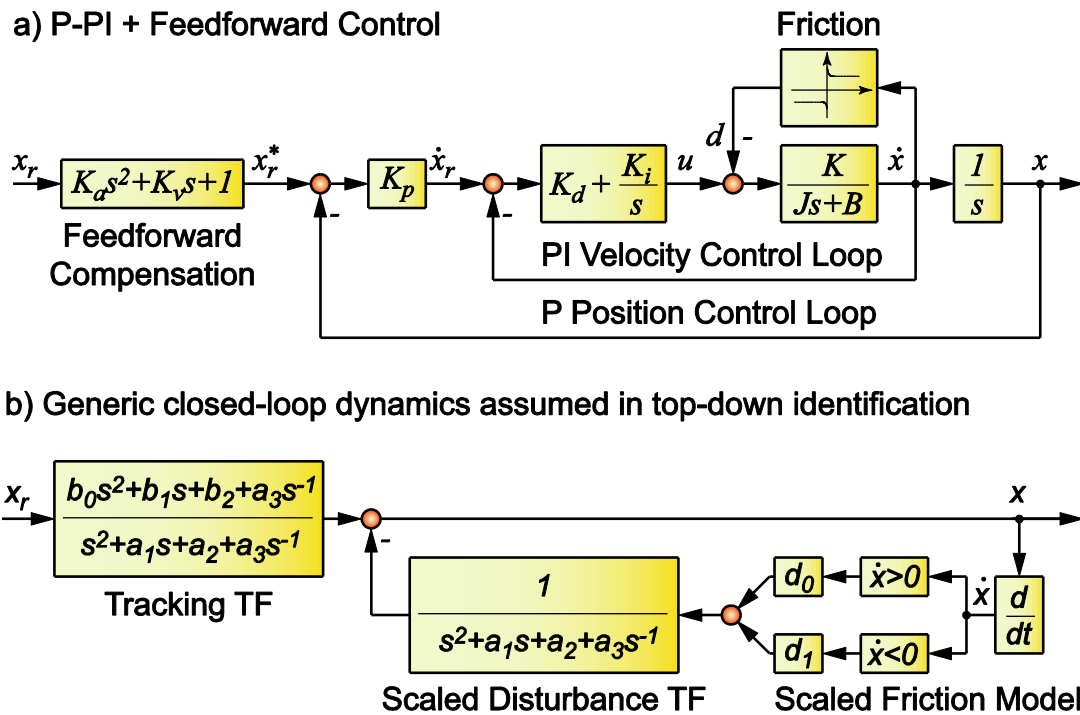
Fig. 2.10. P-PI position-velocity cascade control structure and generic closed-loop model in rapid identification [73].

Overall, the aforementioned feed drive dynamic modeling techniques explained previously, as well as the methods already proposed in literature, have crucial roles in predicting the final accuracy of feed drive systems. However, experimental identification of such models is generally time consuming and requires significant expertise on dynamics, identification theories, and the technical expertise to apply

this knowledge on production equipment. In addition, bottom-up modeling based identification tests typically need to be performed on the shop floor; which causes downtime to the machine away from production. Instead of going through these steps, a top-down approach has been proposed in literature [73][74]. In this top-down method, as shown in Fig. 2.9, a short duration NC code is executed (comprising typically random motion commands) and the commanded and actual position data is gathered for reverse-engineering a model that emulates the machine tool drive's closed-loop command tracking and disturbance response behavior in a limited frequency range.

This approach is also capable of capturing the effect of Coulomb friction, which enables the prediction of tracking errors and quadrant glitches that stem from abrupt motion reversals. One of the common feedback control structures (i.e., P-PI cascade control) is given in Fig. 2.10a. Here, the position loop is closed using proportional control and the velocity loop with proportional-integral (PI) control. Feedforward compensation is also used to widen the servo tracking bandwidth so that the positioning accuracy can be improved for rapidly varying motion commands. The generic closed-loop model in Fig. 2.10b can capture this closed-loop dynamics, as well as other control configurations in which third order dynamics are prevalent, such as direct PID position control, or pole placement control with a Kalman filter based state feedback and trajectory pre-filtering [73].
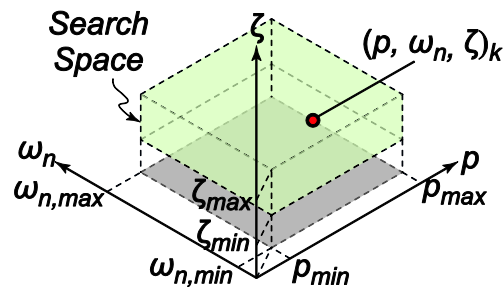
Fig. 2.11. Solution search space for constrained identification of top-down models [73][74].

The merit of the top-down approach in [73], developed for feed drive systems with predominantly rigid body response, is to represent a wide class of feed drive systems with only 8 parameters (3 poles, 3 zeros, and 2 friction parameters). After data collection, the closed loop tracking and disturbance transfer function parameters are first identified using a LS based formulation. The interpolator generated motion commands are generally smooth and may lack the persistence of excitation, which does not allow the eight parameters to be estimated with sufficient closeness to their actual values. This is a minor problem that can be ignored as long as the identified feed drive model is capable of representing the real dynamics in a satisfactory manner within the frequency range of the CNC motion commands. However,

20

this issue may result in problems when the estimated model has unstable or poorly damped pole locations. In order to prevent this situation, bounds are imposed in [73] and [74] on the closed loop pole locations, as shown in Fig. 2.11. Then, the numerator and friction parameters for each selection of pole locations can be obtained by solving a LS sub-problem (i.e., via LS projection):

$$\underbrace{\Phi_2 \theta_2}_{\substack{Numerator\ (zeros)\\ and\ friction\ terms\\ \sim(b_0,b_1,b_2,d_0,d_1)}} = \underbrace{Y}_{\substack{Measured\\ response}} - \underbrace{\Phi_1 \theta_1}_{\substack{Terms\ related\\ to\ tested\ pole\\ locations\\ \sim(a_1,a_2,a_3)}} + \underbrace{E}_{\substack{Model\\ prediction\\ error}} \qquad (2.4)$$

In this thesis, a novel formulation has been developed for this top-down identification problem, which significantly improves the numerical conditioning and convergence properties of the model, and the robustness of the estimation against measurement noise. This is presented in Chapter 3.

2.3.   Literature on Iterative Learning Control

In a wide range of industrial applications, such as robotic manipulators, machine tools, and chemical reactors, the nature of the reference and disturbance inputs are repetitive. Especially, in machine tools, which execute the same tool motion repeatedly in batch or mass production scenarios, when the operating conditions are well controlled (i.e., vibration isolated, temperature controlled, etc.), then the servo positioning accuracy is affected by the commanded trajectory and disturbances (such as friction and cutting forces) in a fairly repeatable pattern. These effects lead to cyclical error profiles, which are implicitly influenced by unmodeled dynamics, parametric uncertainties, and unmodeled or uncompensated disturbances.

In order to reduce errors in the presence of such factors, different control techniques, ranging from classical control to the more complex methods, such as robust and adaptive control, and nonlinear control, have been proposed. Neural network, fuzzy logic based, and intelligent control have also been studied and implemented in various applications [75][76]. However, these control strategies may not always be suitable for production machines, such as machine tools and robots, because of the complexity of the methods and the requirement to modify the feedback/feedforward control structure, which is typically fixed in industrial servo controllers. On the other hand, Iterative Learning Control (ILC), which can be categorized as an intelligent control technique, can be implemented by simply modifying the trajectory command sequence in order to mitigate the repeating error patterns. This would require no change of the feedback or feedforward portions of the servo control system. Thus, it has generated strong appeal for industrial application.

The first concrete model and analysis of ILC emerged during the 1980s, which was motivated for robotic manipulators performing repetitive tasks [77][78]. Afterwards, considerable literature has grown around the topic of ILC [79]. Several surveys covered the theoretical background and referenced other published papers relating to ILC [79][80][81][82]. Per various definitions and goals which have been reported in literature, the main objective of ILC is to achieve an inverse effect for the plant (or closed-loop system) which counteracts the influence of repeating inputs [79]. In many situations, ILC can be implemented with minimal information about the system model.

Various ILC techniques have been proposed in the literature. Markusson et al. [83] used ILC for nonlinear non-minimum phase systems. In the same study, the inverse of a linearized model with non-causal filtering has been used. A more comprehensive discrete-time inverse model based ILC has been proposed in [84]. In addition, to enhance the contouring performance of multi-axis CNC machine tools, other ILC techniques such as cross-coupled ILC has been proposed [85]. For multi degree of freedom (DOF) structures, for example for industrial servo systems where positioning errors arise from both motor and load side, dual-stage ILC has been proposed in the literature [86]. Further analysis on 2-DOF structures has been considered in [87] and [88].

The general architecture of ILC technique is shown in the Fig. 2.12. In this architecture, which is also referred to as the serial configuration, ILC is applied before the feedback controller. This type of configuration is convenient when there is a commercial controller that does not give direct permission to alter the control signal applied to the plant (as is in most machine tool drives). Conversely, in the parallel configuration, the ILC signal is combined with the feedback controller input. This approach directly modifies the control signal applied to the plant. If feedforward action is available on the control structure, then this approach can be adopted. The parallel configuration also enables the separation of the performance contribution of ILC from the feedback control action [81]. Owing to the semi-rigid control structure which has been established in the machine tool industry, in this thesis the serial configuration of ILC has been investigated.

In Fig. 2.12, x_r is the reference and x_j is the output signal. j is the iteration number (denoting the instance of running the repeating command trajectory). For every iteration, the sequence of recorded tracking error e_j and ILC input u_j are stored in a memory. The purpose of ILC is to decrease the tracking error $e_j = x_r - x_j$ by generating the feedforward signal f_j. f_{j+1} is generated based on the history of e_j and u_j from the previous iteration. The ILC update law given by [89],

$$f_{j+1}[k] = Q(z)[f_j[k] + L(z)e_j[k]]$$

(2.5)

where for a continuous time signal e, the corresponding sampled time signal is denoted by $e[k] \triangleq e(kT_s)$, where T_s is the sampling time. The tracking error is recorded in memory for every iteration 'j' and discrete time instant 'k'. Above, $L(z)$ and $Q(z)$ are z-transform of the learning property and robustness filter of ILC, respectively. Under the assumptions that: i) The initial state of the system is set to the same value at the beginning of each iteration, ii) The closed loop system is stable, and also that iii) The closed loop system is linear and time invariant (LTI). The stability of applying ILC and the monotonic convergence of the error to zero are met by the following condition,

$$\|Q(z)[1 - L(z)C(z)]\|_i < 1, \qquad i = \{1, 2 \ldots \infty\}$$

(2.6)

$C(z)$ is the z transform of the closed loop transfer function. $\|.\|_i$ is the 'norm' operator.
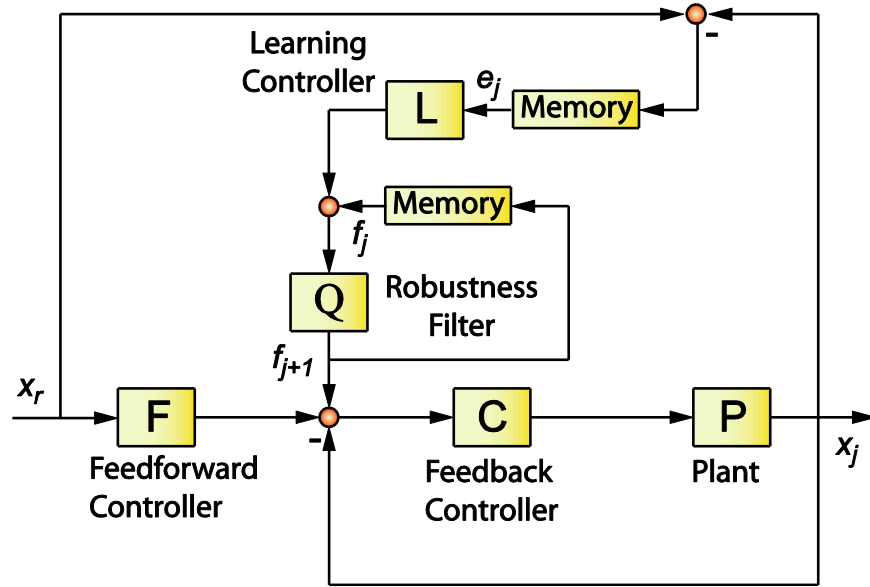
Fig. 2.12. Iterative Learning Control Dynamics [89].

In this thesis, ILC has been investigated to improve the repetitive errors that occur during multi-axis contouring motions. While ILC can be directly implemented with experimental (field) data during an ongoing manufacturing process, during the learning and adjustment period, servo positioning accuracy and therefore the manufactured part quality would be sacrificed. Also, valuable (productive) machine time would be wasted. Rather, the objective is to perform ILC directly using an estimated virtual model of the servo system, in order to minimize the amount of trial and error required on the actual machine-tool. The investigation carried out on ILC is discussed in Chapter 6.

Chapter 3

Estimation of Feed Drive Closed-Loop Models Considering Rigid Body Dynamics

3.1. Introduction

Understanding the accuracy and motion limitations of the servo system in a machine tool is critical to planning process trajectories that can make maximum use of that machine's dynamic capabilities. While there are already established methods for developing dynamic models of servo drives, such as using first principles modeling, identifying each parameter/gain one at a time, or analyzing the response of one feedback loop at a time, such methods can be time consuming and detrimental to the daily operation of a production machine. The proposed methodology in this chapter aims to estimate equivalent closed-loop models of feed drives in a nonintrusive manner, directly from field data which is collected ideally without interrupting the machine's operation. Thus, it holds promise for conveniently migrating into virtual production planning through the use of so-called 'digital twins', with minimal negative impact on the manufacturing performance.

In this chapter, feed drive closed-loop dynamics estimation considering rigid body modeling is described and the effectiveness of the proposed estimation is demonstrated around two case studies. The first is gear form grinding. The second is related to identifying the x-y axes of a 5-axis machine tool which was conducted in collaboration with another graduate student, Ms. Ginette Tseng, MASc at University of Waterloo. The two application setups used for validation purposes are first explained in Section 3.2. Classical (bottom-up) approach, which identifies the dynamics of the servo drives through one-by-one modeling and time- and frequency-domain techniques are presented in Section 3.3. In Section 3.4, an earlier method for identifying virtual dynamics in a top-down manner, which can be usually implemented with classical LS, is described. Afterwards, the new algorithm proposed in this thesis, based on pole search in conjunction with LS projection, is presented in Section 3.5. To compare the effectiveness of the new method over the earlier approach, identification results under simulated measurement noise and a convergence analysis are presented in Section 3.6. Experimental estimation results based on the aforementioned two applications are given in Section 3.7, demonstrating the improvements obtained with the proposed algorithm. The chapter ends with conclusions in Section 3.8.

3.2. Two Sample Applications: Gear Form Grinding and 5-axis Milling Machine Tools

3.2.1. Gear Form Grinding Application

The proposed identification methodology was validated on a gear grinding machine tool, as seen in Fig. 3.1. This machine is located at Ontario Drive & Gear Ltd. (ODG, New Hamburg, Ontario, Canada) and used for the production of high precision gears. ODG manufactures different kinds of gears, including marine gears, mining gears, automotive gears, etc. The company also manufactures conveyor systems and power transmission couplings for various vehicles. Gear quality is essential for smooth power transmission and machine life. In order to manufacture high quality gears and gear assemblies, ODG uses different CNC machines such as turning, milling, grinding, hobbing, and gear shaping. Among these processes, grinding constitutes 35-40% of the annual production.

There are various types of grinding configurations (form grinding and generating (i.e., worm) grinding). In form grinding, which is particularly suited for small batch sizes and customized gears, the abrasive wheel assumes the negative shape that is to be imparted onto the gear tooth-gap profile, which is ground as one gap at a time. Fig. 3.1a shows a schematic diagram of a Kapp KX 300P CNC gear grinder used at ODG [90]. While the illustration may appear a bit complicated, the crucial portion (the dressing tool and the grinding wheel) that has been used in testing the modeling in this thesis has been highlighted (for clarification) in color. Trimming the grinding wheel to the correct shape is achieved through a process called 'dressing', during which the x-y axis carriage (highlighted in yellow in Fig. 3.1a) supporting the grinding wheel performs relative motion with respect to the dressing tool located at a fixed station. Fig. 3.1b shows a photograph of the dressing tool, workpiece, and grinding wheel together. Also, Fig. 3.1c shows a typical dressing operation for form grinding and Fig. 3.1d illustrates motion of the x-y carriage. Fig. 3.1e demonstrates how a shaped grinding wheel is used to produce gears with the correct tooth and gap contours.

In form grinding, the dressing takes up about 15-30% of a part's cycle time. Increasing the dressing speed results in shape distortion, thus tooth form errors, due to increased tracking and contouring errors which occur at high velocity and acceleration magnitudes. Hence, having an accurate model of the feed drive system obtained through pole search method can enable such errors to be predicted and corrected ahead of time, allowing productivity gains to be achieved by increasing the dressing speed.
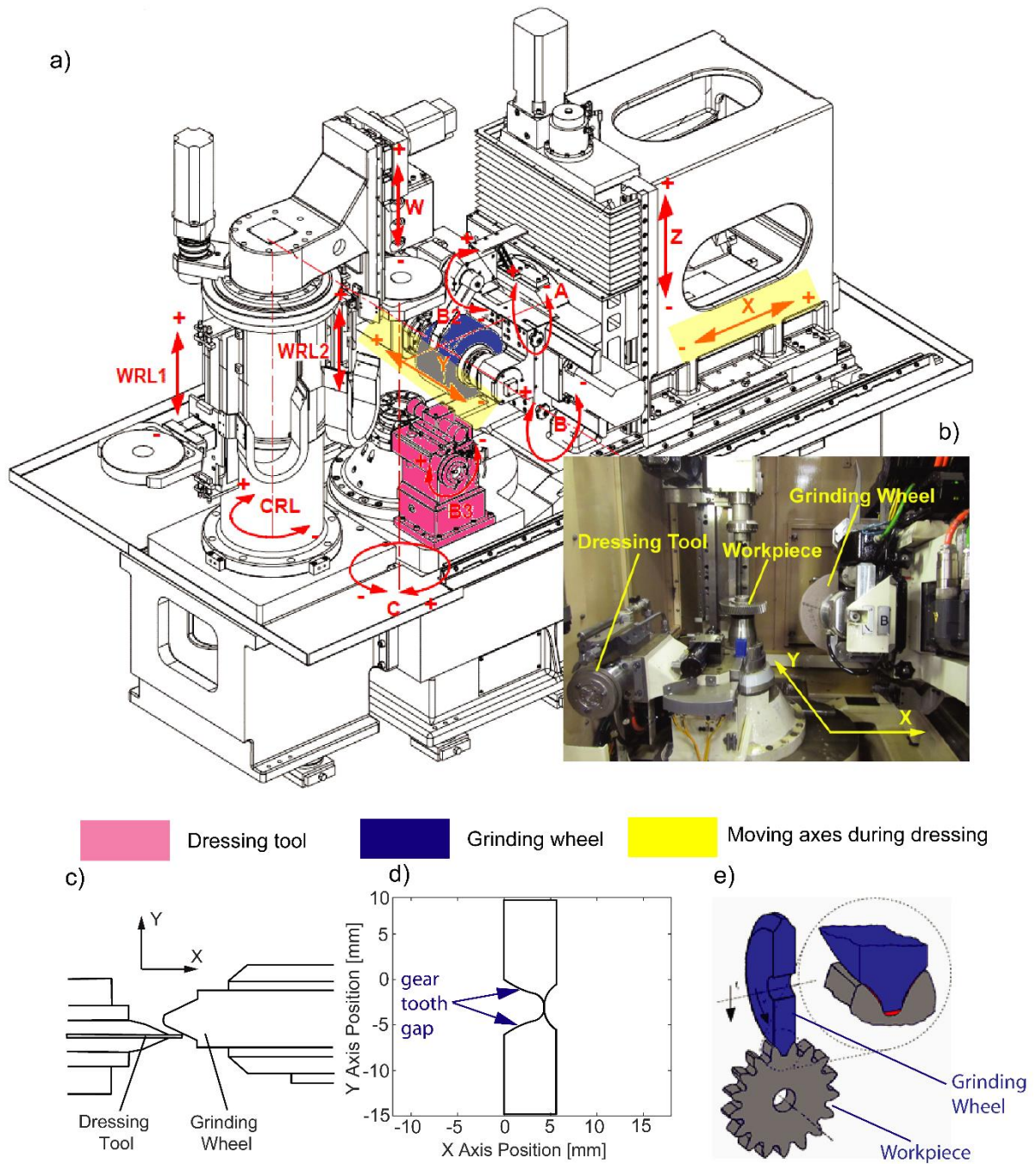
Fig. 3.1. a) Form grinding setup [90] b) Dressing tool, workpiece and grinding wheel. c) Dressing tool-grinding wheel operation [92]. d) Dressing path. e) Workpiece-grinding wheel contact.

3.2.2. 5-axis Milling Machine Tool Application

The Deckel Maho 80P hi-dyn five-axis machining center in Fig. 3.2 was also used as a test bed to validate the proposed identification method. The machining center has a Heidenhain TNC 430N controller with a built in scope function which allows 4096 data samples to be logged at a sampling period of 0.6 ms. The scope function was used to capture position commands, as well as measured position data from the linear encoder with 0.1 μm resolution. The simulation and experimental results presented in this chapter related to this setup were obtained together with Ms. Ginette Tseng.
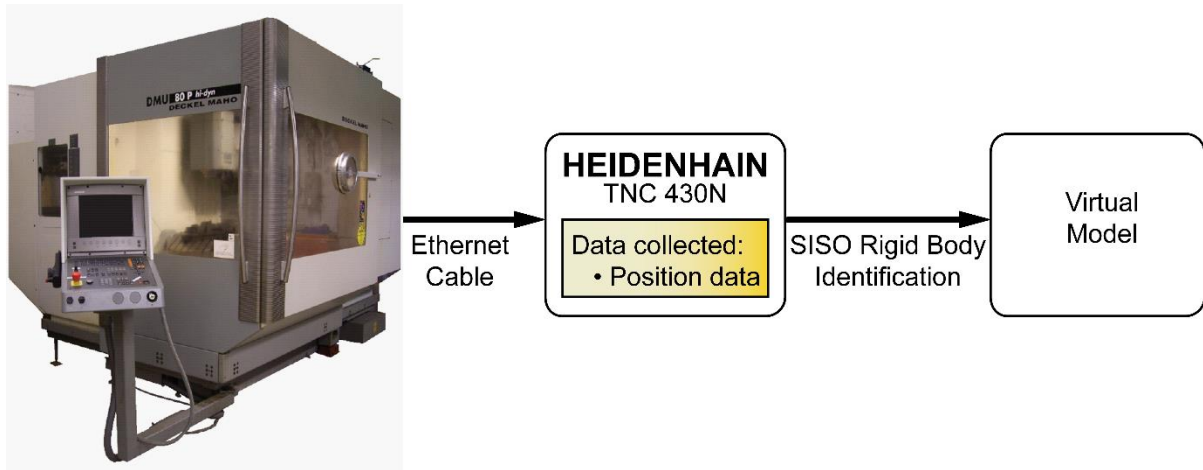
Fig. 3.2. 5-axis machine tool for validating pole search method.

3.3. Classical (Bottom-Up) Approach

The most common servo control structure, and the one encountered in the two experimental setups, is 'P-PI position-velocity cascade control'. The P-PI controller is easy to tune and implement, and therefore widely used in industry. The control of the feed axes of the grinder is achieved with P-PI control, implemented together with additional filter and logic. Compact representation of this control structure is also captured with Fig. 3.3. Further details on some of the individual blocks, not illustrated in this figure, can be found in [91], which was obtained from the Siemens 840D CNC documentation.

Frequency response function (FRF) measurements were taken from the gear grinding machine dressing process and used to identify the inertia parameter, J. Viscous friction (B) identification was challenging, as the frequency of the corresponding pole (B/J) was below the measured frequency range on the Siemens CNC. Hence, B was taken as zero. The filter, feedback controller, and feedforward compensation parameters were also identified from their respective CNC parameter entries.
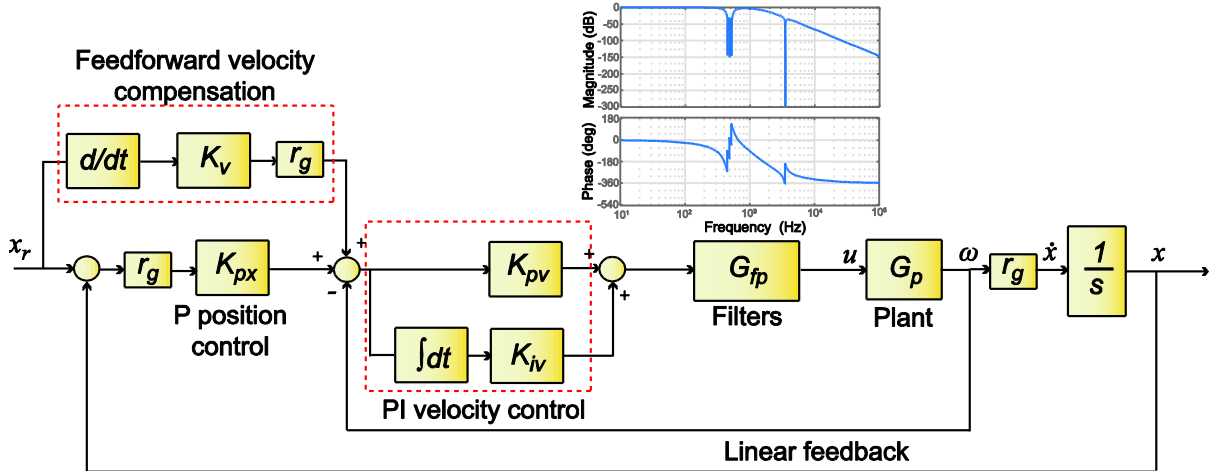
Fig. 3.3. P-PI position-velocity cascade control scheme with velocity feedforward term.

The P-PI cascade control system model was validated by capturing the command and actual (translational encoder) x-y position data from the grinder during the dressing operation, and comparing the actual motions of the machine with those predicted with the model. These results are shown in Fig. 3.4. At the initial glance, it can be seen that the model predictions are in reasonable agreement with the actual movements of the machine tool. While the instantaneous servo errors are replicated well to a certain extent, there is still some discrepancy in the predictions. One disadvantage of the classical (bottom-up) approach is that it takes a long time to build, which results in loss of productivity due to the machine tool not being used to make parts. The construction of this model would, in normal circumstances, have caused several hours of downtime to the machine tool, even if the control engineer performing the identification is well familiar with the operation of the CNC and its internal structure. When such familiarity is missing (for example in identifying servo models for machine tools of different builds, perhaps controlled with different CNC's), this process can take much longer.

As a main objective in this thesis is to build virtual models of servo drive systems from in-process data, this bottom-up effort constitutes a baseline in terms of evaluating the effectiveness and efficiency of other approaches, such as the one proposed in Section 3.5.
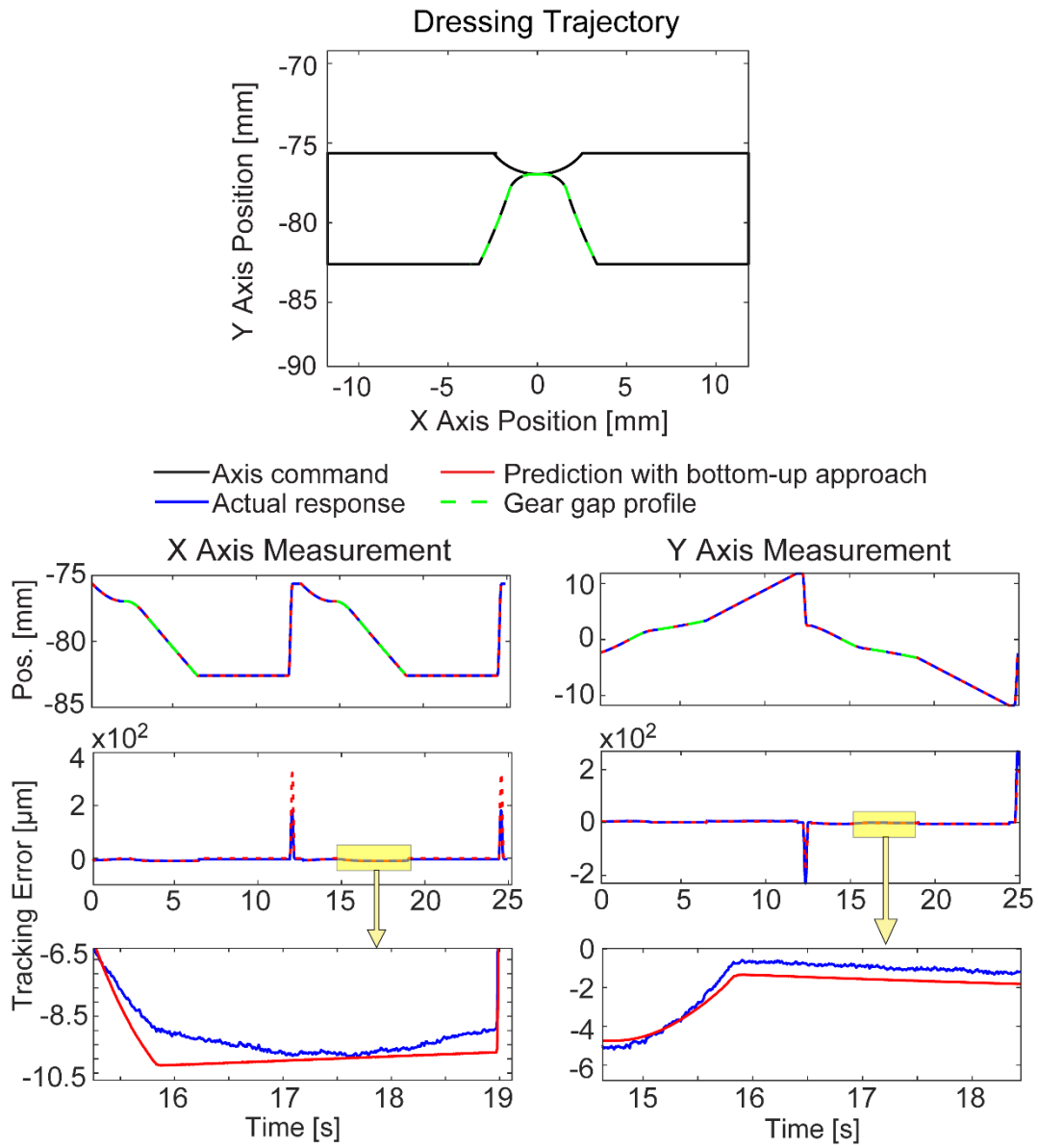
Fig. 3.4. Validation of bottom-up model with in-process captured dressing trajectory.

3.4. Earlier Method of Rapid Identification – Utilizing Least Squares for Estimating the Equivalent Closed-Loop Tracking and Disturbance Response

As explained in [73], a third order model is capable of describing the closed-loop behavior of a large class of feed drive control systems, such as a ball screw or direct drive system. This model can be controlled by various feedback techniques (P, PI, PD, PID, and/or P-PI cascade control), which can contain feedforward dynamics or friction compensation, as long as the closed loop transfer function is dominated by 3rd order dynamics. Also, the double pole term has been allowed to assume damping values larger than 1. This provides the accommodation to represent third order systems with three real poles. There are three main assumptions that this approach makes. Firstly, the structural resonances of the machine are avoided, hence the machine is modelled as a rigid body. Secondly, the motor and amplifier are run below the saturation limit, ensuring that they operate in their linear range. Finally, the nonlinearities in the system have very little influence on the motion of the feed drive. For example, the backlash in precision ball screws is typically an order of magnitude smaller than the encountered servo errors. Under these assumptions, the equivalent closed-loop dynamics can thus be modelled as:

$$
x(s) = \underbrace{\frac{b_0 s^2 + b_1 s + b_2 + a_3 \frac{1}{s}}{s^2 + a_1 s + a_2 + a_3 \frac{1}{s}}}_{G_{track}(s)} x_r(s) - \underbrace{\frac{K/J}{s^2 + a_1 s + a_2 + a_3 \frac{1}{s}}}_{G_{dist}(s)} d(s)
\tag{3.1}
$$

Here, $x_r(s)$, and $x(s)$ are the commanded and actual axis positions, and $d(s)$ represents the disturbance (such as friction) acting on the motion system, all represented in the Laplace domain. Their time-domain representations are $x_r(t)$, $x(t)$, and $d(t)$. a_i and b_i are polynomial coefficients of the transfer functions. $G_{track}(s)$ is the equivalent command tracking transfer function and $G_{dist}(s)$ is the equivalent disturbance response. J represents open-loop inertia of the feed drive, and K the product of the motor torque gain, current amplifier gain, and ball screw and gear transmission gain (if there is any) [73].

Following the rapid identification formulation in [73], the parameter estimation steps in Eqs. (3.4)-(3.7) utilize the time-integral of the tracking error. Hence, the denominator polynomial is expressed with the lowest order term (a_3) coinciding with $s^{-1} = 1/s$. Multiplying the numerator and denominator with (s) naturally yields a form similar to Eq. (3.10).

Errors caused by friction become prevalent during velocity reversals because the feedback controller cannot compensate sudden changes in the disturbance force. As the velocity of the feed drive transitions through zero, the friction force (which is very close to being in the pre-sliding regime) quickly changes

its direction. Here, to simplify the model, only Coulomb type friction is considered to approximate the overall detrimental effect of friction dynamics. This type of friction model can be formulated as:

$$d = d^+PV(\dot{x}) + d^-NV(\dot{x}),\tag{3.2}$$

where $PV(\ )$ is a binary function which has a value of "1" when the axis velocity is positive and "0", otherwise, while $NV(\ )$ is a binary function which has a value of "1" when the axis velocity is negative and "0" otherwise. The control signal equivalent values for the Coulomb friction are modelled as d^+ and d^- for the positive and negative directions of motion, respectively. From here onwards, adopting the operator 's' as differentiation with respect to time and '$1/s$' as integration with respect to time, the closed-loop dynamics can be expressed by combining Eqs. (3.1) and (3.2):

$$\left[s^2 + a_1 s + a_2 + a_3 \frac{1}{s}\right] x = \left[b_0 s^2 + b_1 s + b_2 + a_3 \frac{1}{s}\right] x_r - [PV(\dot{x})d_n^+ + NV(\dot{x})d_n^+]\tag{3.3}$$

Above, d_n^+ and d_n^- are normalized friction values for positive and negative velocities, respectively, and can be obtained as $d_n^{+/-} = (K/J)d^{+/-}$. From Eq. (3.3), in discrete-time form, the position of the drive at sample k can be predicted as:

$$\hat{x}_k = \alpha_i e_{i,k} - \alpha_1 \dot{x}_k - \alpha_2 \ddot{x}_k + \beta_0 x_{r,k} + \beta_1 \dot{x}_{r,k} + \beta_2 \ddot{x}_{r,k} - PV(\dot{x}_k)\delta^+ - NV(\dot{x}_k)\delta^-\tag{3.4}$$

$$\left.\begin{aligned}
\alpha_2 &= 1/a_2, & \alpha_1 &= a_1/a_2, & \alpha_i &= a_3/a_2, \\
\beta_2 &= b_0/a_2, & \beta_1 &= b_1/a_2, & \beta_0 &= b_2/a_2, \\
\delta^+ &= d_n^+/a_2, & \delta^- &= d_n^-/a_2,
\end{aligned}\right\}\tag{3.5}$$

where $\alpha_i, \alpha_1, \alpha_2, \beta_0, \beta_1, \beta_2, \delta^+, \delta^-$ are the normalized model parameters with respect to a_2. Commanded and actual axis position (x_r, x), velocity $(\dot{x}_r. \dot{x})$ and acceleration $(\ddot{x}_r, \ddot{x})$ profiles can be captured on the fly in most machine tool systems. In Eq. (3.4), e_i is the integrated tracking error, which can be approximated as:

$$e_{i,k} = T_s \sum_{m=1}^{k} (x_{r,m} - x_m)\tag{3.6}$$

Note that $\hat{x}_k = \hat{x}(kT_s)$, where T_s is the discrete time sampling period. Using classical LS, the 8 unknown parameters can be found by minimizing [93],

$$Minimize \; f = \frac{1}{2}(Y - \Phi\theta)^T(Y - \Phi\theta)$$

$$Y = [x_1 \; x_2 \; ... \; x_N]^T$$

$$\theta = [\alpha_i \; \alpha_1 \; \alpha_2 \; \beta_0 \; \beta_1 \; \beta_2 \; \delta^+ \; \delta^-]^T \qquad (3.7)$$

$$\Phi = \begin{bmatrix} e_{i,1} & -\dot{x}_1 & -\ddot{x}_1 & x_{r,1} & \dot{x}_{r,1} & \ddot{x}_{r,1} & -PV(\dot{x}_1) & -NV(\dot{x}_1) \\ e_{i,2} & -\dot{x}_2 & -\ddot{x}_2 & x_{r,2} & \dot{x}_{r,2} & \ddot{x}_{r,2} & -PV(\dot{x}_2) & -NV(\dot{x}_2) \\ \vdots & \vdots & \vdots & \vdots & \vdots & \vdots & \vdots & \vdots \\ e_{i,N} & -\dot{x}_N & -\ddot{x}_N & x_{r,N} & \dot{x}_{r,N} & \ddot{x}_{r,N} & -PV(\dot{x}_N) & -NV(\dot{x}_N) \end{bmatrix}$$

as

$$\theta = (\Phi^T\Phi)^{-1}\Phi^TY \qquad (3.8)$$

Here, θ is the parameter vector with all unknown parameters, Y contains axis position measurements, and Φ is the regressor matrix, made up of signals available for measurement. In earlier work, to observe the performance of the drive over various feedrates, a short NC code with pseudo-random movements would be executed. By executing several back and forth movements on the machine and inducing trajectories with different acceleration and velocity, motor torque/force amplitude dependency of the system's response caused by Coulomb friction could be reasonably captured. While generally successful, there are some drawbacks to this earlier approach:

1- The commanded signals in CNC systems are typically acceleration-continuous and lack the persistence of excitation (PE) for full parameter convergence. This deteriorates the prediction accuracy of identified models and can, in some cases, also lead to unstable models.

2- The formulation in Eq. (3.7) requires numerical derivatives of measured encoder signals in the regressor matrix Φ, which typically leads to noise sensitivity issues. This is true especially if low resolution encoders are used, or the captured CNC data is limited in the number of significant digits available in the controller's trace function.

To avoid the issue of identifying unstable models due to lack of PE, earlier research [70][73][74] had imposed bounds which define acceptable pole locations as being sufficiently away from the imaginary axis of the s-plane. Considering that the characteristic polynomial can be written as $s^3 + a_1s^2 + a_2s + a_3 = (s + p)(s^2 + 2\zeta\omega_n s + \omega_n^2)$, the following constraints were integrated into the estimation process:

$$\text{Constraints:} \quad \begin{array}{cc} p_{min} \leq p \leq p_{max} & \omega_{n,min} \leq \omega_n \leq \omega_{n,max} \\ \zeta \geq \zeta_{min} & \zeta \leq \zeta_{max} \end{array} \qquad (3.9)$$

In earlier experimental and simulation studies [73], it was observed that for majority of the cases, solution of the unconstrained estimation problem in Eq. (3.7) resulted in pole locations which already satisfied the constraints in Eq. (3.9). In other words, solving the unconstrained problem alone yielded the equivalent result to merging Eqs. (3.7) and (3.9) and solving the constrained problem via a method like Lagrange Multipliers. Thus, in the benchmark simulation and experimental studies presented in this thesis, the earlier method in [73] was implemented by first solving the unconstrained 8-parameter estimation problem in Eq. (3.7), and then checking the compliance of the solution with the constraint set in Eq. (3.9) afterwards. If this check passes, then Kuhn-Tucker conditions required for analyzing the constraint activation scenarios are by-passed, thereby greatly simplifying the implementation. In this thesis, such implementation of the earlier method has been referred to as the 'Full LS Solution'.

3.5. Proposed New Solution: Pole Search in Conjunction with Least Squares Projection

The goal of the proposed identification method is to enhance the convergence and robustness in estimating a CNC drive system's dynamic model. In the new method, the instantaneous tracking error $(e = x_r - x)$ in each axis is directly predicted, rather than the axis position itself:

$$e(s) = \underbrace{\frac{(c_0 s^2 + c_1 s + c_2)s}{s^3 + a_1 s^2 + a_2 s + a_3}}_{G_{e,x_r}(s)} x_r(s) - \underbrace{\frac{(K/J)s}{s^3 + a_1 s^2 + a_2 s + a_3}}_{G_{e,d}(s)} d(s)$$

(3.10)
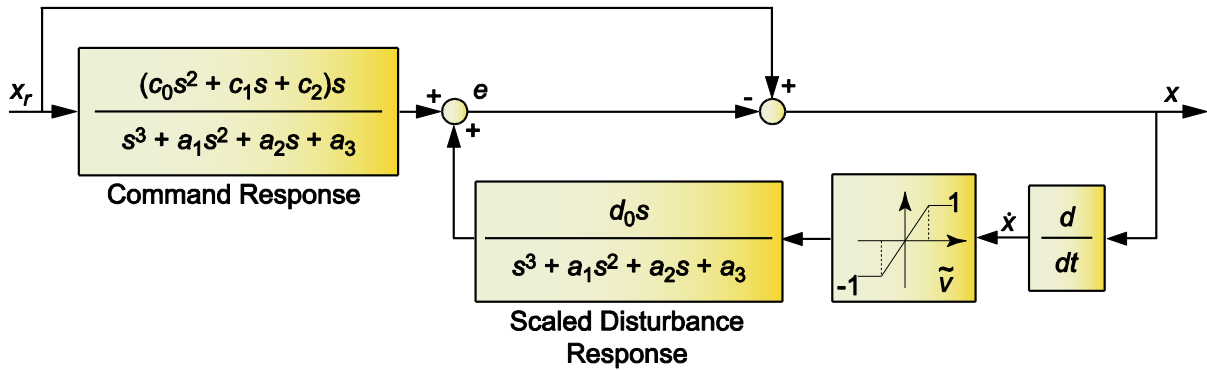
Fig. 3.5. Closed-loop model for predicting tracking error and feed drive position.

$$\left. \begin{aligned} c_0 &= 1 - b_0, \\ c_1 &= a_1 - b_1, \\ c_2 &= a_2 - b_2 \end{aligned} \right\}$$

(3.11)

Prediction of the servo error (e) and axis position (x) is illustrated in Fig. 3.5. For numerical estimation and simulation convenience in the new method, the friction at small velocities is approximated as being viscous, while beyond a certain velocity threshold ($\tilde{v}$) it is modeled as Coulomb friction.

$$d(t) = d_0' sat(\dot{x}/\tilde{v}) \tag{3.12}$$

Above, d_0' is the control input normalized Coulomb friction value for both positive and negative motion directions and $\tilde{v}$ is the velocity band for transitioning to Coulomb friction. Lumping the friction magnitude d_0' together with the gain of the disturbance response K/J, a single gain can be defined as $d_0 = d_0'K/J$ pertaining to the disturbance response for a scaled friction input between -1 … +1. In the *estimation* step, since numerically differentiated position readings from the machine encoder can be noisy, even after filtering, a pure sign( ) function may lead to false detection of sudden friction force transitions. On the other hand, when a block diagram like the one in Fig. 3.5 is used for *simulating* the axis motion and servo errors, pure Coulomb friction, which transitions discontinuously around zero velocity, can lead to limit cycle type oscillations when coupled with the feedback loop [94]. Thus, it was found that using a saturation function, which emulates viscous type friction behavior around very small velocities, provides a practical workaround to both problems, while still facilitating close enough parameter estimation and tracking error prediction due to the friction force. Substituting Eq. (3.12) into Eq. (3.10), the following expression is obtained in which the characteristic polynomial $P(s)$ has also been designated:

$$\underbrace{(s^3 + a_1 s^2 + a_2 s + a_3)}_{P(s)} e = (c_0 s^2 + c_1 s + c_2)sx_r + s[d_0 sat(\dot{x}/\tilde{v})] \tag{3.13}$$

For a candidate model, if the pole locations are already chosen in the structure: $P(s) = s^3 + a_1 s^2 + a_2 s + a_3 = (s + p)(s^2 + 2\zeta\omega_n s + \omega_n^2)$, then the numerator terms and lumped friction magnitude can be estimated following a LS sub-problem constructed by re-arranging Eq. (3.13) into the form below:

$$
\begin{aligned}
e &= \frac{c_0 s^3}{P(s)}x_r + \frac{c_1 s^2}{P(s)}x_r + \frac{c_2 s}{P(s)}x_r + \frac{s}{P(s)}\left[d_0 sat\left(\frac{\dot{x}}{\tilde{v}}\right)\right]\\
&= \underbrace{\frac{s^3 x_r}{P(s)}}_{\dddot{x}_{rf}}c_0 + \underbrace{\frac{s^2 x_r}{P(s)}}_{\ddot{x}_{rf}}c_1 + \underbrace{\frac{sx_r}{P(s)}}_{\dot{x}_{rf}}c_2 + \underbrace{\frac{s}{P(s)}sat\left(\frac{\dot{x}}{\tilde{v}}\right)}_{d_{nf}}d_0
\end{aligned}
\tag{3.14}
$$

In practical implementation, the actual axis velocity ($\dot{x}$) is replaced by the measured and filtered velocity estimate ($\dot{x}_f$) determined through differentiation and moving average filtering of the encoder readings with zero phase shift with respect to time (e.g., by using the '*filtfilt*' command in Matlab). This substitution helps mitigate noise issues in resolving the direction of the instantaneous friction force, especially at small velocities.

Due to the consideration of predominantly rigid body dynamics and integral action in the control law, the characteristic polynomial $P(s)$ is third order. Thus, the filtered velocity, acceleration, and jerk command profiles, $\dot{x}_{rf}$, $\ddot{x}_{rf}$, $\dddot{x}_{rf}$ will all be continuous as long as x_r is continuous.

Output of the saturation function will be 0th degree continuous. However, its filtering through $s/P(s)$ will add two more degrees of continuity. This signal, d_{nf}, can be considered as a normalized friction force (between -1 and +1), which has been 'filtered' through the closed loop system's characteristic response and differentiated once.

In contrast to the earlier estimation method described in Section 3.3, which requires up to second order differentiation of both command signals and encoder (position) readings, in the new approach all signals considered in the regressor matrix are continuous and they do not suffer from noise or numerical round-off error amplification problems induced by the differentiation process. Grouping the observed tracking errors into an output vector ($Y = [e_1 \ e_2 \ \cdots \ e_N]^T$) and defining the regressor matrix in the form:

$$\Phi_2 = \begin{bmatrix} \dddot{x}_{rf,1} & \ddot{x}_{rf,1} & \dot{x}_{rf,1} & d_{nf,1} \\ \dddot{x}_{rf,2} & \ddot{x}_{rf,2} & \dot{x}_{rf,2} & d_{nf,2} \\ \vdots & \vdots & \vdots & \vdots \\ \dddot{x}_{rf,N} & \ddot{x}_{rf,N} & \dot{x}_{rf,N} & d_{nf,N} \end{bmatrix} \tag{3.15}$$

The estimation of the numerator terms and lumped friction magnitude can be achieved as:

$$\theta_2 = [c_0 \ c_1 \ c_2 \ d_0]^T = (\Phi_2^T \Phi_2)^{-1} \Phi_2^T Y \tag{3.16}$$

Step 1. Construct denominator polynomial $P(s)$ by taking candidate poles $(p, \omega_n, \zeta)_k$ from stable location.

Step 2. Compute regressors to estimate numerator $(c_0, c_1, c_2)_k$ & disturbance $(d_0)_k$.

Disturbance Regressor

Measured Velocity Signal (Filtered) $\xrightarrow{\dot{x}_f}$ | | $\dfrac{s}{P(s)}$ $\xrightarrow{d_{nf}}$ Φ_d

Command Trajectory

$\dfrac{s}{P(s)}$ $\xrightarrow{\dot{x}_{rf}}$ Φ_1

$\dfrac{s^2}{P(s)}$ $\xrightarrow{\ddot{x}_{rf}}$ Φ_2

$\dfrac{s^3}{P(s)}$ $\xrightarrow{\dddot{x}_{rf}}$ Φ_3

Tracking Regressors

Step 3. Least squares solution of parameters $(c_0, c_1, c_2, d_0)_k$.

Parameter Estimation

Regressor $\longrightarrow$ $\theta_k = (\Phi_k^T \Phi_k)^{-1} \Phi_k^T Y$

$$Y = [e_1 \ e_2 \ \cdots \ e_N]^T$$

$$\Phi_{2,k} = \begin{bmatrix} \dddot{x}_{rf,1} & \ddot{x}_{rf,1} & \dot{x}_{rf,1} & d_{nf,1} \\ \dddot{x}_{rf,2} & \ddot{x}_{rf,2} & \dot{x}_{rf,2} & d_{nf,2} \\ \vdots & \vdots & \vdots & \vdots \\ \dddot{x}_{rf,N} & \ddot{x}_{rf,N} & \dot{x}_{rf,N} & d_{nf,N} \\ \underbrace{}_{\Phi_3} & \underbrace{}_{\Phi_2} & \underbrace{}_{\Phi_1} & \underbrace{}_{\Phi_d} \end{bmatrix}$$

$$\theta_{2,k} = [\ c_0 \ c_1 \ c_2 \ d_0\ ]^T$$

Step 4. Choose candidate model $(p, \omega_n, \zeta)_k \longrightarrow (c_0, c_1, c_2, d_0)_k$ which yields the lowest value for the RMS of prediction error.

$$f = \sqrt{\frac{1}{N} \sum_{k=1}^{N} (e_{actual} - e_{pred})^2}$$

Fig. 3.6. Proposed new procedure for identifying virtual feed drive dynamics.

36

Hence, the following step-by-step procedure has been developed for implementing the proposed identification scheme, as also illustrated in Fig. 3.6:

1- Candidate models are generated with pre-assigned stable pole locations within a search-space.
2- After constructing the corresponding regressor, the best-fitting numerator and friction parameters are solved using LS projection [93].
3- Each candidate model is evaluated for how well it is able to replicate the observed tracking error profile for an individual axis, by assessing the objective function which penalizes the root mean square of the prediction error.

$$f = \sqrt{\frac{1}{N} \sum_{k=1}^{N} (e_k - \hat{e}_k)^2} \tag{3.17}$$

4- The pole set (and matching numerator and friction parameters) which yield the best result are selected to establish the 'identified model'.

In Eq. (3.17), e_k and $\hat{e}_k$ are the actual (experimental) and predicted tracking errors respectively, and N is the total number of samples considered in the model fitting and evaluation process.

3.6.   Simulation Results

3.6.1.   Performance Analysis of Identification Approaches under Measurement Noise

In this section, the proposed identification technique's advantages (robustness, consistency etc.) has been compared to the earlier approach [73]. This analysis has been implemented in the context of reconstructing the dynamics of a P-PI position-velocity cascade controlled drive system when the output (e.g., position, x) measurement is contaminated with sensor noise (e.g., quantization). The controller structure, shown in Fig. 3.7, is frequently used in industrial machine tools.

Fig. 3.7. P-PI position-velocity cascade control structure.

In this case, the third order closed loop model parameters correlate to the individual open loop and control law parameters through the following relationships:

$$
\left.
\begin{aligned}
a_1 &= \frac{B + KK_{pv}}{J} & a_2 &= \frac{K(K_{pv}K_{px} + K_i)}{J} \\
a_3 &= \frac{KK_{px}K_i}{J} & b_0 &= \frac{KK_a}{J} \\
b_1 &= \frac{KK_{pv}K_v}{J} & b_2 &= \frac{K(K_{px}K_{pv} + K_vK_i)}{J}
\end{aligned}
\right\}
\tag{3.18}
$$

The above formulation for denominator and numerator parameters belongs to the tracking transfer function $(x_r \rightarrow x)$ form considered in Eq. (3.1). In evaluating the tracking error response to the commanded trajectory $(x_r \rightarrow e)$ as in Eq. (3.10), c_0, c_1, and c_2 terms can be calculated using Eq. (3.11).

The model was developed based on the x-axis drive of the DMG machine tool explained earlier in this chapter. By inspecting the CNC parameters, it was found out that the acceleration and velocity feedforward gains had been set to zero. Thus, in the simulation, they were also set to be disabled ($K_a = 0$, $K_v = 0$). The effect of true friction is emulated by applying the GMS friction model [43][95]. Prediction results were based off data generated during the tracking type trajectory with increasing amplitude. The maximum displacement was 11 mm, with peak velocity acceleration, and jerk values reaching 96 mm/s, 4514 mm/s^2, and 3.82×10^6 mm/s^3, respectively. In Fig. 3.8, the true system's response has been illustrated. In this figure, measured position profile, tracking error with max 1.3 mm amplitude and command velocity profile are shown.

Three levels of measurement noise have been considered, in the form of encoder quantization: 1, 5 and 10 μm. In these scenarios, the velocity and acceleration estimates obtained by differentiation, after

quantization of the position response, take the forms shown in Fig. 3.9. As can be seen in Eq. (3.7), since the full LS approach requires the "measured" velocity ($\dot{x}$) and acceleration profiles ($\ddot{x}$), in identifying the necessary 8 parameters, the measurement noise can have a significant detrimental influence on the parameter convergence. Whereas in the proposed approach, the regressor matrix (Φ_2) contains profiles which are smoothened by the filter $P(s)$ based on the choice of candidate pole locations. Thus, measurement noise has much less impact, influencing only the 4th column of Φ_2, attributed to the estimated normalized Coulomb friction. Even this profile gains two levels of continuity due to the preceding $s/P(s)$ term in Eq. (3.14). Considering Fig. 3.9, the magnitude of the velocity profiles does not vary too much from one case to another, as only resolution deteriorates significantly as quantization level increases. However, maximum detected acceleration changes drastically, from 2.1×10^3 to 1.4×10^4 mm/sec^2 due to the detrimental influence of quantizing the position measurements prior to double differentiation. As will be seen in the following convergence results, the full LS identification approach suffers significantly from the noise contamination in the measurement signal.

Examining the true and estimated frequency response functions (FRFs) in Fig. 3.10, as the measurement noise increases, the dynamics estimation via the Full LS deteriorates significantly, especially after 25 Hz, whereas the proposed approach achieves much more consistent estimation of the disturbance and tracking dynamics.
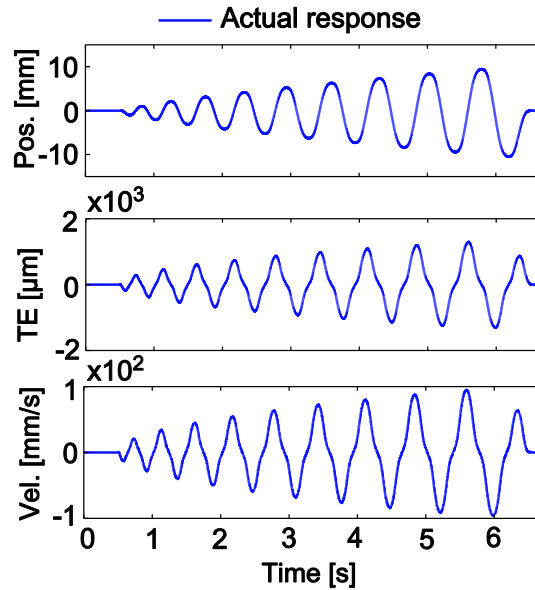
Fig. 3.8. The true system's response (simulation).
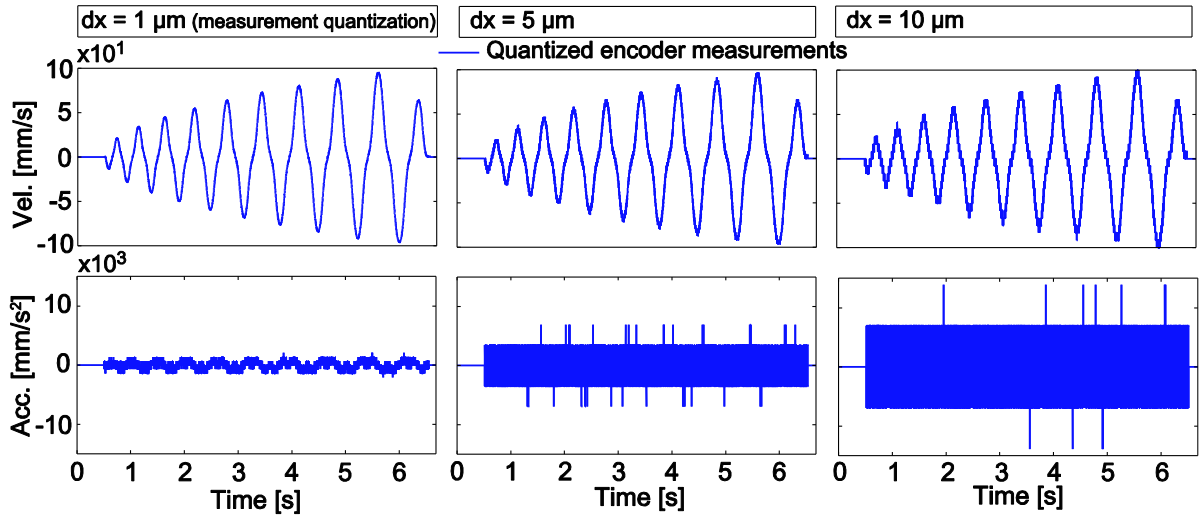
Fig. 3.9. Velocity and acceleration profiles for different quantization levels.
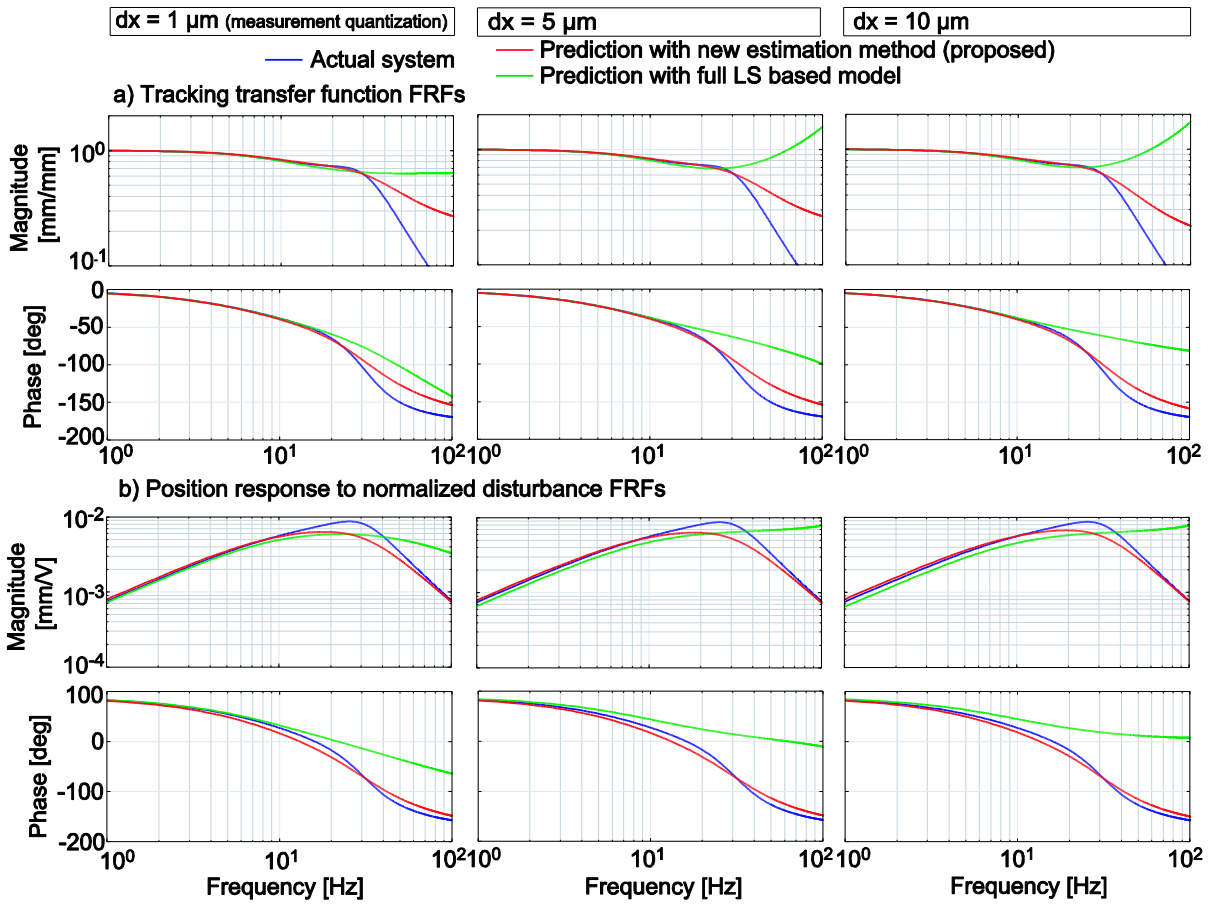
Fig. 3.10. The true and estimated command tracking and disturbance response FRF's.

Comparing the 2-norm condition number for the regressor matrices in the two approaches reveals that compared to the full LS approach, the proposed pole search method solves a least squares sub-problem that is much better numerically conditioned (Table 3.1). This is because the measured velocity and acceleration profiles, constituting the 2nd and 3rd columns of Φ, are obtained by numerical differentiation of the quantized position measurements. They are noisy due to the simulated encoder resolution, and get worse as this resolution (dx) becomes coarser.

Table 3.1. Condition numbers for full LS and proposed method.

Condition number	dx = 1 μm	dx = 5 μm	dx = 10 μm
Full LS (Φ)	8.8×10^6	7.8×10^6	10.5×10^6
Proposed method (Φ_2)	508.3	577.2	734.3

It is worth mentioning that in the dx = 10 μm case, the full LS approach even converges to an unstable model (Fig. 3.11), when the pole bounds in Eq. (3.9) are not directly enforced. A pair of unstable complex conjugate poles are estimated with $\omega_n = 233.41$ Hz and $\zeta = -0.028$.
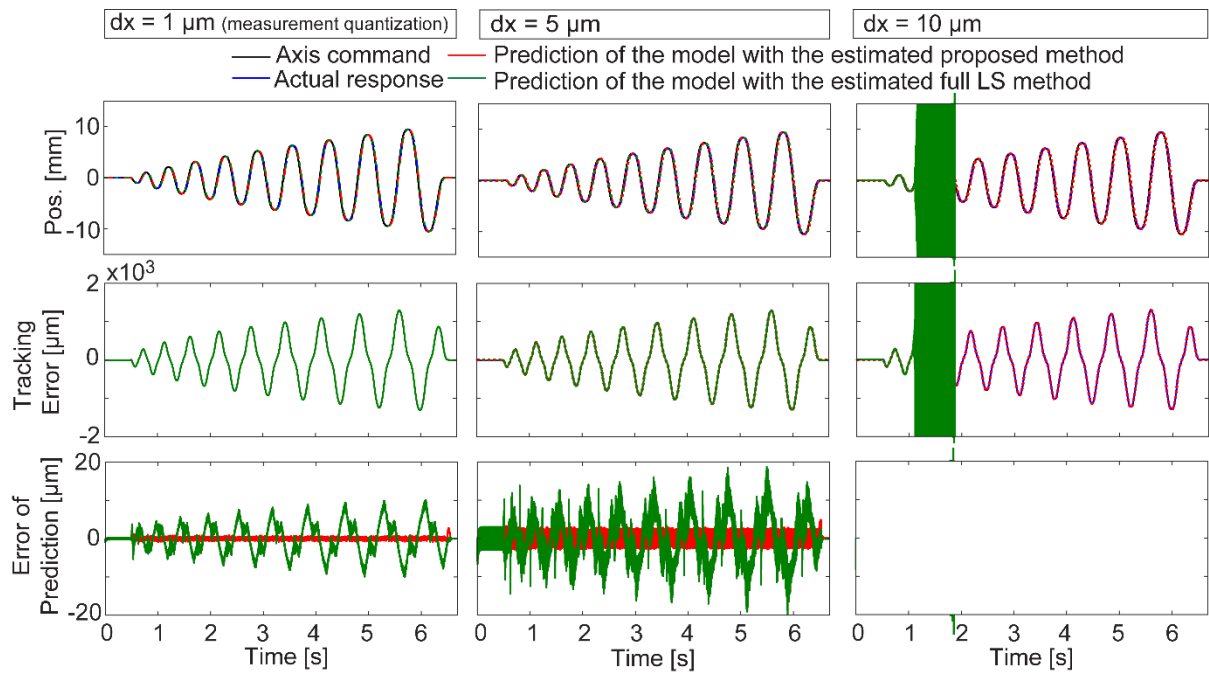
Fig. 3.11. Actual and predicted servo performance for sine wave type trajectory with increasing amplitude (simulation result).

In Fig. 3.11, position, tracking error and error of prediction results are given for three different quantization cases. For dx = 1 and dx = 5 μm, the proposed approach shows much less error of prediction compared to the full LS approach. When dx = 10 μm, the full LS converges to an unstable model. As a result, the proposed algorithm indeed provides much more robust, consistent, and well-conditioned model estimation, compared to the full LS approach, especially in the presence of measurement noise. Unconstrained LS alone cannot guarantee the estimation of a stable model, especially when there is noise in the measurement, and therefore the enforcement of stable pole locations is essential.

3.6.2.   Estimation and Simulation Improvement via the Saturation Function

In developing the identification strategy in Section 3.5, the Coulomb friction was approximated with a saturation function. In this subsection, the impact of the saturation function on the identification and simulation results is investigated. For the same actual system model, and motion trajectory, with Section 3.6.1, and considering a measurement resolution of dx = 5 μm, model identification was performed considering both the saturation function and a sign (signum) function. The model identification results are shown in Fig. 3.12 and Table 3.2. In terms of matching the real system's frequency response characteristics, using the saturation function seems to yield similar results, with albeit slightly improved characteristics, over using the signum function. Noticeably, the real system's complex conjugate pole pair at 31.31 Hz is better captured at 31.47 Hz, compared to 26.48 Hz using the signum function. The estimated normalized friction magnitude (293) also better matches its true value (286), compared to its counterpart (202) in the model estimated with the signum function.

In simulating the model's dynamic response, use of saturation versus signum function is also compared for the same dynamic model and trajectory. In this case, the measurement quantization has been removed. The corresponding results are shown in Fig. 3.13 and Table 3.3. In the simulations, the use of the saturation function provides improvement of the tracking error prediction, especially at velocity reversals. On the whole, 6.7% improvement is obtained in the RMS value for the error of prediction. However, at the very beginning and very end of the motion (i.e., connecting to exact zero velocity boundary conditions), the prediction accuracy degrades by 21%. Naturally, the real nature of stick slip friction (which is simulated accurately in the true model using the GMS dynamics), cannot be fully captured with the saturation-based friction model. Nevertheless, in majority of the data in which motion is persistent, improvement is observed over using the signum function to emulate Coulomb friction.
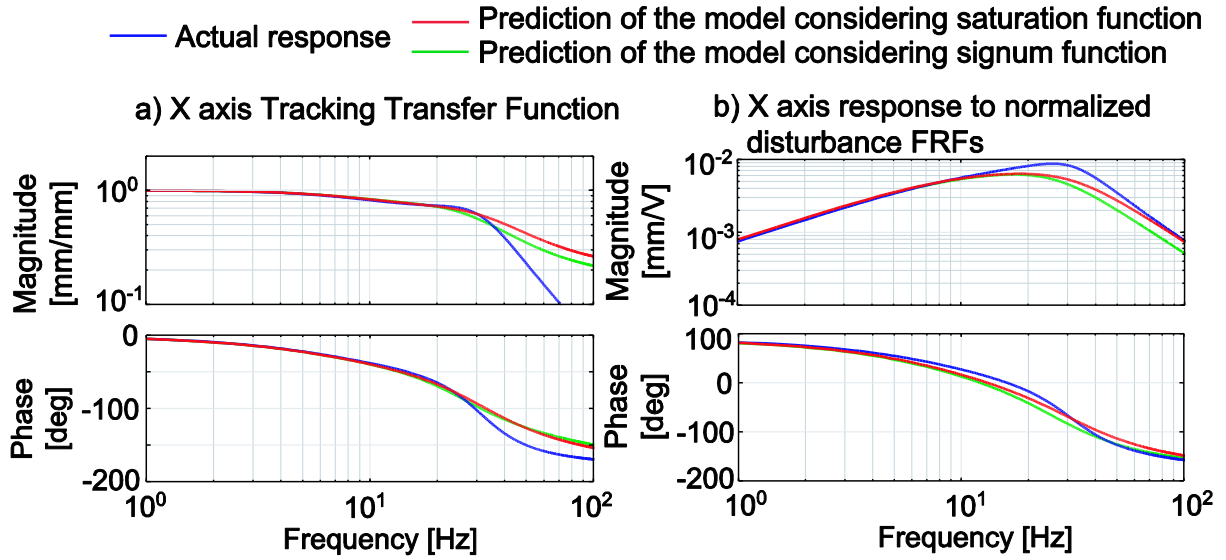
Fig. 3.12. Actual and predicted servo performance using saturation and signum functions for approximation of friction (5 μm quantization).

Table 3.2. Identified parameters for the models that contain saturation and signum functions.

X axis	Actual Freq. [Hz]	Actual Damping [ ]	Saturation Freq. [Hz]	Saturation Damping [ ]	Signum Freq. [Hz]	Signum Damping [ ]
Poles						
p_1	31.31	0.44	31.47	0.71	26.48	0.66
p_2	31.31	0.44	31.47	0.71	26.48	0.66
p_3	9.87	1.00	9.41	1.00	9.41	1.00
Zeros						
z_1	21.88	1.00	57.66	-1.00	64.73	-1.00
z_2			50.02	1.00	33.78	1.00
z_3			15.88	1.00	17.72	1.00
Normalized friction (d_0)	286		293		202	
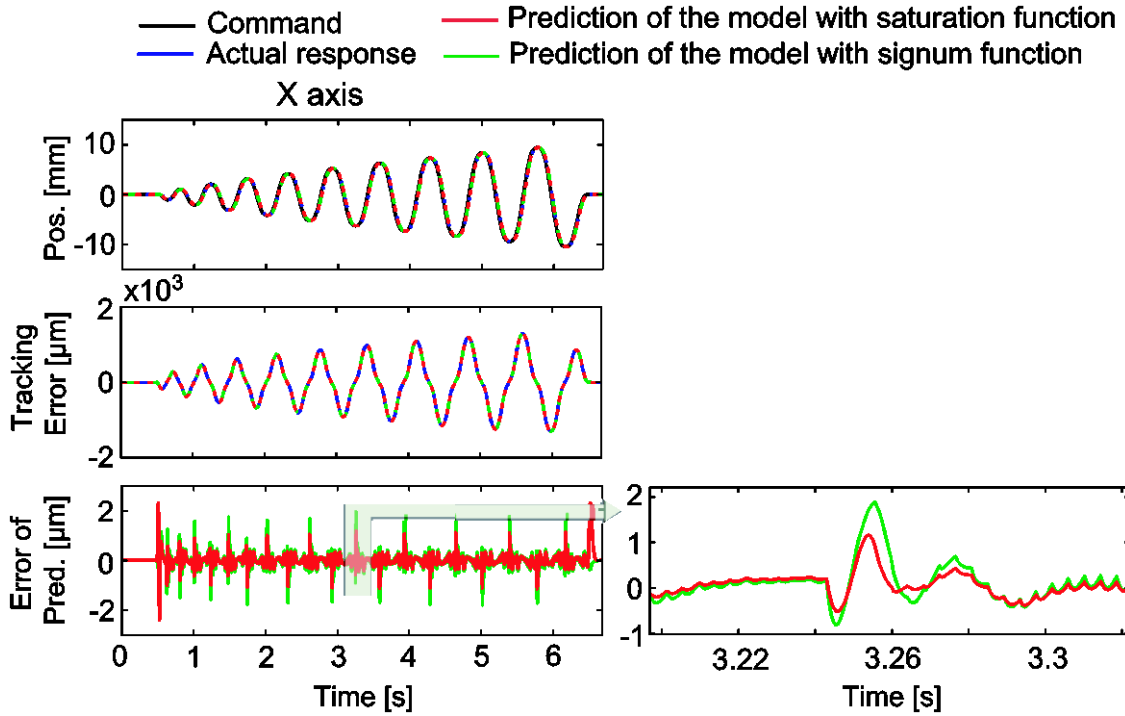
Fig. 3.13. Actual and predicted servo performance using saturation and signum functions for approximation of friction (without quantization).

Table 3.3. Tracking prediction performance for two different cases.

Discrepancy in Servo Error Prediction	Saturation	Signum
X axis tracking error: RMS (MAX) [μm]	0.28　(2.40)	0.30　(1.89)

3.7. Experimental Results

In this section, experimental validation of the proposed identification method is presented for the aforementioned two different applications. Comparison is also made with the full LS method.

3.7.1. Gear Form Grinding Application

Servo data was collected from the Siemens 840D controller of the grinding machine (Fig. 3.1) during the production of helical gears with 1.67 mm normal module. The portion of data corresponding to the roughing pass performed at nominal feed was used in identifying the virtual drive parameters. Model validation was carried out with both roughing and finishing pass data. Each roughing and finishing operation has 3-4 passes, which are nearly periodic. The sampling period, allowed by the 840D for data collection, was 4 ms. Position measurement resolution from the encoders was 0.01 μm. In inspecting

the CNC parameters for this machine, it was determined that while acceleration feedforward gain (K_a) was set to zero, the velocity feedforward gain was present and non-zero ($K_v \neq 0$).
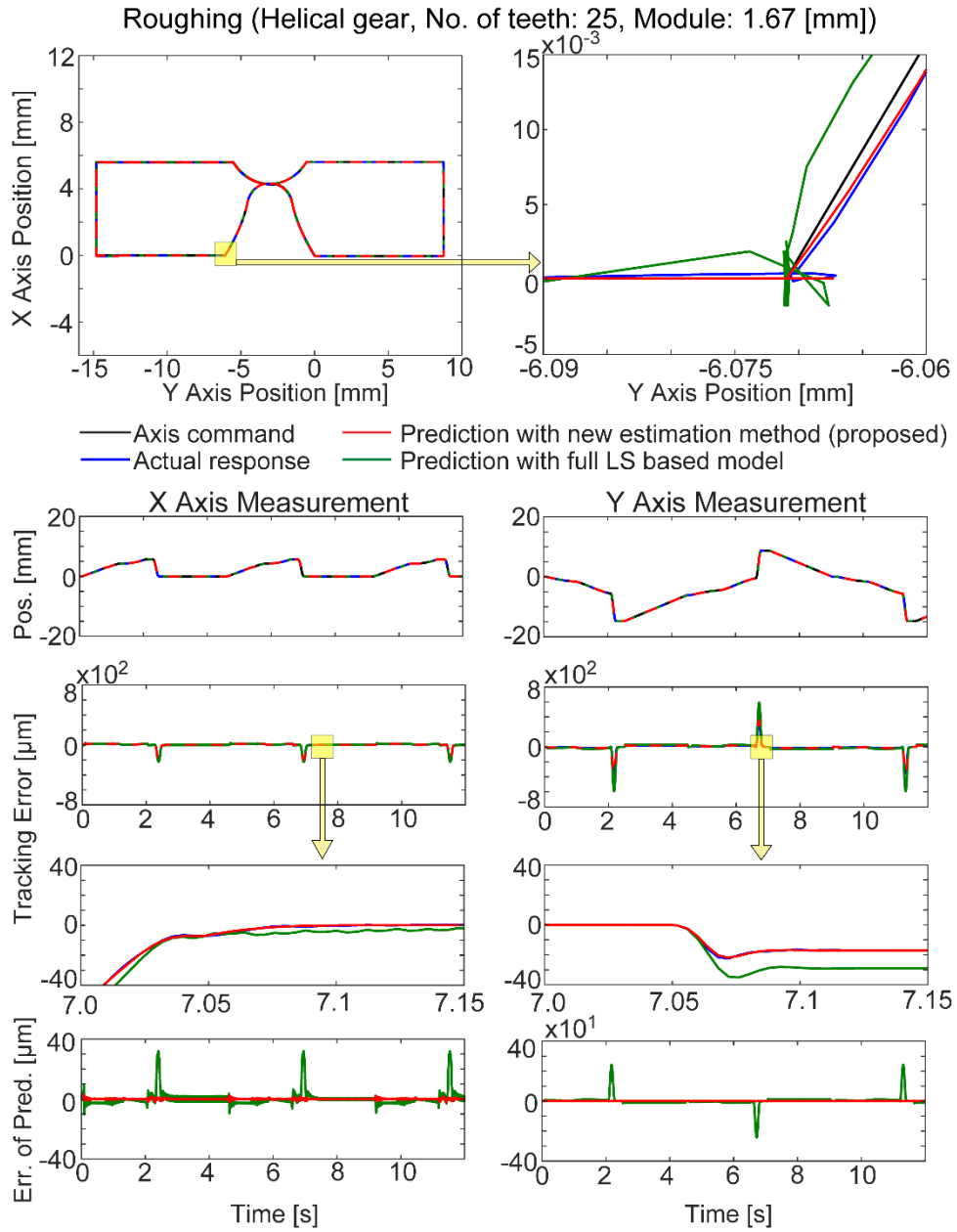
Fig. 3.14. Actual and predicted servo performance for form grinding wheel rough dressing.

Table 3.4. Kinematic values (in tangential direction) for rough and finish dressing operations.

Maximum Values in the Tangential Direction	Rough Dressing		Finish Dressing	
	Complete Trajectory	Involute Portion	Complete Trajectory	Involute Portion
Feedrate [mm/s]	93.5	4.4	108.1	1.6
Tangential acc. [mm/s^2]	1,550	105	1,550	1
Tangential jerk [mm/s^3]	40,073	8,977	40,084	242

The training data, shown in Fig. 3.14, was ~12 s in duration for each roughing pass (3000 samples). Maximum feedrate, tangential acceleration, and jerk magnitudes reached during the dressing operation, for the positioning trajectory and critical involute (i.e., gear tooth gap) portion, are summarized in Table 3.4. This table considers rough and finish dressing passes. As seen, there is 1-2 orders of magnitude reduction in feed and acceleration during the involute portion, particularly in finish dressing.

The pole search bounds and obtained closed loop parameters for the x- and y-axes are shown in Table 3.5 and Table 3.6. Predictions obtained for rough and finish dressing passes, with the proposed method and via the full LS approach, are presented in Fig. 3.14 and Fig. 3.15. Numerical comparison of the tracking and contouring error predictions for both methods are presented in Table 3.7.

Table 3.5. Pole search bounds for x-y axes of Kapp KX300P machine tool.

Parameters	Min	Max
p [Hz]	1	125
ω_n [Hz]	1	125
ζ []	0.2	2

Table 3.6. Identified parameters for x-y axes of Kapp KX300P machine tool.

Parameter	X Axis	Y Axis
p [Hz]	8.20	6.41
ω_n [Hz]	28.30	32.02
ζ []	0.29	0.8
c_0	1.51	2.33
c_1	147.26	212.72
c_2	6.32e+03	6.32e+03
d_0	75.47	108.26

46
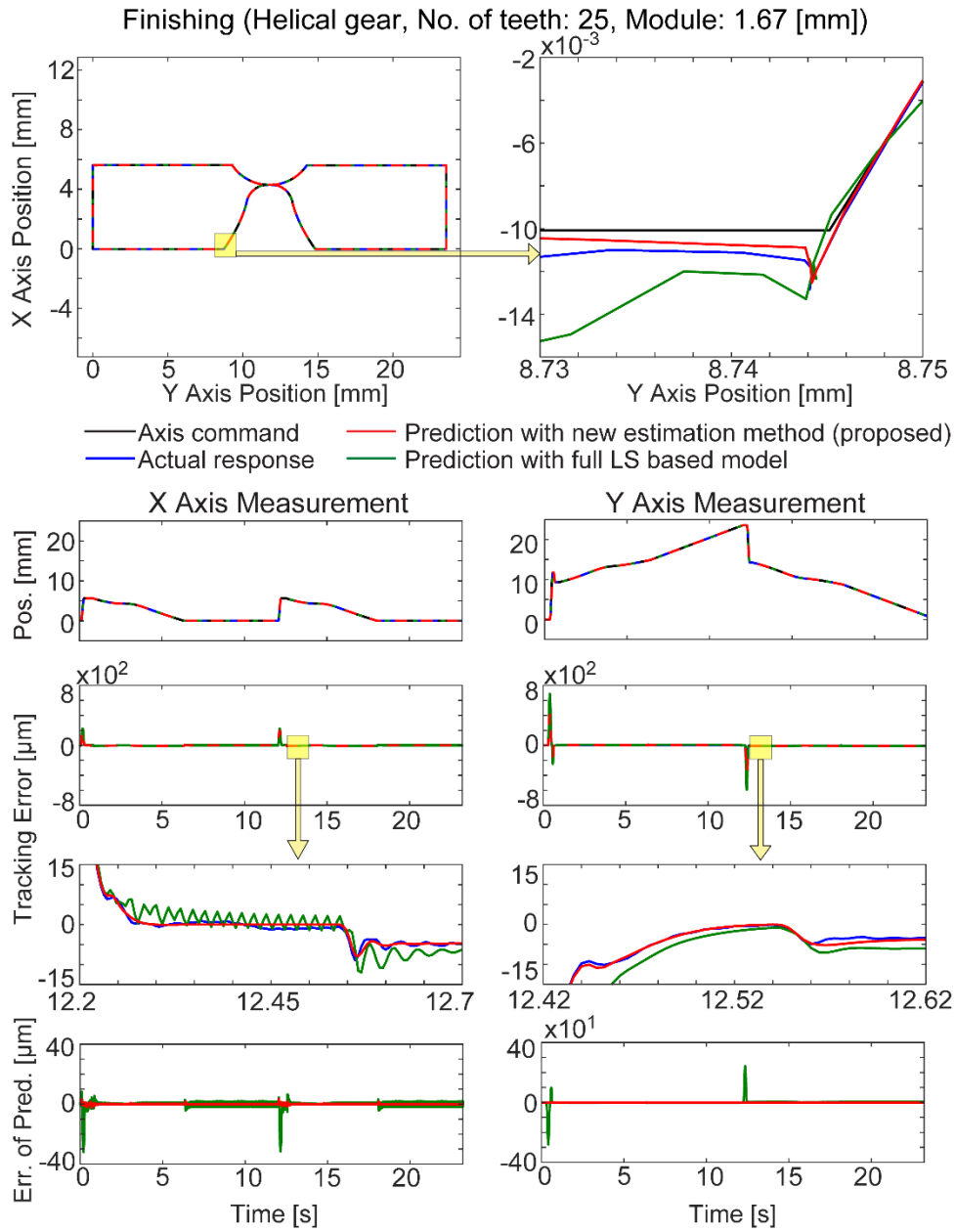
Fig. 3.15. Actual and predicted servo performance for form grinding wheel finish dressing.

Comparing the x- and y-axis parameters in Table 3.6, it is seen that the two axes appear to have somewhat similar dynamics, as would be expected in a well-tuned machine tool. There is, however, discrepancy in the damping ratios. This may be possible if predominantly time-domain tuning of the control system was realized with a smooth trajectory, which prevents the excitation of oscillatory behavior.

47
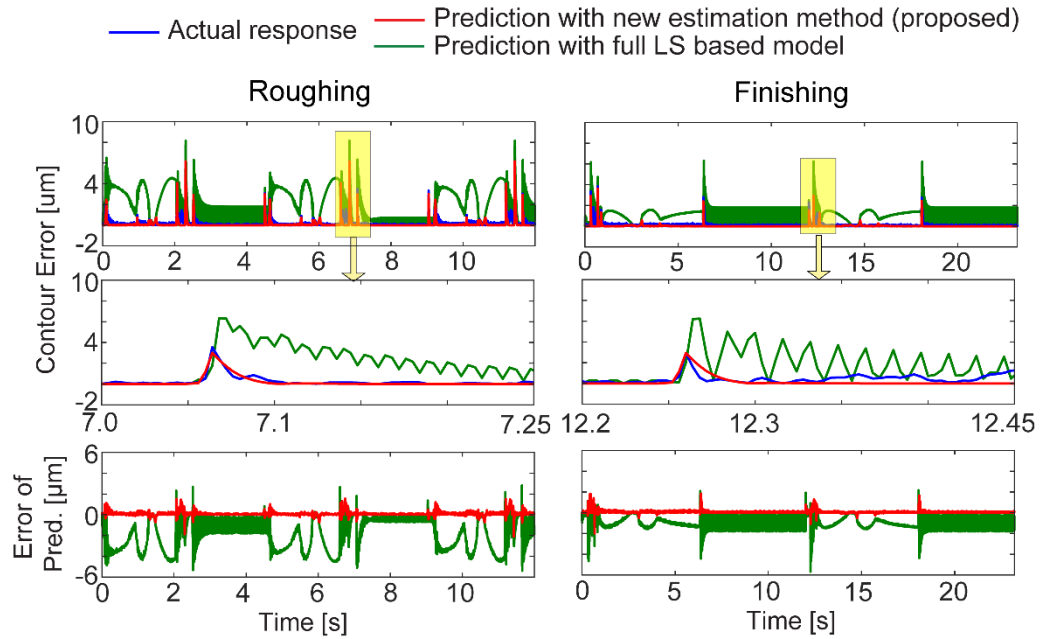
Fig. 3.16. Actual and predicted contour errors for rough and finish dressing.

Considering Fig. 3.14 and Fig. 3.15, some results similar to those observed in the simulations section can be spotted. For example, both methods are able to generate a model which captures the general trend in the tracking errors. However, looking closer at zoomed portions of the tracking error, it is seen that the model identified with proposed method yields significantly closer prediction. Also, the transient response, determined by the pole frequency and damping ratio, is predicted more consistently, as seen on left hand side of Fig. 3.15 (i.e., zoomed x-axis tracking error profile). The full LS based model, on the other hand, seems to incorrectly predict a more oscillatory response. Overall, the model obtained with the proposed method yields significantly better prediction of transients in the toolpath and of contouring errors, for rough and finish dressing operations, as seen in the top right panels of Fig. 3.14, Fig. 3.15, and in Fig. 3.16.

As observed in Table 3.7, by migrating from full LS to the proposed approach, the discrepancy in tracking error prediction has been mitigated from a range of 32-280 to 1.8–3.4 μm, considering maximum magnitudes. This corresponds to 1-2 orders of improvement. Accuracy of contouring error prediction has been improved, from 5.4-5.7 to 2.0-2.1 μm, again considering maximum magnitudes (2.7× improvement). In the case of RMS values, this is a reduction from 1.2-2.4 μm to 0.2-0.25 μm (7.8x improvement). Noting that the x- and y-axes encounter maximum tracking errors of around 195 μm (x) and 352-408 μm (y) (considering rapid tool positioning movements), the proposed method is able to achieve tracking error prediction with 0.5-1.8% consistency, based on worst-case (i.e.,

48

maximum discrepancy). Full LS approach, on the other hand, achieves a consistency of 10-68%. It is noteworthy to mention that although the tracking errors in the individual axes are quite high, due to axis dynamics matching [73], the resulting contour errors are limited to only 10 μm.

Table 3.7. Tracking and contouring error prediction performance for two identification methods.

Discrepancy in Servo Error Prediction	Roughing Operation		Finishing Operation	
	Proposed Method	Full LS	Proposed Method	Full LS
X axis tracking error: RMS (MAX) [μm]	0.36 (2.63)	4.92 (32.05)	0.25 (3.43)	2.87 (31.98)
Y axis tracking error: RMS (MAX) [μm]	0.20 (1.81)	34.54 (241.87)	0.15 (1.88)	22.47 (280.32)
Contouring error: RMS (MAX) [μm]	0.25 (2.11)	2.36 (5.40)	0.20 (2.00)	1.17 (5.69)

3.7.2. 5-axis Milling Machine Tool Application

The Deckel Maho 80P hi-dyn five-axis machining center in Fig. 3.2 was also used as a test bed to validate the proposed identification method. The machining center has a Heidenhain TNC 430N controller with a built in scope function, which allows 4096 data samples to be logged at a sampling period of 0.6 ms. The scope function was used to capture the position commands, as well as measured position data from the linear encoder with 0.1 μm resolution. The bounds for the pole search are given in Table 3.8.

Table 3.8. Pole search bounds for x-y axes of Deckel Maho 80P.

Parameters	Min	Max
p [Hz]	1	833
ω_n [Hz]	1	210
ζ []	0.2	2

In Table 3.8, 833 Hz is the Nyquist frequency. 210 Hz is one quarter of the Nyquist frequency. Generally, complex conjugate poles are obtained within this bound. In order to obtain three real poles, upper bound of ζ_1 is set to be as 2. For damping ratios greater 1, the real pole is at $-\omega_n\left(\zeta + \sqrt{\zeta^2 - 1}\right) = -3.73\omega_n$ and by selecting quarter of the natural frequency, the real pole remains below the Nyquist frequency.

Estimation of the parameters was based off data collected during the execution of a diamond shaped toolpath with 20 mm edge length, interpolated with 96 mm/s feedrate (i.e., tangential velocity) and 3623 mm/s^2 and 3.33×10^6 mm/s^3 tangential acceleration and jerk. Validation in terms of tracking and contour error prediction was carried out considering this trajectory, and also a circular trajectory with 10 mm diameter, 100 mm/s feedrate, 5000 mm/s^2 tangential acceleration, and 4.4×10^6 mm/s^3 tangential jerk. The range of the trajectory response where the machine is in motion, and a few seconds after motion stops to capture the settling response (for estimating pole locations), was used as the training data. The estimated parameters are shown in Table 3.9. It can be seen that the x- and y-axes have somewhat close natural frequency (16 and 11 Hz) and damping ratio (1.12, 1.22). The higher frequency real poles at 89 Hz (x) and 210 Hz (y) have very little influence on the overall response. Also, the absence of pole-zero cancellation indicates that feedforward control is not used. Inspecting the TNC 430N parameters, it was verified that the built-in feedforward option had been disabled. During LS projection based estimation of the model parameters, some pole location candidates led to a negative value for d_0. Naturally, such models were excluded from candidacy.

Table 3.9. Identified parameters for x- and y- axes of Deckel Maho 80P via the proposed method.

Parameters	X Axis		Y Axis	
p [Hz]		88.55		209.74
ω_n [Hz]		15.79		11.18
ζ []		1.12		1.22
c_0		0.01		1.04
c_1		1.21E+03		2.34E+03
c_2		6.89E+04		8.19E+04
d_0		699.04		714.99
Tracking TF Zeros	**Freq. [Hz]**	**Damp. [ ]**	**Freq. [Hz]**	**Damp. [ ]**
z_1	48.8	-0.8	3326.3	1.0
z_2	48.8	-0.8	33.3	-1.0
z_3	9.3	1.0	5.8	1.0

The predictions obtained by the proposed approach have been benchmarked with those obtained through full LS. The actual and predicted motion data and tracking errors for the diamond and circular trajectories are presented in Fig. 3.17 and Fig. 3.18. Contour error prediction results are shown in Fig. 3.19. Prediction summaries for the proposed and full LS methods are presented in Table 3.10.

Considering Fig. 3.17 and Table 3.10, the discrepancy in tracking error prediction has been reduced in x- and y-axes from 10.3 and 12.7 μm to 6.5 and 9.1 μm, respectively, based on maximum values. While

30% improvement may appear modest, examining the tracking error prediction discrepancy graphs in the bottom left and right panels of Fig. 3.17 reveals that the major components of prediction inaccuracy originates during the friction transitions. Improvement of prediction during the friction transients has been addressed later in Chapter 4 and Chapter 5.
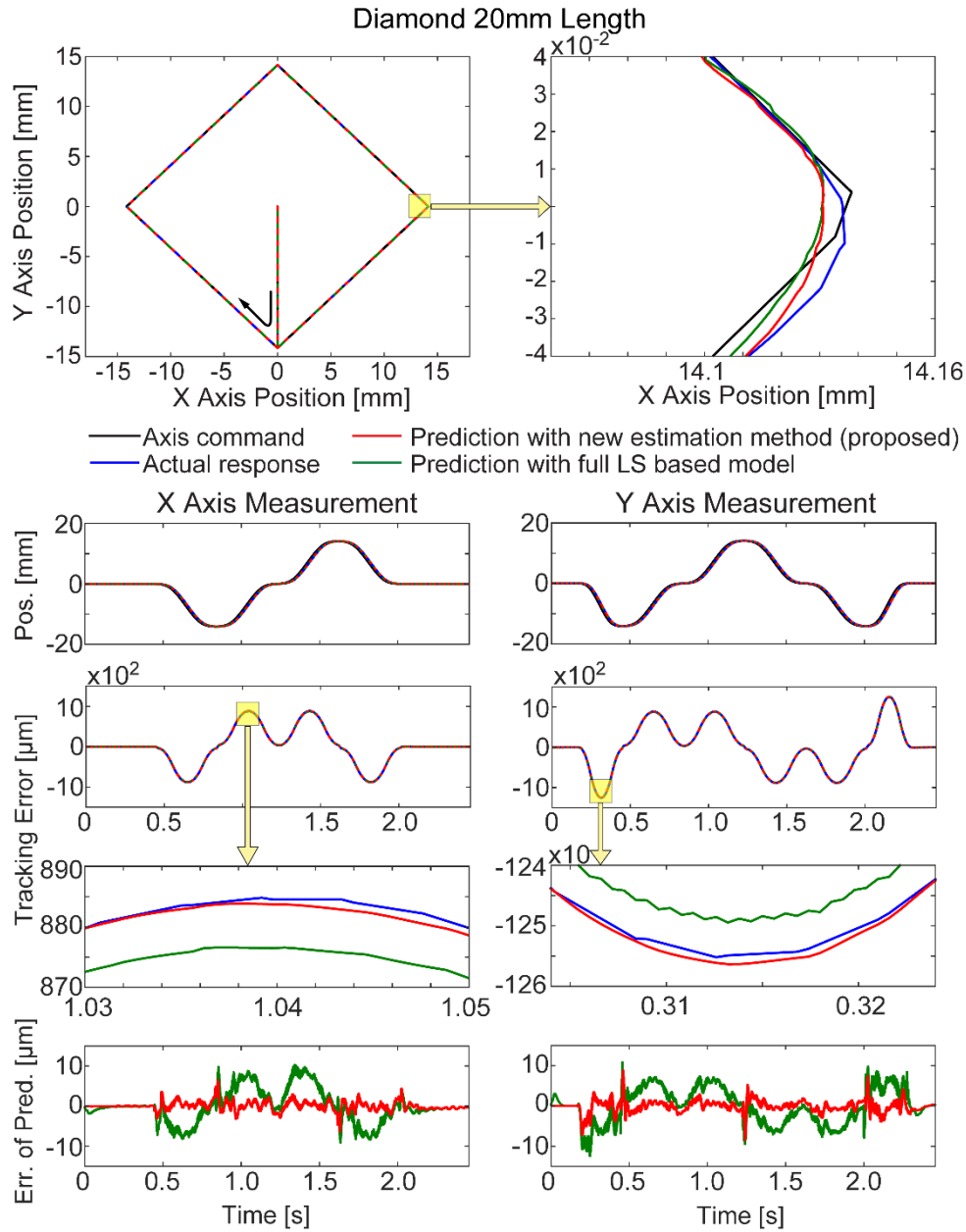
Fig. 3.17. Actual and predicted servo performance for diamond toolpath on machining center.

51

Considering the RMS values of prediction error, there is reduction from 4.1 and 4.4 µm to 1.2 and 1.6 µm (i.e., 60-70% improvement) in x- and y-axes, respectively. This is also seen in the bottom panels of Fig. 3.17 by the fact that the proposed method is able to achieve much more uniform improvement in the prediction of tracking error, facilitated by more accurate approximation of the system's linear dynamics.

Similar trends are seen in the prediction results for the circular toolpath in Fig. 3.18 and Table 3.10. Considering maximum values, the prediction discrepancy is reduced in x- and y-axes from 17.0 and 14.6 µm to 8.5 and 10.7 µm, in the mentioned order. In the case of the circular trajectory, the dynamic response due to sinusoidal command inputs in x- and y-axes has as much, and perhaps a bit more, influence on the largest discrepancy in tracking error prediction compared to friction.

Thus, improvement of the model parameter estimation achieves recognizable refinement in predicting the true tracking error. RMS values for tracking error prediction discrepancy are reduced from 6.5 µm to 1.6 and 1.7 µm in x- and y- axes, which is again 70% improvement. This result corroborates the reduction in tracking error prediction discrepancy graphs, seen at the bottom left and right panels of Fig. 3.18.

Prediction of contouring errors for diamond and circular toolpaths, and their discrepancy profiles, are shown in Fig. 3.19. Considering Fig. 3.19 and Table 3.10, for the diamond toolpath the maximum contouring error prediction discrepancy is slightly worse with the proposed method, increasing from 6.6 to 6.9 µm of discrepancy. This is in spite of the improvements in predicting the servo errors. As mentioned earlier for the diamond toolpath, the maximum discrepancy is very much dominated by the friction model. The RMS value, on the other hand, is improved from 1.1 to only 0.9 µm, which is virtually indistinguishable. This is because starting out, due to matched x-y dynamics, the contour error is very small to begin with in tracking straight line (linear) toolpaths. In the case of the circular toolpath, the improvement is clearer, around 30%. The maximum discrepancy in contouring error prediction is reduced from 11.2 to 7.9 µm, and its RMS value reduced from 2.1 to 1.4 µm.
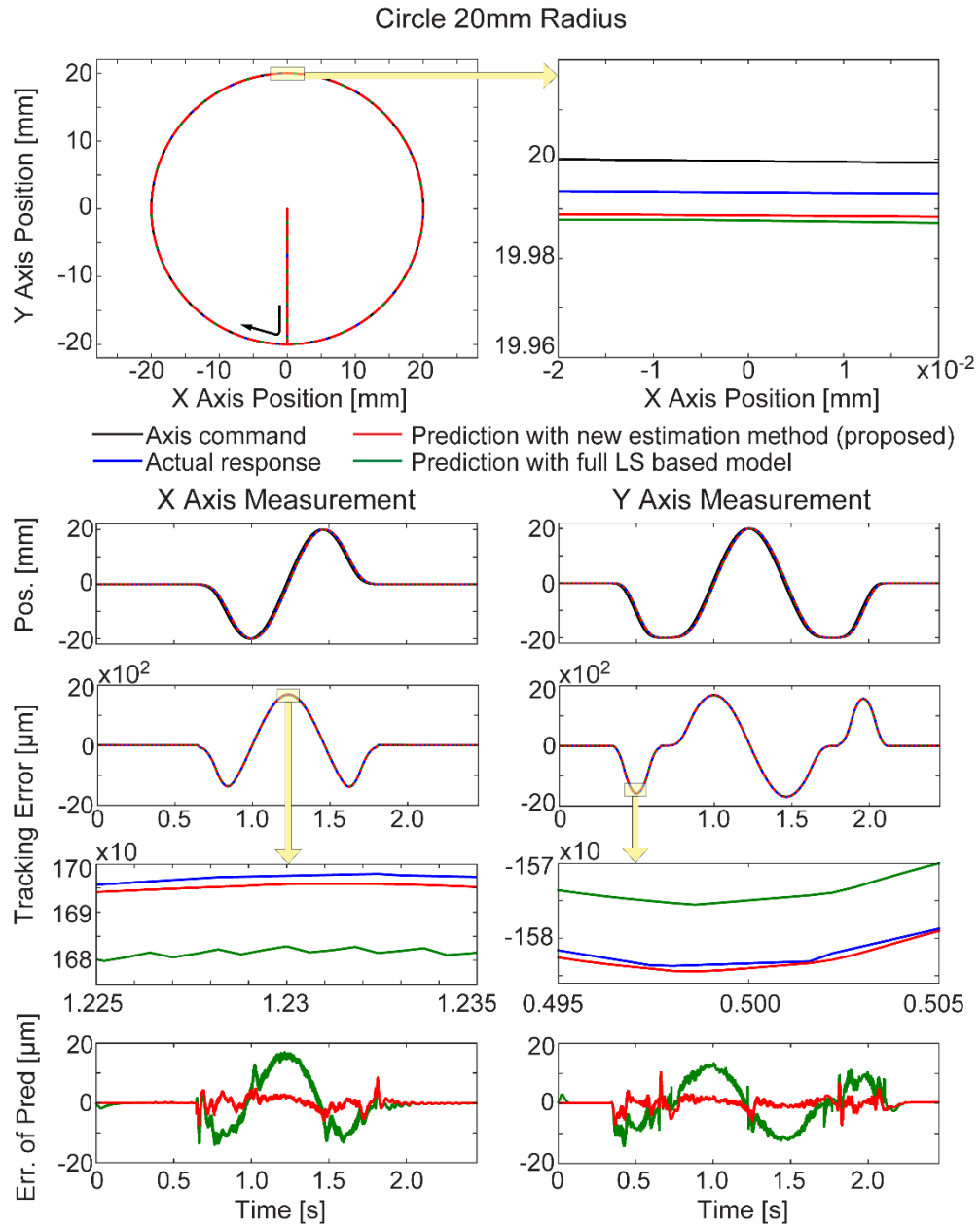
Fig. 3.18. Actual and predicted servo performance for circular toolpath on machining center.

As indicated earlier, improvement in contouring error prediction is significantly more challenging than improving the tracking error prediction, especially in orthogonal feed drive systems with well-matched dynamics. The instantaneous tool position has a natural tendency to fall on top of the desired toolpath during linear and low curvature paths. Hence, improvement in contour error prediction may not be as noticeable as the improvement in the tracking error predictions. However, in trajectories involving high curvature toolpaths, as well as large jerk, acceleration, and velocity magnitudes, enhancing the accuracy

of tracking error prediction is still key to achieving good process prediction and quality control capability.
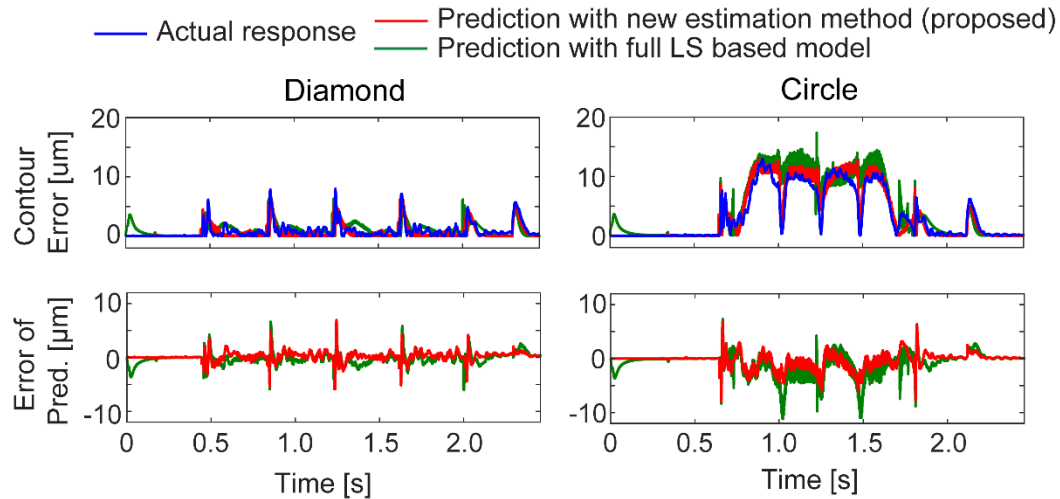
Fig. 3.19. Contour errors for diamond and circle toolpaths on Deckel Maho 80P.

Table 3.10. Tracking and contouring error prediction performance for two identification methods.

Discrepancy in Servo Error Prediction	Diamond Toolpath		Circular Toolpath	
	Proposed Method	Full LS	Proposed Method	Full LS
X axis tracking error: RMS (MAX) [μm]	1.16 (6.45)	4.07 (10.29)	1.56 (8.45)	6.30 (16.97)
Y axis tracking error: RMS (MAX) [μm]	1.59 (9.09)	4.36 (12.65)	1.73 (10.68)	6.47 (14.62)
Contouring error: RMS (MAX) [μm]	0.90 (6.93)	1.16 (6.61)	1.39 (7.94)	2.14 (11.19)

Considering the magnitudes of tracking errors observed in Fig. 3.17 and Fig. 3.18, the actual servo errors can be predicted within 0.7% closeness via the proposed method. This method also enables the contouring error to be predicted with 10-11% closeness in RMS. However, there is still room for improvement, as the maximum discrepancy in contour error prediction at motion reversals appears to reach as high as 60-86%. This is addressed further in the proceeding chapters by refining the friction model.

3.8. Conclusion

A new method for identifying virtual feed drive models with in-process collected CNC data has been presented. As verified in simulations and experiments, the convergence and prediction accuracy have

been significantly improved over an earlier proposed solution. This proposed method shows a great potential to identify feed drive dynamics without interrupting machine's production. The new method's convergence results did not deviate significantly under measurement noise while classical LS greatly suffered in terms of convergence. In addition, the performance analysis of both methods have been carried out based on experimental data collected from two different machine tools. As this approach offers great advantage in terms of collecting in-process data and constructing feed drive dynamics, this technique still has a few drawbacks: once the friction becomes dominant, especially during pre-sliding regime, the prediction results may degrade due to Coulomb friction model's lack of ability to reflect friction dynamics. Hence, as done in next chapters, more advanced friction models can be used jointly with this method to improve the feed drive dynamics. Furthermore, while better convergence (to correct parameters) and robustness (in the presence of measurement noise) is achieved, the persistence of excitation for the input trajectory is still very important and critical to obtain even better estimation results. Lastly, virtual feed drive dynamics has been constructed considering rigid body dynamics and this new approach still lacks for modeling vibratory dynamics.

Chapter 4

Reduced Parameter GMS Friction Model

4.1.   Introduction

In the emulation of the dynamics of feed drives for multi-axis machines, high fidelity realization of the nonlinear stick-slip friction dynamics plays an important role. While elaborate friction models have been proposed, such as the GMS model, their unknown parameters can be numerous and difficult to identify from limited field data. This thesis proposes a new and highly efficient method for parametrizing the pre-sliding portion of the GMS model, via the characterization of the so-called 'virgin curve' with only three parameters: the overall breakaway displacement, the breakaway force, and a shape factor. It is shown that such an approximation can successfully replicate earlier GMS pre-sliding data reported in literature. Having a reduced parameter formulation for the GMS friction model can also benefit applications such as a virtual CNC [10]. The concept of virtual CNC enable the prediction and optimization of the multi-axis response of machine tools to various command trajectories. For a virtual CNC implementation, where a feed drive dynamics typically needs to be identified from limited field data [70][73], as done in Chapter 3, high number of elements increase the number of unknowns to search through.

In this chapter, a new method to approximate the virgin curve is presented, as shown in Fig. 4.1. The virgin curve is defined as the initial portion of the hysteresis curve in the pre-sliding regime for the GMS friction model. Approximation of the virgin curve automatically leads to determining the pre-sliding hysteresis curve that is the doubled version of the virgin curve [46]. With the proposed method, instead of using $2N$ parameters to constitute the virgin curve via elemental stiffness (k_i) and force contribution factors (α_i) as done in the typical model formulation [43], a similar effect is captured by the use of only three parameters. Following the approximation of the virgin curve with an analytical function, a multi-spring GMS pre-sliding model can be extracted as shown in Fig. 4.1, which can be used in proceeding time-domain simulations. The proposed approximation technique significantly simplifies the parameterization of a GMS model while still preserving the main strengths of the GMS approach.

$$K_{c1} = k_1 + k_2 + k_3 + k_4 + \cdots + k_i$$
$$K_{c2} = k_2 + k_3 + k_4 + \cdots + k_i$$
$$K_{c3} = k_3 + k_4 + \cdots + k_i$$
$$K_{c4} = k_4 + \cdots + k_i$$
$$K_{ci} = k_i$$

$$s(v) = W_1 + W_2 + W_3 + W_4 + \cdots + W_i$$

$$\sum \alpha_i = 1$$
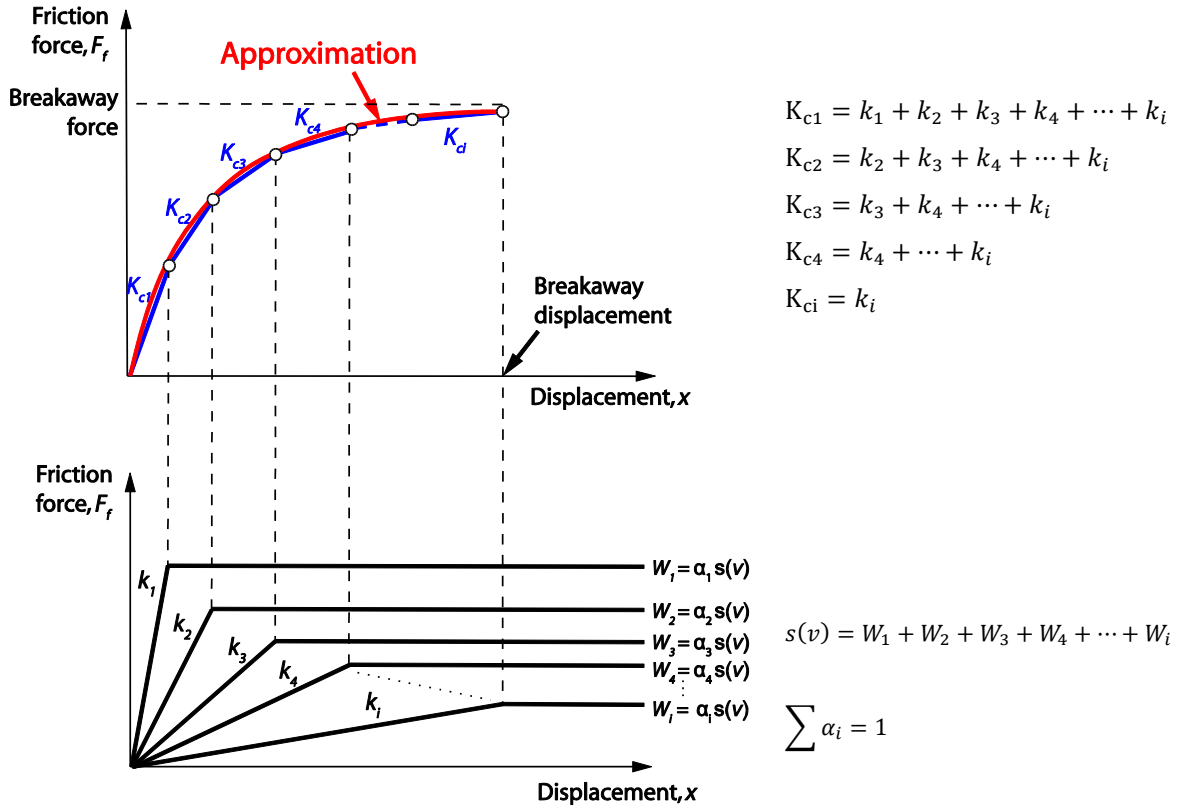
Fig. 4.1. Approximation of 2N parameters.

The identification of a full GMS model requires $2N$ parameters. While estimating these parameters (stiffness values k_i, and force contribution factors α_i) can be done manually in a systematic manner, there are some disadvantages to this procedure.

i) The data capture frequency has to be very high to be able to accurately characterize the pre-sliding motion.

ii) Special heuristics are required to isolate only the virgin curve portion of the force versus displacement graph, from in-process data.

iii) Putting 8 or 10 unknown variables ($N = 4, 5$) into a global search routine was implemented by the author two years ago and was seen to demonstrate very poor convergence, unless an accurate initial guess can be used, which again requires elaborate and robust heuristics (reason ii).

On the other hand, the proposed three parameter approximation has the following advantages:

i) It is relatively easier to spot break away displacement and breakaway force in operational data. Even if these numbers are not exactly determined, these can be extracted with simpler heuristics and used as good initial guesses.

ii) High-resolution pre-sliding data is not required, as the shape of the pre-sliding regime is determined just by one factor. By modulating the shape factor and the breakaway force and breakaway displacement, and observing the replication of the predicted axis output, the reduced parameter GMS provides a formulation which is much easier and more robust to implement using existing global optimization algorithms.

The remainder of this chapter is organized as follows. GMS friction model is briefly explained in Section 4.2. In Section 4.3, the proposed parameterization method is explained. Section 4.4 and Section 4.5 provide estimation results based on experimental data and comparison with other friction models (LuGre and fully parameterized GMS friction models). Section 4.6 presents the conclusion.

4.2. GMS Friction Model Brief Introduction

As mentioned in Chapter 2, there are N elementary spring block units and the forces of these elements are added together to obtain the equivalent friction force. For each element in the GMS model, two phases of friction are considered, pre-sliding and sliding regimes, as seen in Fig. 4.2. When a certain unit is sticking (in the pre-sliding regime), the state equation of this unit is

$$\frac{dF_i}{dt} = k_i v \tag{4.1}$$

where F_i is the elementary friction force, v is the velocity and, k_i is the elementary stiffness. Pre-sliding or sticking continues until the friction force (F_i) reaches the maximum value $W_i = \alpha_i s(v)$, where $s(v)$ is the Stribeck friction and α_i is the normalized sustainable maximum friction force (or sometimes referred as 'saturation limit'). In this thesis, α_i will be referred as 'contribution factor' for each elementary block i since this parameter designates the contribution of F_i to the total friction force F_f. When the system starts sliding, the sum of contribution factors equal to 1 (i.e. the total friction force equals the Stribeck curve). For the sliding regime, the state equation is given by

$$\frac{dF_i}{dt} = sgn(v)C\left(\alpha_i - \frac{F_i}{s(v)}\right), \tag{4.2}$$

where C is the attraction parameter which represents the rate at which the friction force follows the Stribeck effect in sliding. The total friction force is obtained by adding the force outputs of all elementary state model and including an overall viscous friction term (σ):

$$F_f(v) = \sum_{i=1}^{N} F_i(v) + \sigma v(t) \tag{4.3}$$
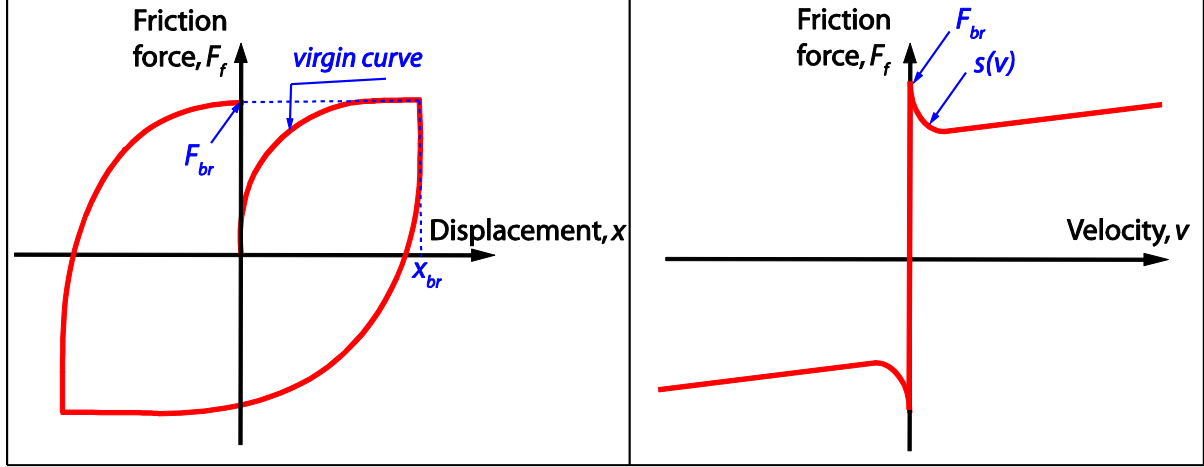
Fig. 4.2. Representation of pre-sliding (left) and sliding (right) regimes.

4.3.   Spline Approximation of the GMS Pre-Sliding Characteristic

In the proposed approach, the GMS pre-sliding regime is defined via only three parameters, namely the breakaway (static) friction force (F_{br}) and breakaway displacement (x_{br}) values as shown in Fig. 4.1 and a shape factor (n), as illustrated in Fig. 4.3b. To enable virgin curve shape definition, irrespective of the breakaway force and displacement magnitudes, normalization is performed as shown in Fig. 4.3a and Fig. 4.3b. The normalized friction force and displacement are defined as: $\bar{F}_f = F_f/F_{br}$ and $\bar{x} = x/x_{br}$. The parametric approximation for these quantities is represented with the functions $\bar{f}(u)$ and $\bar{x}(u)$, where u, as explained in the proceeding, is the function parameter. Consequently, $\bar{x}_u$ and $\bar{f}_u$ are the first derivatives of $\bar{x}$ and $\bar{f}$ with respect to u.

Aiming to find a simple yet effective approximation for the GMS virgin curve data presented in literature, such as in [44] and [96], several analytical function were iteratively tried, including parabolas, circle/arc equations, ellipse equations, and polynomials of various order. From these studies, it was determined that a 4th order spline structure, as shown in Eq. (4.4), can be appropriate. Other curves such as B-splines can provide higher flexibility, but require more unknowns to solve, bringing the situation close to the original multi-segment GMS formulation. The principal advantage of the 4th order polynomial, together with the parameterization proposed in Eq. (4.8), is that it allows for the complete curve to be solved by the specification of a single variable, the shape factor (n).
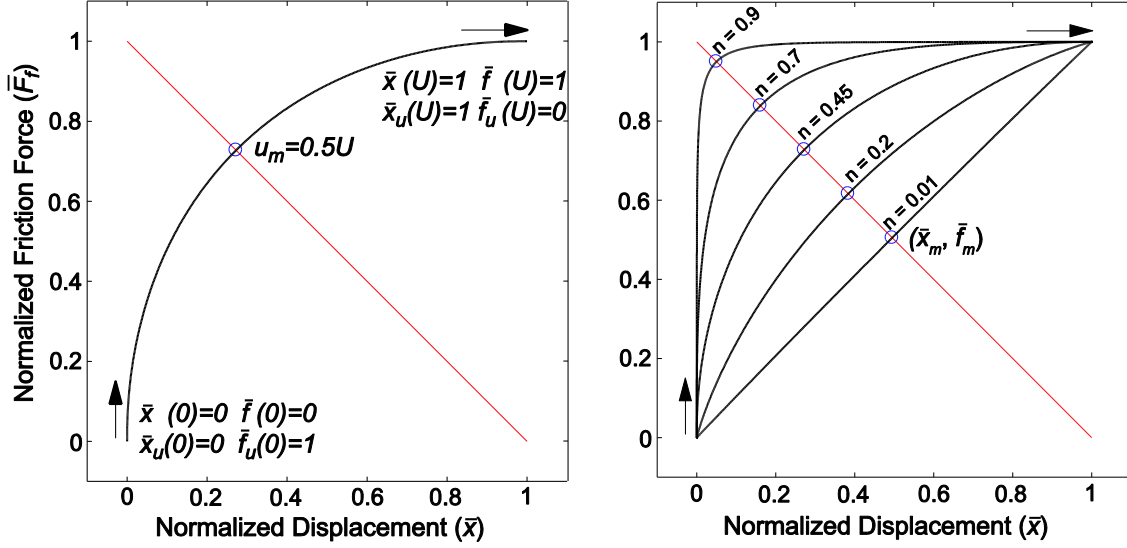
a- Virgin curve spline with initial and final
boundary conditions.

b- Virgin curve splines for different shape
factor (n) values.

Fig. 4.3. Virgin curve spline construction.

$$\bar{x}(u) = A_x u^4 + B_x u^3 + C_x u^2 + D_x u + E_x$$
$$\bar{f}(u) = A_f u^4 + B_f u^3 + C_f u^2 + D_f u + E_f \qquad 0 \leq u \leq U \qquad (4.4)$$

Above, $A_{x/f}$, $B_{x/f}$, $C_{x/f}$, $D_{x/f}$, and $E_{x/f}$ are the polynomial coefficients, which are fixed for given shape factor (n) (i.e. these coefficients are uniquely determined by n). u is the spline parameter and U is the spline parameter upper bound. It is important to mention that to get 'suitable' virgin curve shapes, as will be demonstrated in the proceeding, U needs to be selected based on the chosen shape factor n.

The midpoint of the spline is obtained via the following equations:

$$\bar{x}_m = \bar{x}(u_m) = A_x u_m^4 + B_x u_m^3 + C_x u_m^2 + D_x u_m + E_x$$
$$\bar{f}_m = \bar{f}(u_m) = A_f u_m^4 + B_f u_m^3 + C_f u_m^2 + D_f u_m + E_f \qquad , \text{where} \qquad u_m = 0.5U \qquad (4.5)$$

The proposed idea is to alter the geometry of the virgin curve approximation by shifting the coordinates of its midpoint $(\bar{x}_m, \bar{f}_m)$ as a function of the chosen shape factor n, as shown in Fig. 4.3b. When $n \to 0$, $(\bar{x}_m, \bar{f}_m) \to (0.5, 0.5)$. When $n \to 1$, $(\bar{x}_m, \bar{f}_m) \to (0,1)$. The following linear relationships are used for this purpose, which generate the $(\bar{x}_m, \bar{f}_m)$ point along the red diagonal line shown in the figure:

$$\bar{x}_m = 0.5 - 0.5n = 0.5(1 - n), \quad \bar{f}_m = 0.5 + 0.5n = 0.5(1 + n) \qquad (4.6)$$

60

Combining this with the initial and final boundary conditions illustrated in Fig. 4.3b, which shape the start and end values and slopes, and applying Eqs. (4.4) and (4.5) leads to:
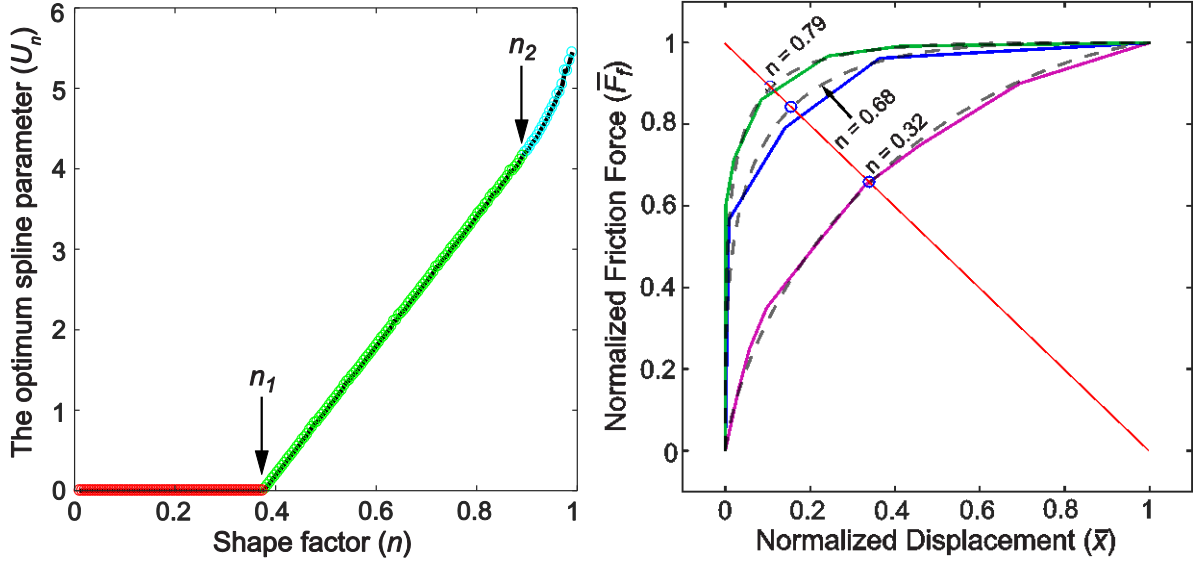
a- Shape factor (n) vs. the optimal spline parameter (U_n) to yield 'realistic' virgin curve shapes.

b- Proposed virgin splines (black-dashed) vs. virgin curves taken from different sources (Yoon et. al. [44] (magenta), Jamaluddin et. al. [96] (blue) and a ball-screw drive at UW/PCL (green))

Fig. 4.4. Virgin curve approximation.

$$
\begin{bmatrix} \bar{x}(0) \\ \bar{x}_u(0) \\ \bar{x}(U) \\ \bar{x}_u(U) \\ \bar{x}(u_m) \end{bmatrix} = \begin{bmatrix} 0 \\ 0 \\ 1 \\ 1 \\ \bar{x}_m \end{bmatrix} \rightarrow \underbrace{\begin{bmatrix} 0 & 0 & 0 & 0 & 1 \\ 0 & 0 & 0 & 1 & 0 \\ U^4 & U^3 & U^2 & U & 1 \\ 4U^3 & 3U^2 & 2U & 1 & 0 \\ u_m^4 & u_m^3 & u_m^2 & u_m & 1 \end{bmatrix}}_{L_x} \underbrace{\begin{bmatrix} A_x \\ B_x \\ C_x \\ D_x \\ E_x \end{bmatrix}}_{\theta_x} = \underbrace{\begin{bmatrix} 0 \\ 0 \\ 1 \\ 1 \\ \bar{x}_m \end{bmatrix}}_{\xi_x}
$$

$$
\begin{bmatrix} \bar{f}(0) \\ \bar{f}_u(0) \\ \bar{f}(U) \\ \bar{f}_u(U) \\ \bar{f}(u_m) \end{bmatrix} = \begin{bmatrix} 0 \\ 1 \\ 1 \\ 0 \\ \bar{f}_m \end{bmatrix} \rightarrow \underbrace{\begin{bmatrix} 0 & 0 & 0 & 0 & 1 \\ 0 & 0 & 0 & 1 & 0 \\ U^4 & U^3 & U^2 & U & 1 \\ 4U^3 & 3U^2 & 2U & 1 & 0 \\ u_m^4 & u_m^3 & u_m^2 & u_m & 1 \end{bmatrix}}_{L_f} \underbrace{\begin{bmatrix} A_f \\ B_f \\ C_f \\ D_f \\ E_f \end{bmatrix}}_{\theta_f} = \underbrace{\begin{bmatrix} 0 \\ 1 \\ 1 \\ 0 \\ \bar{f}_m \end{bmatrix}}_{\xi_f}
$$

(4.7)

A key parameter which defines the spline shape is the parameter range U. Inadequate choice of this value can result in the spline shape to display fluctuations, an inflection (i.e. loop), or a bulge outside the acceptable envelope of normalized displacement and force values. Therefore, it was found that for different values of the shape factor n, a suitable value of U needs to be pre-assigned.

This assignment is made by searching for the 'optimal' spline parameter range value U_n via the following algorithm:

i)   Scan possible values of the shape factor n (0.01 … 0.99, for example, in 200 steps).

ii) For each n, try different parameter range values U (10^{-3} … 10^1, typically in 5000 steps of logarithmic distribution).

iii) Evaluate the resulting 'virgin curve' approximation for each case using Eq. (4.7). This step essentially evaluates $A_x, \ldots, E_x$, and $A_f, \ldots, E_f$.

iv) Compute the virgin curve approximation $(\bar{x}(u), \bar{f}(u))$ via Eq. (4.4) for $0 \le u \le 1$.

v)   Choose the smallest value of U for the tested shape factor n, such that the proposed curve $(\bar{x}(u), \bar{f}(u))$ *always satisfies* the conditions: $0 \le \bar{x} \le 1$ and $0 \le \bar{f} \le 1$.

It was seen that choosing the minimum parameter range U helps avoid fluctuations or inflection (looping). However, keeping U too small, especially for $n \ge 0.38$, was observed to cause the curve the bulge out of the bounds of $0 \le \bar{x} \le 1$ and $0 \le \bar{f} \le 1$. Using the above algorithm, the 'optimum' spline parameter range (U_n) determined for each possible shape factor (n) is shown in Fig. 4.4a, with black dots. In this data, two break points are observed: $n_1 = 0.3757$ and $n_2 = 0.8994$. U_n stays constant for $n < n_1$ (below the first breakpoint), then increases linearly with increasing shape factor. For $n > n_2$ (beyond the second breakpoint), U_n displays quadratic growth. The general variation of U_n has been captured with the following fitted expressions:

$$U_n(n) = \begin{cases} 0.001 \, , \, for \, 0 \le n < n_1 \\ -3.016728 + 8.031550n \, , n_1 \le n \le n_2 \\ 53.059150 - 115.486220n + 68.048632n^2 \, , n_2 < n \le 1 \end{cases} \tag{4.8}$$

Evaluation of the expressions in Eq. (4.8) has been overlaid in color (red / green / cyan) in Fig. 4.4a on top of the individually computed optimal U_n values (black dots), thus verifying a close and successful approximation. The calculation of U_n via Eq. (4.8) can be regarded as an essential ingredient which enables the proposed spline expression in Eq. (4.4) to yield the desirable virgin curve shapes shown in Fig. 4.3b.

While researching the most suitable way to parametrize U with respect to n, the minimization of various objective functions was also considered and evaluated, such as the integral square of the second or third derivatives of the profiles $\bar{x}$ and $\bar{f}$ with respect to u, as well as the integral square of ds/du. In the latter, $ds = \sqrt{(d\bar{x})^2 + (d\bar{f})^2} \cdot du$ corresponds to increment in the arc length of the normalized virgin curve, as a function of the increment in the spline parameter du. Compared to these other approaches, the methodology which led to Eq. (4.8) yielded the most successful result.

Hence, in computing a normalized virgin curve for a shape factor n, the following procedure is followed:

    i)   The corresponding spline parameter range $U = U_n(n)$ is determined via Eq. (4.8).

    ii) $A_x, \dots, E_x$, and $A_f, \dots, E_f$ coefficients are solved via Eq. (4.7).

    iii)   Points on the virgin curve are evaluated as $(\bar{x}(u), \bar{f}(u))$ via Eq. (4.4) for $0 \le u \le 1$.

In Fig. 4.4b, virgin curves from different experimental sources are compared with the proposed parameterization approach. In all data sets, F_{br} and x_{br} could be easily observed visually. Thus, the virgin curves have been normalized with respect to these factors. Two of the normalized virgin curves in Fig. 4.4b are based on parameters taken from [44] and [96]. The last (green colored virgin curve) is based on an in-house built ball-screw drive experimental setup, shown in Fig. 4.5. As can be seen, in all cases, the geometry of the normalized virgin curve can be closely captured with the proposed spline approximation, by determining a suitable shape factor n. After finding the shape factor and de-normalizing the virgin curve (i.e., multiplying the vertical and horizontal data with F_{br} and x_{br}, respectively), the numerical data generated from the analytical curve can be used to construct a multi-spring GMS pre-sliding model as illustrated in Fig. 4.1. Hence, the reduced parameter format (F_{br}, x_{br}, n) helps quickly and efficiently parameterize and identify the pre-sliding model. The multi-state simulation of friction then utilizes the resulting computed slip element stiffness values (k_i) and force contribution coefficients (α_i), per [43][44]. Naturally, this approximation also does have some limitations, and may not always succeed in exactly capturing all possible virgin curve shapes. Nevertheless, it provides a highly efficient and intuitive definition of the pre-sliding response, and promisingly so far it has been successful for the reported and tested data sets.

4.4.   Friction Parameter Identification Based on Experimental Data from Ball-Screw Drive

In this section, after introducing the experimental setup used for data collection, parameter identification results using the setup are presented.

4.4.1. Experimental Setup

To validate the proposed approximation, a single-axis ball-screw drive setup was used (Fig. 4.5). The ball-screw is THK-BNK-2020 driven with a 3 kW Omron servo motor, which has 3000 r/min rated speed and 20-bit incremental encoder. The ball-screw drive has 0.02 m diameter and 0.02 m lead. The ball-screw has oversized ball and preload torque is rated between 2×10^{-2}–9.8×10^{-2} Nm. In the setup, the table position is directly measured with a linear encoder at a resolution of 10 nm (by interpolating 4 μm period sinusoidal signals). The guideway system consists of four 3" diameter porous carbon air bushings. Hence, the main contributors to the observed friction originate from the ball-screw/preloaded nut interface, the rotational bearings located inside the motor, and those supporting the ball-screw.
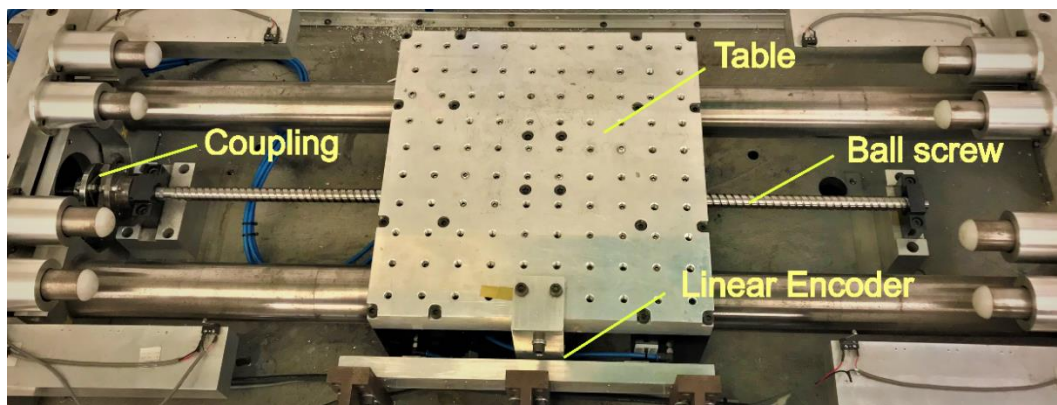
Fig. 4.5. Ball-screw drive.

Position measurements of the axis were gathered in open-loop using the scheme shown in Fig. 4.6. Inertia and viscous friction coefficients were identified using Least Squares (LS) technique, following the methodology in [18]. Total equivalent inertia (J) and viscous damping (B) values are identified as 7×10^{-3} and 1.1×10^{-3} kgm^2, respectively. The amplifier and motor torque constants are 2.3293 A/V and 0.41 Nm/A, respectively. Also, transmission gain (r_g) is 3.18 mm/rad.
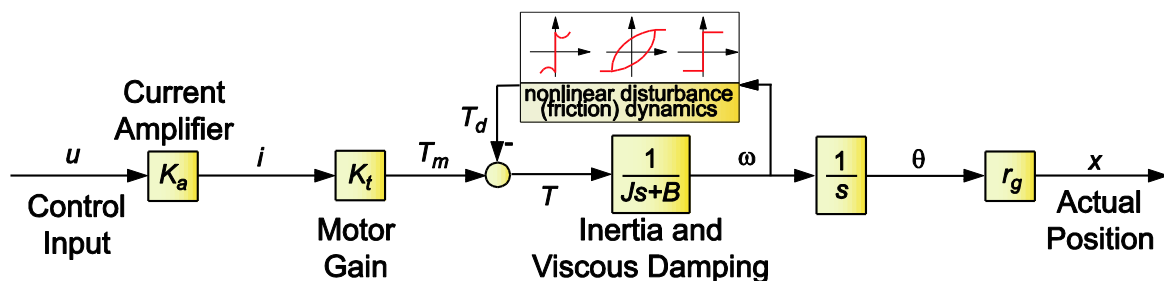
Fig. 4.6. Ball-screw drive open-loop scheme.

4.4.2. Identification Results

The hysteresis virgin curves obtained using the proposed GMS parameter identification methodology have been compared to those measured experimentally. To obtain pre-sliding data, the ball-screw was excited with small and slow-speed sinusoidal torque inputs (with amplitudes around 0.143 Nm and frequency 0.35 Hz). This torque amplitude is the threshold before significant sliding is observed. Various amplitudes of torque inputs are applied until the ball-screw drive reaches the gross limit of the pre-sliding regime. This enables the identification of three unknowns: the breakaway (static friction) force (F_{br}), the breakaway displacement (x_{br}), and shape factor (n).
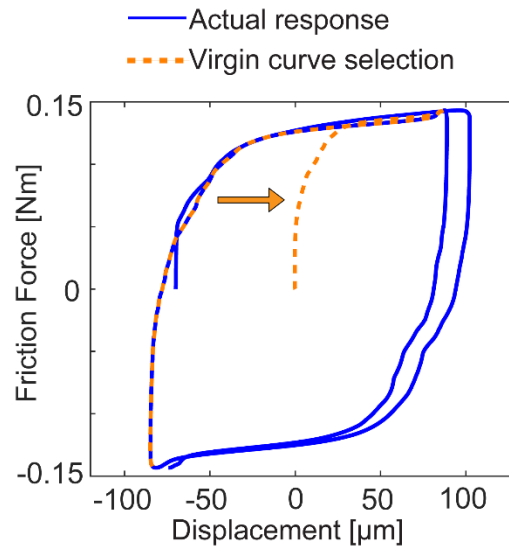
Fig. 4.7. Measured pre-sliding virgin curve construction.

A sample hysteresis curve is plotted as shown in Fig. 4.7. Following [46] and [52], the virgin curve can be determined by halving the left-hand branch of the full hysteresis curve (shown in the figure with the orange dashed line). In this work, this approach is used to visualize the virgin curve from experimental data, typically against the response prediction from the identified model.

In the experiments, displacement and torque command signals were collected via a dSpace system at a sampling frequency of 20 kHz. Displacement was measured using the linear encoder scale. A high sampling frequency was used to ensure clear and high-resolution data collection. Five seconds of data was gathered from the experimental setup for different excitation amplitudes. While applying the automated identification algorithm, 75% of the data was used. In numerically evaluating and visualizing the effectiveness of the estimated friction model, 100% of the data was used.
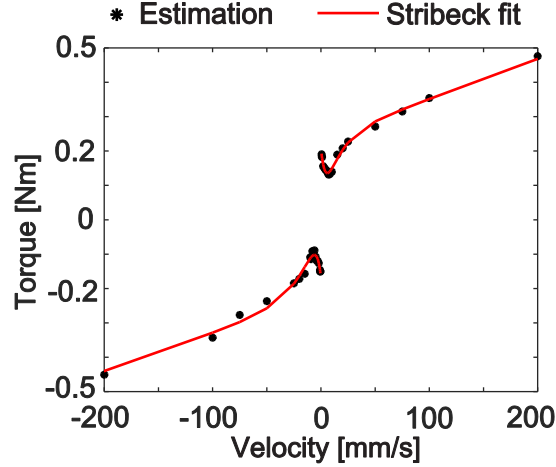
Fig. 4.8. Stribeck friction model fit.

Before focusing on the pre-sliding behaviour, the viscous friction and Stribeck friction properties were identified. Stribeck friction was modelled with the following equation:

$$s(v) = sgn(v)\left(F_s e^{-\frac{v}{v_{s1}}} + F_c\left(1 - e^{-\frac{v}{v_{s2}}}\right)\right),$$

(4.9)

where F_s and F_c are the static and Coulomb friction forces. v_{s1} and v_{s2} are the velocity constants that shape the spacing between the pre-sliding and sliding regions. Identification of these was accomplished by operating the feed drive in closed-loop position control, and taking the average of the motor torque readings during different steady state velocities, similar to [18]. The fitted sliding friction model, superposed on top of experimental readings, is shown in Fig. 4.8. The model parameters, estimated via Matlab's nonlinear least square solver are: the static friction (F_s) is 0.21 Nm and the Coulomb friction is 0.18 Nm. Velocity constants are $v_{s1} = 1.26$ mm/s and $v_{s2} = 4.39$ mm/s.

As shown in Fig. 4.4b (ball-screw drive virgin curve approximation), the pre-sliding portion of the GMS model can be fitted by observing the breakaway force and breakaway displacement from experimental data, and adjusting the shape factor manually. A key advantage of the reduced parameter GMS model is its ease of identifying the pre-sliding response with a lower number of unknown variables, which leads to a more efficient identification problem. To estimate the reduced parameter GMS model in an automated manner, which can later be extended to also concurrently identify other dynamics (such as various electro-mechanical transfer functions which interact with the friction), implementation has been realized using Matlab's global optimization toolbox [97]. Different

algorithms, such as global search, multi-start search, particle swarm, and genetic algorithms, can be used. Here, the presented results are based on the global search method [97].

Suitable lower and upper bounds are considered for the free variables (F_{br}, x_{br}, n). Bounds for breakaway force and breakaway displacement can be determined by inspecting the data, and also from experience. Bounds for shape factor are set as $0.01 - 0.99$. For each candidate parameter set, the response of the feed drive model shown in Fig. 4.6, combined with the GMS friction model (containing both pre-sliding and sliding (i.e., Stribeck) behaviors) is simulated for the same torque input applied to the actual experimental setup. In the simulations, the number of Maxwell slip elements has been chosen as 10. Since this has no impact on the number of search parameters, higher quality simulation can easily be accomplished by interpolating a larger number of spring elements as needed from the analytical approximation of the virgin curve developed in the previous section. For each element to be able to transition seamlessly between pre-sliding and sliding regimes, based on the tested breakaway force value, the Stribeck model was also scaled so that the static friction value (F_s) coincided with the breakaway force (F_{br}), and the Coulomb friction value (F_c) was also modulated proportionally.

The objective function to be minimized penalizes the root mean square of the prediction error between the simulated displacement profile ($\hat{x}_k$) and the experimentally measured displacement (x_k) as defined below:

$$q = \sqrt{\frac{1}{N}\sum_{k=1}^{N}(x_k - \hat{x}_k)^2} , \qquad N: number\ of\ data\ samples \tag{4.10}$$

Automatic identification of the pre-sliding friction parameters was carried out with two different sets of data. In the first set, the input torque was set just below the typically observed breakaway threshold (0.143 Nm). Thus, the response was predominantly pre-sliding. In the second set, realized with 0.153 Nm excitation amplitude, the breakaway threshold is exceeded further, enabling a more evident mixture of pre-sliding and sliding regimes to be observed.

Test 1: Predominantly pre-sliding response

Table 4.1 shows the visually observed and automatically estimated friction pre-sliding parameters. The corresponding input torque and displacement data are presented in Fig. 4.9, both related to the experimental data and the identified model. As seen in Table 4.1, the automatically estimated breakaway torque (0.142 Nm) matches quite closely the visually measured value (0.143 Nm). The

breakaway displacement (85.5 µm) is estimated with around 8 µm (13%) difference as 74.8 µm. As seen in Fig. 4.9a, the shape of the experimentally measured virgin curve, constructed with the halving procedure in [52], is very close to the response generated by the automatically fit model.

Table 4.1. Three parameter search results.

	Estimated manually (by inspection of the data)	Estimated Automatically (via global optimization)
Breakaway force (F_b) [Nm]	0.143	0.142
Breakaway displacement (x_b) [µm]	85.50	74.80
Shape factor (n)	-	0.56

a- Virgin curve approximation.   b- Hysteresis curve approximation.
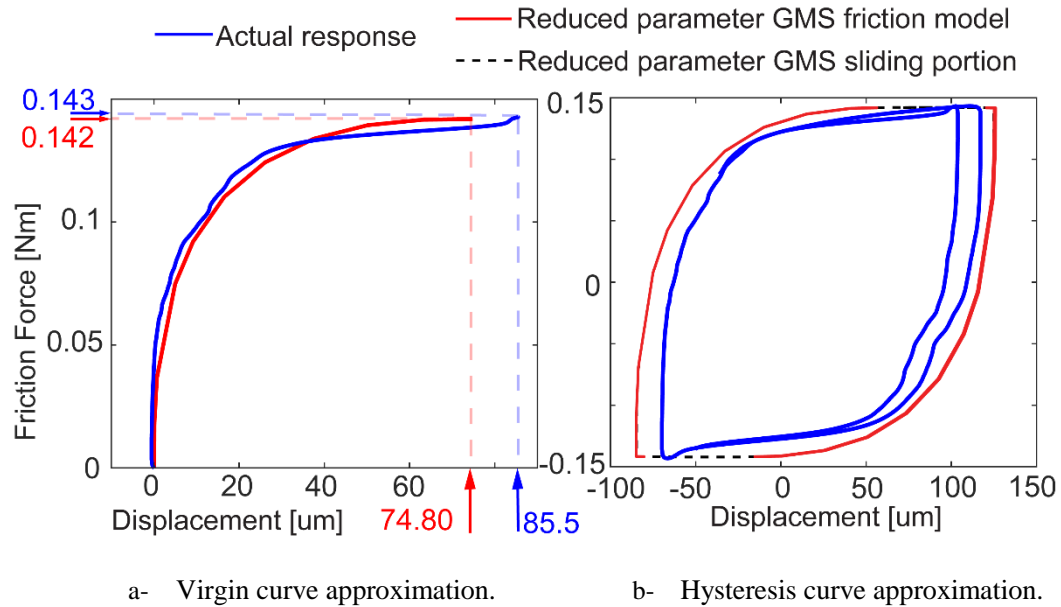
Fig. 4.9. Experimental pre-sliding identification results.

There is also good agreement when the hysteresis curve is constructed. Fig. 4.9b shows the doubled version of the virgin curve approximation. As can be seen, the overall shape of the hysteresis curve is matched reasonably well by the model. One difference is that while the experimental setup is mostly at pre-sliding regime and only a very small amount of sliding occurs (~10 µm), a larger amount of sliding is predicted by the model (60-70 µm, shown with the dashed black line in Fig. 4.9b). Since even very small difference in predicting the sliding behavior can lead to noticeable discrepancy due to double-integration from the acceleration to the position profiles, the presence of this mismatch at the moment is not a major concern. The main point demonstrated is that the proposed reduced parameter formulation for GMS can indeed be used in automatic model building. Naturally, due to mechanical imperfections,

the complex kinematics and contact mechanics in the ball-screw and preloaded nut interface, it is difficult to expect the experimental response to fully agree with the analytical model. Nevertheless, the registered results in the pre-sliding regime are promising.

In Fig. 4.10 and Table 4.2, the feed drive's experimental response, and its prediction considering the reduced parameter GMS friction model, are shown. In addition to displaying the excitation torque and position profiles, Fig. 4.10 shows the error of prediction, defined as $e = x - \hat{x}$. As seen, the feed drive model considering the GMS friction dynamics displays close agreement with the actual response. In the literature, the GMS model has been shown to provide much higher prediction accuracy compared to other friction models, such as LuGre, Dahl, Stribeck, and Coulomb etc. The added benefit of the proposed contribution is that by using the reduced parameter approach, the pre-sliding portion of the GMS model can now be identified more expediently, by solving a lower number of parameters in order to accurately simulate the friction.
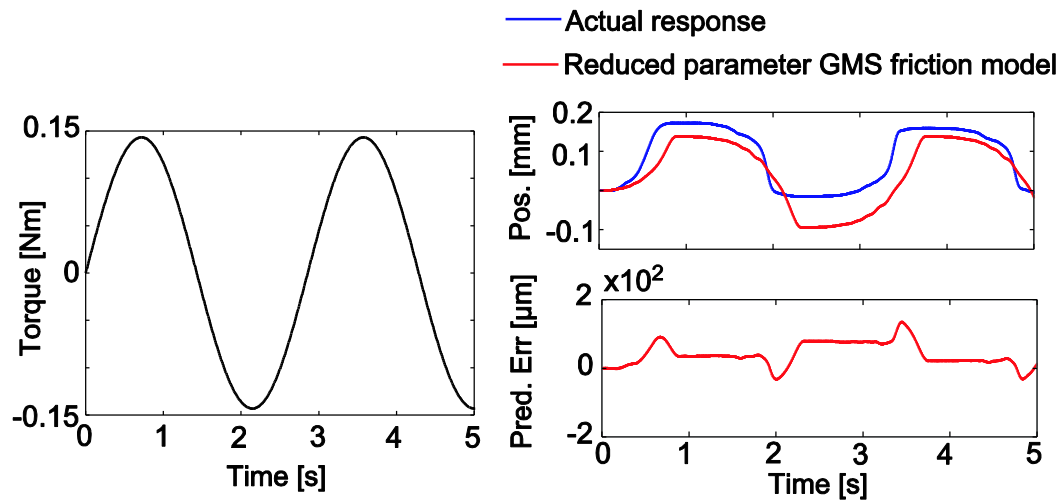
Fig. 4.10. Reduced parameter GMS friction model performance while the setup is in pre-sliding regime.

Test 2: Mixed pre-sliding and sliding response

Fig. 4.11 shows the prediction result when the experimental setup undergoes consecutive pre-sliding and sliding regimes. As seen in Table 4.2, due to the presence of more significant sliding, the prediction accuracy achieved by the GMS based model is less than that of the earlier test. However, as seen in Fig. 4.11, the GMS friction model identified through the proposed reduced parameter approach still yields a certain level of agreement in the open loop position response, even during sliding.

Table 4.2. Prediction Error RMS.

		GMS
Pre-sliding	Position Prediction RMS Error (MAX) [μm]	54 (132)
Sliding	Position Prediction RMS Error (MAX) [μm]	820 (1244)
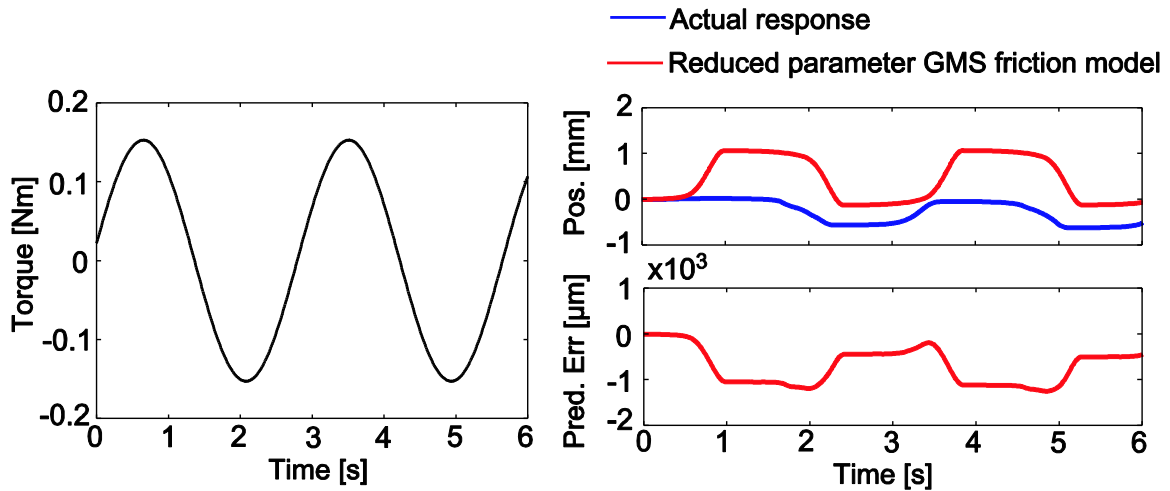
Fig. 4.11. Reduced parameter GMS friction model performance while the setup is alternating between pre-sliding and sliding regimes.

In Fig. 4.12, torque versus velocity is shown for this case. There is good agreement between the actual response and the estimated model around the pre-sliding regime. However, after 1.8 mm/s (when sliding behaviour is more dominant), there is an under estimation of friction, which leads to over prediction of the velocity by the reduced parameter GMS model. In follow-up research, this problem can be tackled by running a second iteration of optimization which also includes the Stribeck and viscous friction parameters into the search space in conjunction with the pre-sliding parameters.

Nevertheless, the experimental results demonstrate that improved prediction of friction behaviour, containing pre-sliding and sliding regimes, can be achieved in a simplified and efficient manner, with the proposed reduced parameter formulation for the GMS friction model.
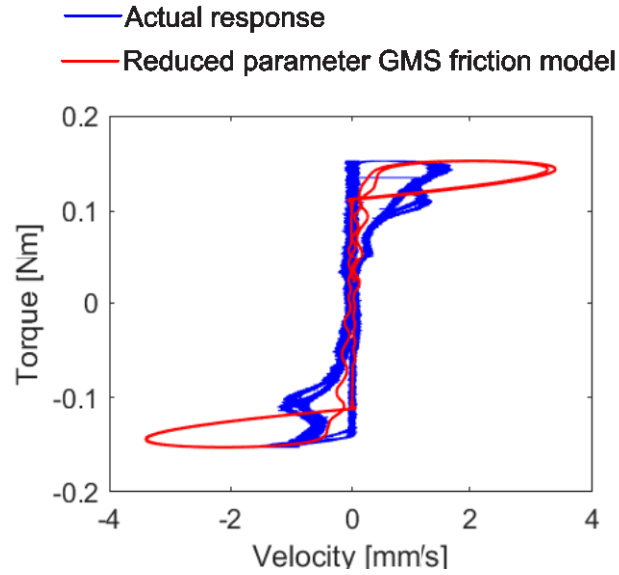
Fig. 4.12. Torque against the velocity for actual and model responses.

4.5.   Experimental Comparison with Different Friction Models (LuGre and full GMS)

So far, in this chapter, the identification and feasibility of the new approximation technique has been explained with the experimental data collected from a ball-screw setup for both pre-sliding and sliding phases. To further analyze the identified reduced order GMS model, specifically in closed-loop, a comparison study, with respect to other friction models, is presented in this section. First, the experimental setup is presented. Then, comparison results are discussed.
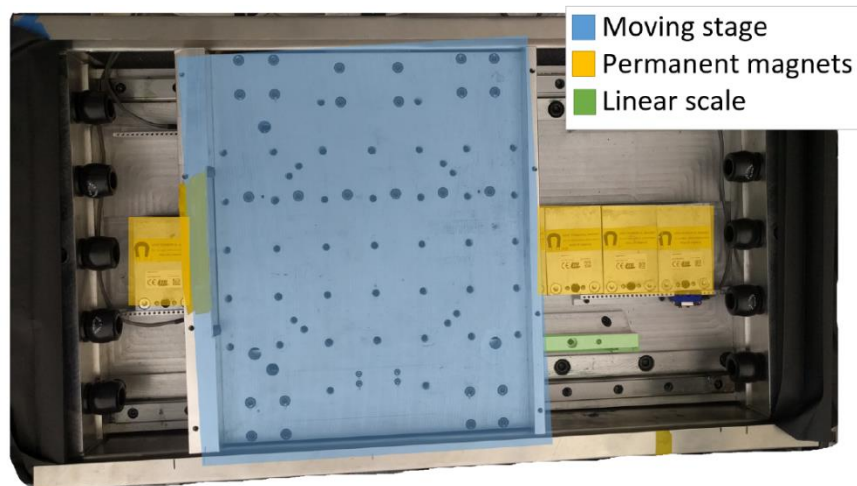
Fig. 4.13. Linear drive setup.

4.5.1.   Experimental Setup

As shown in Fig. 4.13, the experimental setup uses an ironless ETEL (ILM06-06-3RB-A20C) linear motor for actuation. Additional components include a Heidenhain (LIP 518C) encoder, linear guideways (THK SHS-15LV), and the linear motor's magnetic track (ETEL IWM060). Data was collected from the Heidenhain encoder, at a sampling frequency of 6 kHz. Portion of data used in this section are collected together with a visiting graduate student Mr. Rens Slenders from Eindoven University of Technology.

4.5.2.   Comparison Study using Closed-Loop Control

Three different friction models were considered for the comparison study: i) Coulomb ii) LuGre and iii) GMS friction models. For the last friction model, GMS parameters were first identified considering the time domain approach commonly used in literature, in which the virgin curve was constructed using piece-wise linear segments [52]. The results from this identification approach will be called 'GMS – multiple linear segment', and the model response obtained using the parameter identification technique proposed in this thesis, will be called 'GMS – reduced parameter'. Parameter identification procedure of the other two friction models is briefly explained in the proceeding.

Coulomb friction parameters were identified with the method explained in [18] along with the rigid body dynamic parameters. The Coulomb friction values for positive and negative directions were identified as $d_c = \pm 27$ N. The rigid body dynamic parameters were obtained as $m = 25$ kg and $b = 122$ kg/s.

The parameter identification for the LuGre friction model, which was explained in Chapter 2, was conducted according to the procedure explained in [60]. A pseudo random binary sequence (PRBS) signal up to 3000 Hz and an amplitude level of static friction is used to obtain an FRF measurement. The amplitude level was set to be the breakaway force, which actuated the linear drive until the setup reached the gross-limit of the pre-sliding regime. In order to model Stribeck friction ($s(v)$), the linear drive was moved back and forth for constant velocity trajectories and the disturbance state was estimated using a Kalman filter [18]. Disturbance signals were averaged for each velocity and Matlab's *fmincon* function was used to fit the Stribeck model given in Eq. (2.3). The Stribeck friction model fit, as well as the FRF for the fitted feed drive with LuGre model based on identified parameters are shown in Fig. 4.14.
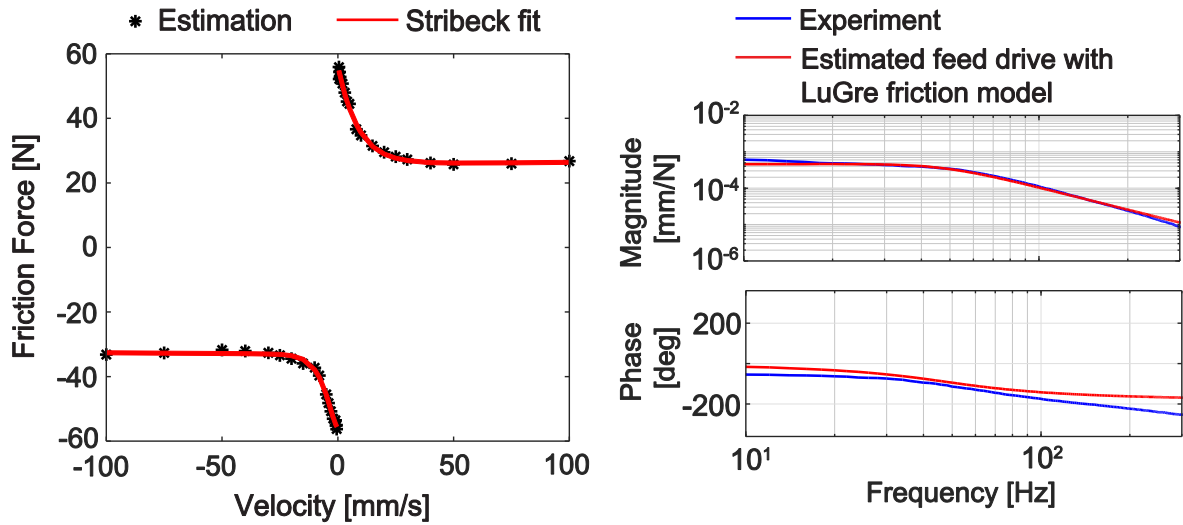
Fig. 4.14. Stribeck friction model fit (left) and LuGre friction model fit (right).
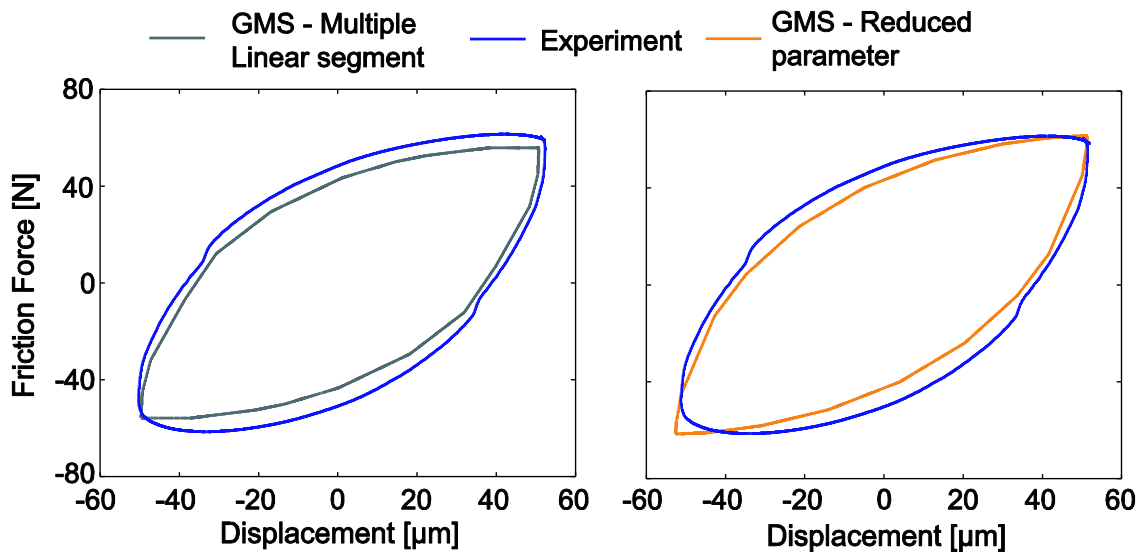
Fig. 4.15. Pre-sliding hysteresis curve fit against experimentally constructed pre-sliding curve.

To accomplish the closed-loop response tests, a P-PI position-velocity cascade controller with 30 Hz cross-over frequency and 67° phase margin was designed. Control parameters were tuned according to the procedure mentioned in [98]. The general schematic of P-PI controller is given in Fig. 2.10. The controller does not contain any feedforward action. After obtaining time-domain data from the linear drive, different friction structures were embedded within the P-PI cascade controlled system's simulation model to compare prediction errors. In Fig. 4.15, both of the fitting methods are shown. On the left, pre-sliding hysteresis curves identified with 'GMS – multiple linear segment' and on the right

'GMS – reduced parameter' results can be seen. Comparison prediction results obtained with different friction models in time-domain are shown in Fig. 4.16. In Table 4.3, friction model parameter values are given. Prediction error RMS values for each model are given in Table 4.4.

As can be seen from Table 4.3, the Coulomb friction is identified as $F_c = 27$ N while Static friction value (F_s) obtained is 56 N. Both the LuGre and GMS models obtained using a combination of linear segments have the same static friction force. However, this value differs for the reduced parameter GMS friction model, which was estimated automatically via global optimization. In this case, this value is around 62 N. As mentioned in the previous sections, to avoid discontinuous transition from pre-sliding to sliding, the breakaway (static) and Coulomb friction forces are scaled. Also, there is around 9 μm (17%) difference for breakaway displacement between 'GMS – multiple linear segment' and 'GMS – reduced parameter'.

Table 4.3. Friction parameter values for different friction models.

Stribeck friction model		LuGre friction model		GMS – Multiple linear segment		GMS – Reduced parameter	
Coulomb friction (F_c)	27 [N]	Asperity stiffness (σ_0)	2.2e+03 [N/mm]	Breakaway force (F_{br}, F_s)	56 [N]	Breakaway force (F_{br}, F_s)	62 [N]
Static friction (F_s)	56 [N]	Micro-viscous friction (σ_1)	2e+04 [Ns/mm]	Breakaway displacement (x_{br})	44 [μm]	Breakaway displacement (x_{br})	53 [μm]
Stribeck velocity factor (v_s)	5.75 [mm/s]	Viscous friction (σ_2, B)	122 [kg/s]			Shape factor (n)	0.38

As shown in Fig. 4.16, the actual (i.e. experimental) position response is compared against the feed drive dynamic model responses that contain the various friction models. RMS and MAX values of the prediction errors (difference between actual position response and model prediction) are given in Table 4.4. As can be seen, the LuGre, 'GMS – multiple linear segment', and 'GMS – reduced parameter' have about 14%, 18%, and 34% less RMS error than the Coulomb friction model, respectively. The difference between the 'GMS – reduced parameter' and 'GMS – multiple linear segment' model prediction is attributed to the two different identification schemes used in estimating the parameters. Manual fitting was implemented in the 'GMS – multiple linear segment' approach [52] by manually selected points in the open-loop pre-sliding data and connecting these points using linear segments. On

the other hand, three parameters global optimization was performed as discussed earlier in this chapter for the identification of the reduced parameter model.
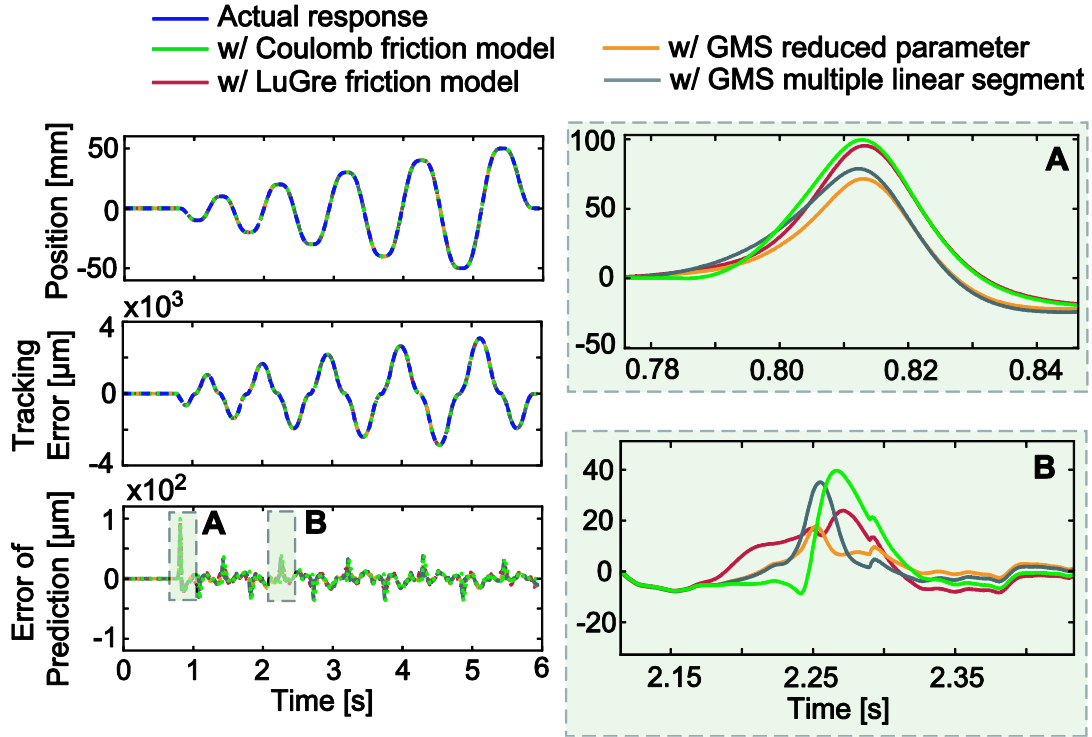
Fig. 4.16. Comparison of different friction models.

Table 4.4. Error of prediction RMS values for different friction models.

Discrepancy in Servo Error Prediction	Coulomb	LuGre	GMS – Multiple linear segment	GMS – Reduced Parameter
RMS error (MAX) [μm]	10.92 (99.67)	9.39 (95.46)	8.97 (78.82)	7.14 (71.58)

As shown in Fig. 4.16, in general, both in terms of RMS and MAX values, the GMS friction models result in better prediction accuracies. In the zoomed-in section (on the bottom-right) of Fig. 4.16, compared to the LuGre friction model, the max value of 'GMS – multiple linear segment' shows higher prediction error. However, 'GMS – multiple linear segment' shows higher prediction capability in terms of MAX value at around 0.8 s (on the top-right), also registered in Table 4.4. Overall, the GMS friction models, obtained using both parametrization approaches, compared to LuGre and Coulomb friction models, show better prediction accuracies.

4.6.   Conclusion.

A new method for approximating the GMS friction model during the pre-sliding regime has been developed. Using this approximation, side stepping the complexity of parameterizing a complete GMS friction model (with multiple slip element stiffness and force contribution factors), one can capture the essential pre-sliding characteristics with only three parameters. In the context of system identification, this greatly simplifies the parameter search problem. Once the three parameters: breakaway force, breakaway displacement, and shape factor are identified, a classical GMS pre-sliding model consisting of individual stiffness elements with their own force contributions can be constructed.

It is shown that the three parameter model can successfully approximate the experimental pre-sliding data reported in two earlier GMS studies in literature, and also the pre-sliding characteristic of a ball-screw drive system located in our lab.

The feasibility of using the reduced parameter GMS friction model is further analyzed with closed-loop control data based on a linear motor feed drive available in the lab. In the results, it is shown that the 'GMS – reduced parameter' and 'GMS – multiple linear segment' models show high prediction capability, especially around velocity reversals. 'GMS – reduced parameter' model showed better prediction results compared to full GMS model constructed by manually identifying multiple spring elements. This is mostly due to the simplification realized in the identification process due to the reduction of the number of unknown parameters. However, to draw a final conclusion regarding the performance analysis between two methods, more studies are needed.

Chapter 5

Joint Estimation of Closed-Loop Dynamics with Reduced Parameter GMS Friction Model

5.1.   Introduction

The idea of VCNC is to have virtual models of the feed drives such that necessary corrective actions can be taken ahead of time without making any physical changes to the actual system. In obtaining the feed drive dynamic model using a classical way (i.e. bottom-up approach), several time- and frequency-domain testing procedures are used. The pole-search method, presented in Chapter 3, overcomes this issue by identifying the virtual dynamic model using a minimum amount of data, typically without interfering with the production or causing downtime to the machine tool. This search approach, as proven by experimental and simulation results, was shown to be a robust and successful estimation technique, while also achieving smaller prediction error compared to using a conventional approach with full LS solution. As mentioned before, however, this method has some limitations. One limitation is the degradation of prediction accuracy in the presence of significant stick-slip friction in the actual system, especially at velocity reversals, corners, and quadrants. As a result, the identified model may show discrepancies from its physical counterpart in replicating the tracking and contouring performance. To circumvent this issue, after the pole-search algorithm, the friction dynamics can be refined further with a model which displays better fidelity than the Coulomb friction approach.

In this chapter, the reduced parameter GMS friction model, introduced in Chapter 4, is integrated with the identification of the tracking and disturbance transfer functions, as proposed by the method in Chapter 3. This integration is explained in Section 5.2. The corresponding experimental results are demonstrated in Section 5.3. In Section 5.4, a generalized form of the identification procedure of Chapter 3 is presented for the multi-input multi-output case, with the capability to also capture vibratory dynamics through the consideration of high order transfer function entries in the overall system model. This extension was realized in the graduate thesis of Ms. Ginette Tseng (MASc) and stems from the core methodology introduced in Chapter 3. Section 5.5 evaluates the integration of the reduced parameter GMS model with the multivariable identification approach, studying two different cases: a positioning system with rigid body dynamics, and a positioning system with built-in flexibility. The conclusions for this chapter are presented in Section 5.6.

5.2.   Reduced Parameter GMS Friction Model Identification with Linear Transfer Function Estimation

As mentioned in Chapter 3, an approximation of the Coulomb friction model is used in the virtual estimation process. This friction model may not adequately predict the positioning errors, especially at velocity reversals, corners and quadrants. The main reason is the dominance of pre-sliding dynamics in the low-velocity portions. To increase the fidelity of the estimated feed drive model, a dynamic friction model such as the Dahl, LuGre or GMS model can be incorporated. Here, as one of the most up-to-date friction models, the GMS model is used. Furthermore, the reduced parameter form of GMS developed in Chapter 4 is utilized to improve the efficiency and convergence of the identification problem.

The proposed identification procedure is shown in Fig. 5.1. Step 1 consists of the pole search method outlined in Chapter 3. This identification is conducted using high-velocity motion, so that the friction effects on the positioning errors are minimal, and therefore the linear transfer functions, particularly describing the tracking response, can be estimated more accurately. During this initial step, an approximate value for the Coulomb friction is also determined.

In Step 2, the identified tracking (G_{track}) and disturbance (G_{dist}) transfer functions are fixed. Now, the three GMS friction model parameters: the breakaway force (F_{br}), breakaway displacement (x_{br}) and shape factor (n), are identified. For the sliding portion of the GMS model, in order to avoid a high number of unknowns, the Stribeck characteristic is ignored and as a constant value it is set to the breakaway force. The influence of viscous friction, on the other hand, is already represented within the poles of the estimated transfer function as damping. The data set used in this case contains slow speed motion and as many velocity reversals as possible.

During Step 3, in order to account for any sub-optimality caused by the sequential fitting procedure, and also in an effort to obtain a better fit in spite of omitting the Stribeck effect, a last round of optimization concurrently modulates all identified pole, zero, and GMS model pre-sliding parameters. This step has been carried out with the slow speed data, to ensure most accurate replication of the system's response. Depending on the expected operated conditions, a mixture of slow and high-speed data can also be used.

In the implementation of this overall procedure, Matlab's multi-start and global search algorithms were used. As pointed out in [97], finding the global minimum is not guaranteed. In Steps 1 and 2, in order to increase the likelihood of obtaining a global minimum, the approach followed is to start with the

multi-start search, and then use the solution identified as the starting point for a global search algorithm. Step 3 directly uses the result of Step 2 to initiate a global search.
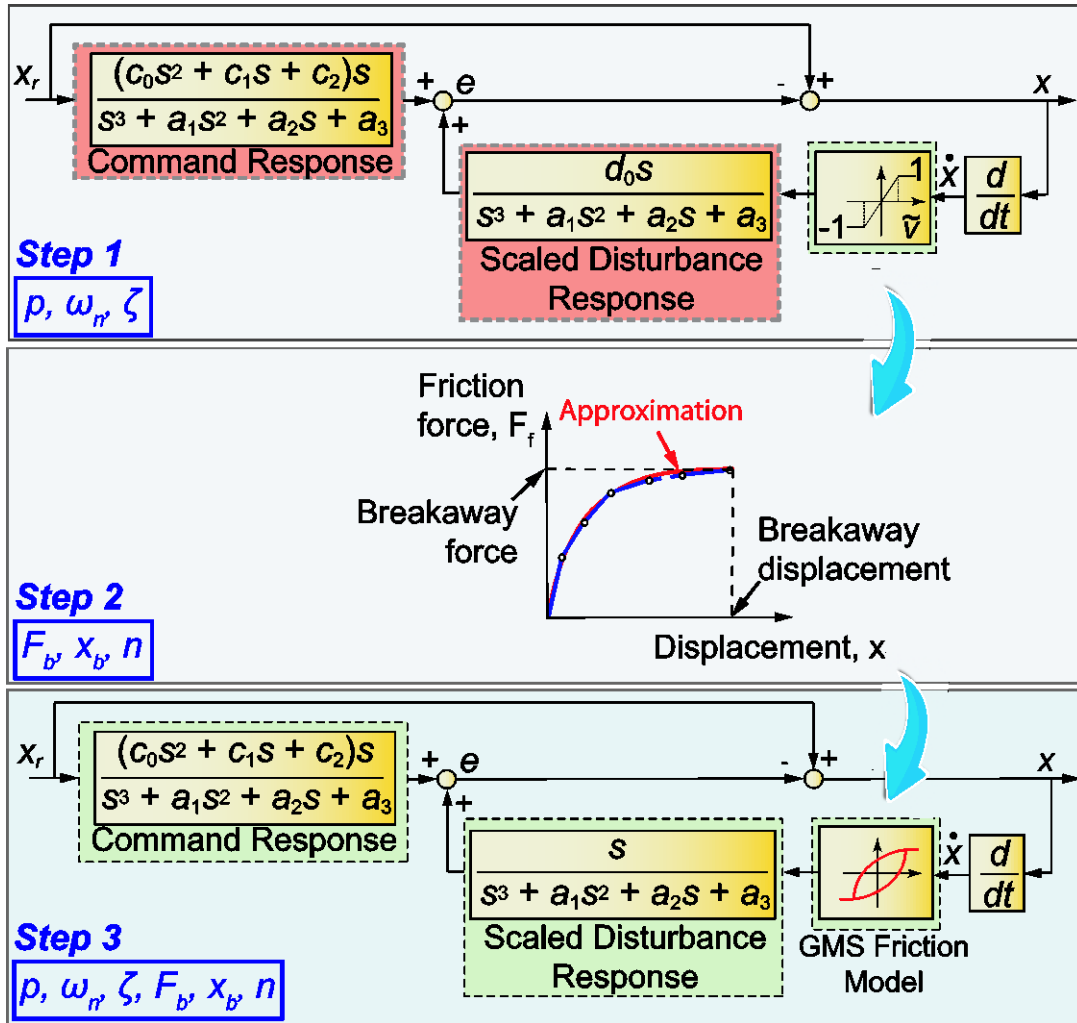
Fig. 5.1. Proposed integrated identification procedure.

5.3.   Identification Results

The data was collected from the x- and y-axes of the 5-axis machining center shown in Fig. 3.2. The motions were generated by commanding these axes in recursively increasing jerk-limited linear displacements in alternating direction, thus generating a motion profile resembling amplitude-varying sine waves in x- and y-axes. The individual axes were tested independently.
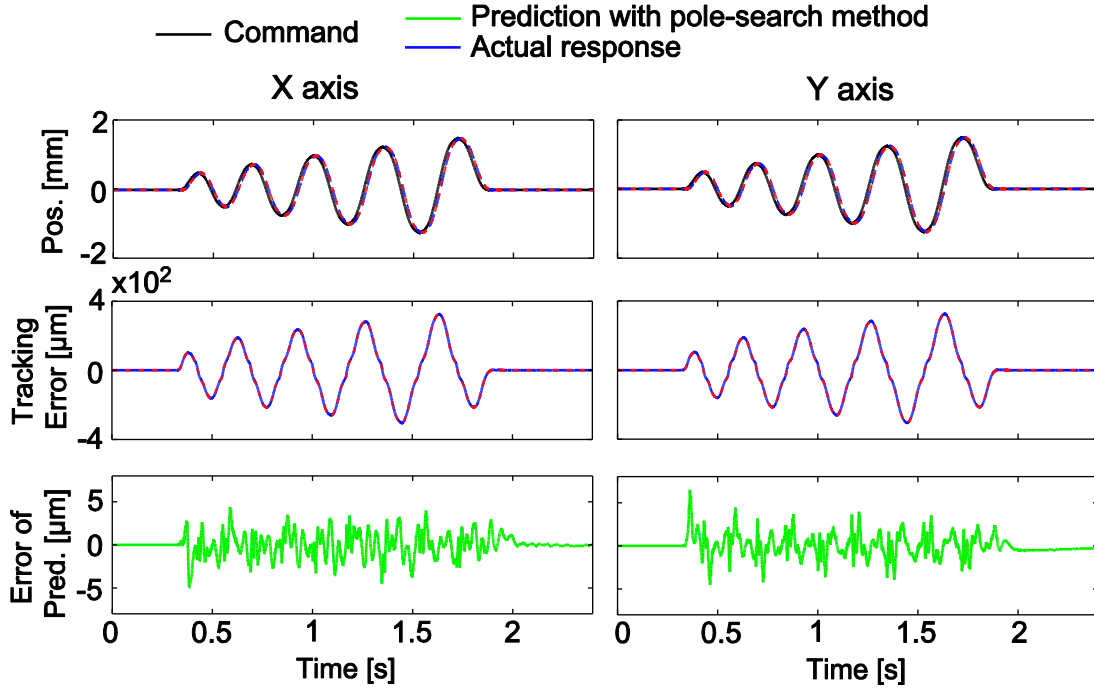
Fig. 5.2. Pole search results for x- and y-axes (after Step 1).

Table 5.1. Identified values using the pole-search method.

	p [Hz]	ω_n [Hz]	ζ
X -axis	11.66	32.29	0.49
Y-axis	16.55	37.52	0.27

The pole-search algorithm in Chapter 3 was used to construct the virtual feed drive model, per Step 1. The resulting response and estimated pole locations are shown in Fig. 5.2 and Table 5.1. As seen from Table 5.1, the x- and y-axes have similar dynamics, as discussed in Chapter 3. Considering Fig. 5.2, the tracking error is well predicted with around 1% error.

In Step 2, the estimated tracking and disturbance transfer functions are fixed and the global search estimates the reduced parameter GMS friction model. Fig. 5.3 shows the model prediction, and the comparison with the earlier result of Step 1. The experimental data determined using the measured (encoder) signal and the CNC's commanded trajectory is in blue color. The feed drive dynamic response using the Coulomb type friction model estimated from Step 1 is shown in green, and the model prediction obtained with the reduced parameter GMS model, after Step 2, is shown with red. It can be seen that the error of prediction is reduced, particularly during velocity crossings.

80
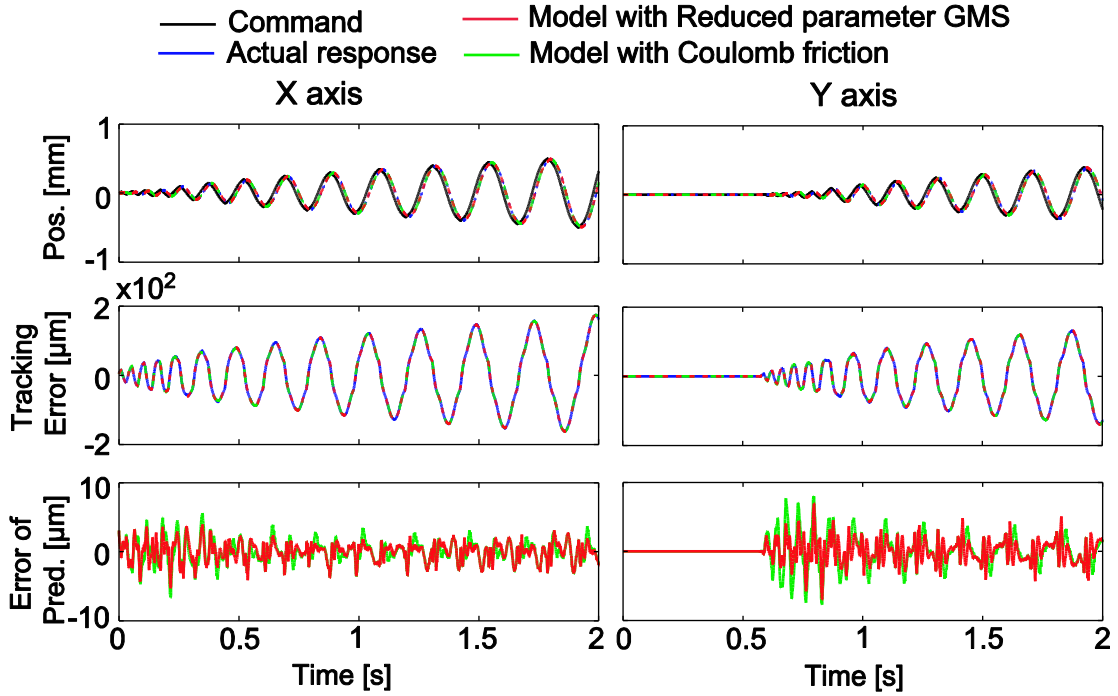
Fig. 5.3. Estimated feed drive dynamic model responses with Coulomb and GMS friction models (Step 2).

The identified reduced parameter GMS model parameters are given in Table 5.2. The RMS and MAX values for the error of prediction, as well as the relative improvements achieved, are shown in Table 5.3. The Coulomb friction coefficients of x- and y-axes obtained in Step 1 are the normalized friction values for positive and negative directions. Similarly, the breakaway forces obtained in this Step 2 have also been normalized as the breakaway friction force, as formulated below,

$$F_{br} = (K/J)F_{nb} \qquad (5.1)$$

Table 5.2. Three parameter GMS friction identification results for x- and y- axes (Step 2).

	F_{nb}	x_{br} [μm]	n
X axis	357.94	23.8	0.91
Y axis	452.07	16.5	0.76

As seen in Table 5.2 for the y-axis, the estimated normalized breakaway force (F_{nb}) is 94 units (21%) higher compared to the x-axis. This is an indication of higher friction force on y-axis. In addition, while analyzing the data collected from the 5-axis machine tool, it was observed that the movements of the x-axis occurred earlier than the y-axis (i.e. more time was needed for the y-axis to break away all pre-

81

sliding springs and reach the sliding phase). The breakaway displacement is 23.8 μm and 16.5 μm for x- and y-axes, respectively. As seen in Table 5.3, compared to the dynamic response represented with only Coulomb friction (Step 1), noticeable improvement is achieved in the RMS and MAX values of the error of prediction, by migrating to the model with the reduced parameter GMS friction dynamics (Step 2). In the x-axis, RMS and MAX values are reduced by 9.7% and 19.6%, respectively. In the y-axis, RMS and MAX values are reduced by 23% and 13.3%.

Table 5.3. Prediction error RMS and MAX values for x- and y-axes (Step 2).

Discrepancy in Servo Error Prediction	Coulomb	GMS	Improvement
X axis tracking error: RMS	1.52	1.37	9.71%
(MAX) [μm]	(6.57)	(5.38)	19.63%
Y axis tracking error: RMS	1.91	1.47	23.04%
(MAX) [μm]	(8.05)	(6.94)	13.34%

In Step 3, the pole and zero parameters of the feed drive dynamics obtained in Step 1 and the reduced parameter GMS friction model parameters obtained in Step 2 are further refined, by simultaneously including all parameters into the search space. In this step, based on the three candidate parameters for the reduced parameter GMS friction model, multi-element stiffness and contribution factors are extracted. Following the construction of the full GMS friction model, similar to Step 1, disturbance and tracking regressors are computed to construct a LS sub-problem. Here, the only difference from Step 1 is the generation of the disturbance regressor based on the candidate GMS friction model, rather than Coulomb friction. From the candidate pole locations, LS solution for the numerator coefficients is achieved. Afterwards, RMS error of the difference between actual and model predicted tracking error is evaluated, for use by the global search algorithm.

Since during Step 1 the disturbance input was modeled as Coulomb type friction, this is expected to generate slight variations in the tracking and disturbance transfer function parameters. In Fig. 5.4, the position response, servo error, and the discrepancy in servo error predictions for the two axes are presented. The identified parameter values are given in Table 5.4. RMS and MAX values for the discrepancy in servo error predictions for both friction models, and the final relevant improvements obtained going from Step 1 to Step 3, are given in Table 5.5.
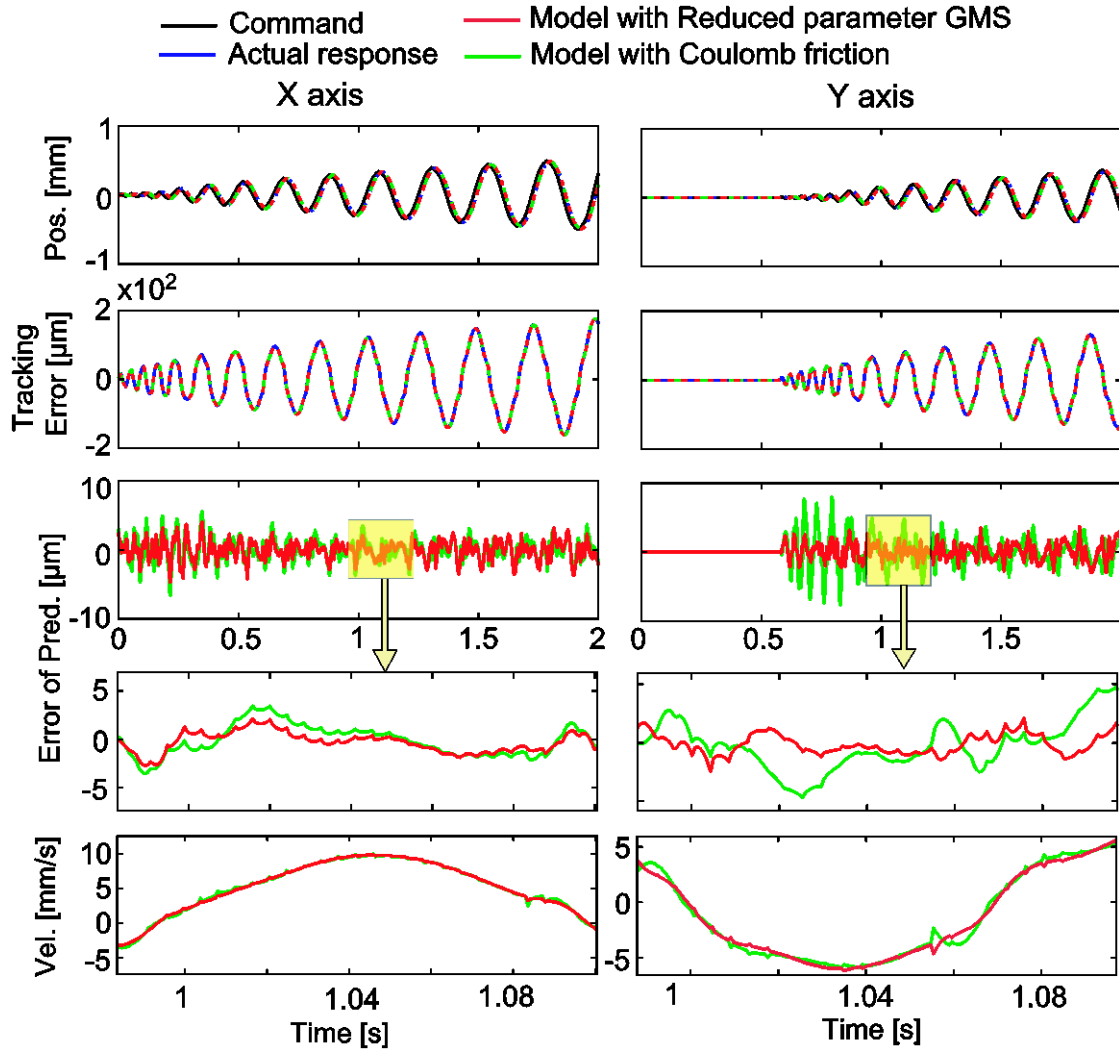
Fig. 5.4. Estimated feed drive dynamic model responses with the Coulomb and GMS friction models (Step 3).

Table 5.4. Refined pole-search and the GMS friction parameters for x and y-axes (Step 3).

	p [Hz]	ω_n [Hz]	ζ	F_{nb}	x_{br} [μm]	n
X -axis	14.94	29.58	0.38	329.16	57.8	0.88
Y-axis	27.06	40.07	0.24	454.73	5.9	0.43

As seen in Fig. 5.4, especially in the zoomed in portion of error of prediction, once the GMS friction model is embedded into the virtual model, the prediction accuracy significantly improves. This improvement is much more visible for the y-axis, especially for short motions (up to 1 sec). Within this

region, since the y-axis operates under conditions in which pre-sliding is prevalent, the improved dynamic model displays better accuracy.

In Table 5.4, as can be seen, the pole parameters (pole, natural frequency and damping ratio) have changed from Step 1. The breakaway force and shape factor are also slightly different from the parameters identified in Step 2. A major change is observed in the breakaway displacement, from 23 μm to 57 μm for the x-axis. For the y-axis, the real pole, the breakaway displacement, and shape factor have also considerably changed, from 16 to 27 Hz, 16 to 6 μm, and 0.76 to 0.43, respectively. Refinements required for the y-axis, by switching over to the GMS model, may have facilitated these changes.

As seen in Table 5.5, as a result of the updated parameters in Step 3, the RMS and MAX values of the prediction error in the x-axis are reduced by 12% and 28%, respectively. In the case of the y-axis, where stick-slip friction dominance seems to be greater, the improvements for the RMS and MAX values of the prediction error are around 44% and 54%, respectively, compared to the prediction accuracies that were obtained in Step 1. Thus, the value of integrating the reduced parameter GMS model with the newly developed top-down identification strategy is clearly demonstrated.

Table 5.5. Prediction error RMS and MAX values for x- and y-axes (Step 3).

Discrepancy in Servo Error Prediction	Coulomb	GMS	Improvement
X axis tracking error: RMS (MAX) [μm]	1.52 (6.57)	1.33 (4.7)	12.32% 28.48%
Y axis tracking error: RMS (MAX) [μm]	1.91 (8.00)	1.06 (3.71)	44.20% 53.70%

5.4. High-Order Multivariable Model Jointly Estimated with Reduced Parameter GMS Friction Model

In the earlier section, the reduced parameter GMS friction model was successfully integrated with rigid body based tracking and disturbance transfer function identifications. However, this approach considers only rigid body dynamics, whereas in machine tool, workpiece, and tooling assemblies, vibratory response due to mechanical flexibility may also be prevalent. In the remainder of this chapter, the integration of the reduced parameter GMS model with higher order dynamics is investigated.

This section introduces an extension of the methodology in Chapter 3 to the high-order multivariable case, which allows multi-input multi-output (MIMO) linear time-invariat (LTI) models of generalized feed drive control system and mechanical assemblies to be identified. This extension was accomplished in the master's thesis of Ms. Tseng [99] and published in [100]. Here, the main formulation and implementation steps are summarized. Afterwards, Section 5.5 integrates the reduced parameter GMS friction model with the MIMO estimation technique. The first step is validation of the correctness of the implementation, by considering only the rigid body dynamics. In the second step, sequential identification of the vibratory dynamics and a GMS-type friction model is investigated.
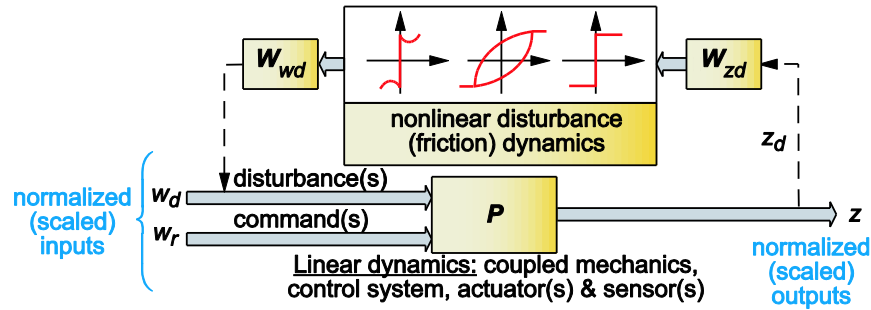
Fig. 5.5. MIMO feed drive dynamic model coupled with friction dynamics.

The MIMO model structure is shown in Fig. 5.5. Here, the generalized and scaled linear dynamics, P, is interconnected with the friction model. While a simplified Coulomb friction assumption is first made, similar to the approach taken in Chapter 3, after solving the identification of the parameters of P which implicitly contain the Coulomb friction magnitude, friction dynamics is replaced with the reduced parameter GMS model, following the same procedure as shown in Step 1 and Step 2 in Fig. 5.1.

Considering Fig. 5.5, $w_r(t)$ represents the scaled reference signal (e.g. position, velocity, or acceleration commands). $w_d(t)$ represents the disturbance input(s) (such as friction and process forces). $z(t)$ are the scaled outputs (which can represent signals such as position, velocity, acceleration, control signal, motor current, servo regulation error or any other outputs that relate dynamically to the inputs). The MIMO system response can be expressed in scaled and unscaled forms as:

$$z(s) = P(s)w(s) \qquad \text{Scaled dynamics}$$
$$\tilde{z}(s) = \tilde{P}(s)\tilde{w}(s) = (W_z P(s) W_w)\tilde{w}(s) \qquad \text{Unscaled dynamics} \tag{5.2}$$

Above, W_z and W_w are the scaling matrices. Scaling enables the transfer function fits across multiple input and output channels to be weighted in a 'balanced' manner.

85

Generally, closed-loop dynamics of typical feed drives consist of three dominant poles, where the second order comes from the rigid body dynamics and the third from the integral action of the controller. Extra complex conjugate poles are contributed by each vibratory mode [25]. $A(s)$, which is the characteristic polynomial of the closed-loop system, comprises n_r number of real poles and n_c number of complex conjugate pairs, and can be written as:

$$A(s) = A_r(s)A_c(s) = s^n + a_1 s^{n-1} + a_2 s^{n-2} + \cdots + a_{n-1}s + a_n$$
$$A_r(s) = \prod_{k=1}^{n_r}(s - p_k), \qquad A_c(s) = \prod_{k=1}^{n_c}(s^2 + 2\zeta_k \omega_k s + \omega_k^2),$$

(5.3)

Above, p_k represents real poles. ω_k and ζ_k correspond to the natural frequency and damping ratios of the complex conjugate poles, respectively. The generalized plant $\boldsymbol{P}(s)$ has N_i input and N_o output channels. Inputs ($k_i = 1, 2, \dots , N_i$) result in the response of each output (k_o), shown as z_{k_o} in Eq. (5.4). Each corresponding transfer function entry can have distinct numerator terms ($b_0, b_1, \dots , b_n$). However, all transfer function entries are set to contain the same common poles, i.e., denominator polynomial. Response of a single output z_{k_o} to multiple inputs $w_1, w_2, \dots, w_{N_i}$ is obtained as:

$$z_{k_o} = \sum_{k_i=1}^{N_i} \left[\frac{b_0^{k_o,k_i}s^n + b_1^{k_o,k_i}s^{n-1} + \cdots + b_n^{k_o,k_i}s^0}{s^n + a_1 s^{n-1} + \cdots + a_n} w_{k_i}(s) \right]$$

(5.4)

By rearranging the above equation, the regressors (φ_n^{ki}) can be constructed as:

$$z_{k_o}(s) = b_0^{k_o 1} \cdot \underbrace{\frac{s^n}{A(s)}w_1(s)}_{\varphi_0^1} + b_1^{k_o 1} \cdot \underbrace{\frac{s^{n-1}}{A(s)}w_1(s)}_{\varphi_1^1} + \cdots + b_n^{k_o 1} \cdot \underbrace{\frac{s^0}{A(s)}w_1(s)}_{\varphi_n^1}$$

$$+ b_0^{k_o 2} \cdot \underbrace{\frac{s^n}{A(s)}w_2(s)}_{\varphi_0^2} + b_1^{k_o 2} \cdot \underbrace{\frac{s^{n-1}}{A(s)}w_2(s)}_{\varphi_1^2} + \cdots + b_n^{k_o 2} \cdot \underbrace{\frac{s^0}{A(s)}w_2(s)}_{\varphi_n^2}$$

$$+ \cdots$$

$$+ b_0^{k_o N_i} \cdot \underbrace{\frac{s^n}{A(s)}w_{N_i}(s)}_{\varphi_0^{N_i}} + b_1^{k_o N_i} \cdot \underbrace{\frac{s^{n-1}}{A(s)}w_{N_i}(s)}_{\varphi_1^{N_i}} + \cdots + b_n^{k_o N_i} \cdot \underbrace{\frac{s^0}{A(s)}w_{N_i}(s)}_{\varphi_n^{N_i}}$$

(5.5)

The scaled regressors in response to the inputs are constructed based on pre-defined $A(s)$, using single-input multi-output (SIMO) transfer functions. The participation coefficients, i.e., scaled numerator terms $\bar{\boldsymbol{b}}^{k_o}$, in each output channel k_o, are computed by solving the following least-squares problem:

$$
\underbrace{\begin{bmatrix} z_{k_o}(1) \\ \vdots \\ z_{k_o}(N_t) \end{bmatrix}}_{\substack{z_{k_o}:\text{ measured} \\ \text{scaled output}}}
= \underbrace{\left[\begin{array}{ccc:c:ccc} \overbrace{\bar\varphi_0^1(1) \quad \cdots \quad \bar\varphi_n^1(1)}^{\substack{\text{scaled regressors in} \\ \text{response to input: \#1}}} & \vdots & \cdots & \vdots & \overbrace{\bar\varphi_0^{N_i}(1) \quad \cdots \quad \bar\varphi_n^{N_i}(1)}^{\substack{\text{scaled regressors in} \\ \text{response to input: \#}N_i}} \\ \bar\varphi_0^1(N_t) \ \cdots \ \bar\varphi_n^1(N_t) & \vdots & \cdots & \vdots & \bar\varphi_0^{N_i}(N_t) \ \cdots \ \bar\varphi_n^{N_i}(N_t) \end{array} \right]}_{\Phi:\text{ regressor matrix}}
\underbrace{\begin{bmatrix} \bar b_0^{k_o 1} \\ \vdots \\ \bar b_n^{k_o 1} \\ \vdots \\ \bar b_0^{k_o N_i} \\ \vdots \\ \bar b_n^{k_o N_i} \end{bmatrix}}_{\substack{\bar b^{k_o}:\text{ scaled} \\ \text{numerator}}}
+ \underbrace{\begin{bmatrix} e_{k_o}(1) \\ \vdots \\ e_{k_o}(N_t) \end{bmatrix}}_{\substack{e_{k_o}:\text{ model} \\ \text{prediction error}}}
\qquad (5.6)
$$

Further details on the mathematical formulation and numerical implementation can be found in [99][100]. One important feature to point out is that several special steps were taken in the development of [100] (such as consistently utilizing balanced discrete-time realizations in both estimation and model validation steps), to mitigate the influence of round-off errors.

The general identification procedure is shown in Fig. 5.6. First, pole candidates are selected. Then, SIMO discrete-time state-space regressors are constructed in response to one input at a time and MIMO regressors are obtained. Afterwards, the influence of multiple inputs is determined using the superposition principle. For each candidate pole set, the best fitting numerator terms are found through solving a LS subproblem (Eq. (5.6)). In determining the most successful model, an objective function which is the RMS of output prediction error is minimized by testing different candidate pole locations. After identifying the scaled model, the numerator parameters are de-normalized to produce the unscaled model, which correlates the observed physical system output to the inputs.
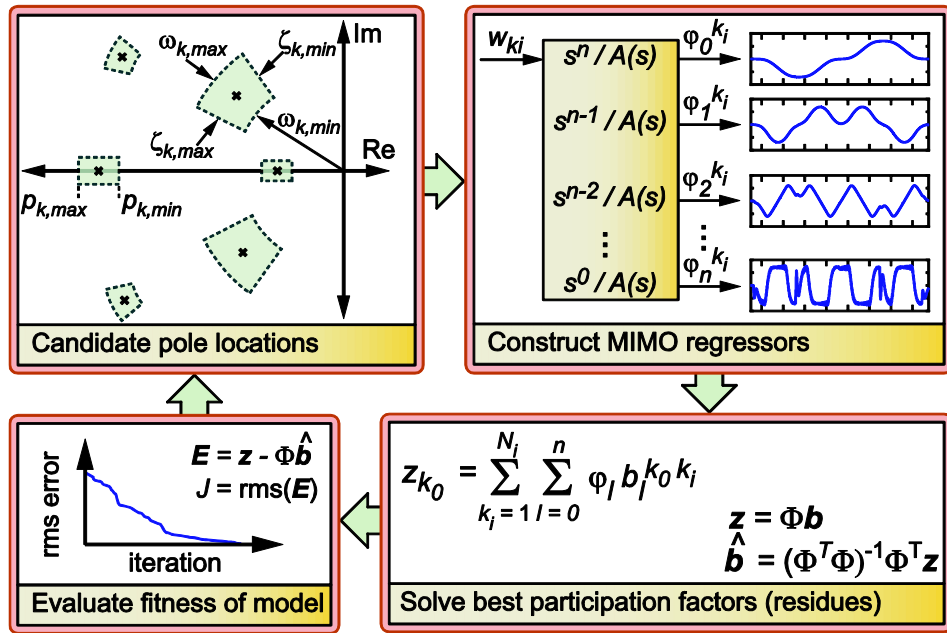
Fig. 5.6. Pole search algorithm steps for obtaining pole candidates and numerator terms.

5.5. Experimental Identification Results for the MIMO Estimation Algorithm with the Reduced Parameter GMS Model

5.5.1. Model Estimation using the Generalized MIMO Algorithm for Rigid Body Dynamics and the Reduced Parameter GMS Friction Model

Considering the structure shown in Fig. 5.5, the input signals were chosen as the position command and disturbance input. The output is the tracking error. Axis velocity, which is needed by the disturbance (friction) model, is obtained through numerical construction of the axis position from the commanded position and servo error ($x = x_r - e$), and by differentiating this signal to obtain velocity.

Table 5.6. Pole search bounds for x-axis of Deckel Maho 80P.

Parameters	Min	Max
p [Hz]	1	833
ω_n [Hz]	1	210
ζ []	0.2	2

Table 5.7. Pole-search parameter identification results for x-axis (Step 1).

p_x [Hz]	ω_{nx} [Hz]	ζ_x
12.65	32.11	0.48

$d_c = 323.2$ (Normalized Coulomb friction)
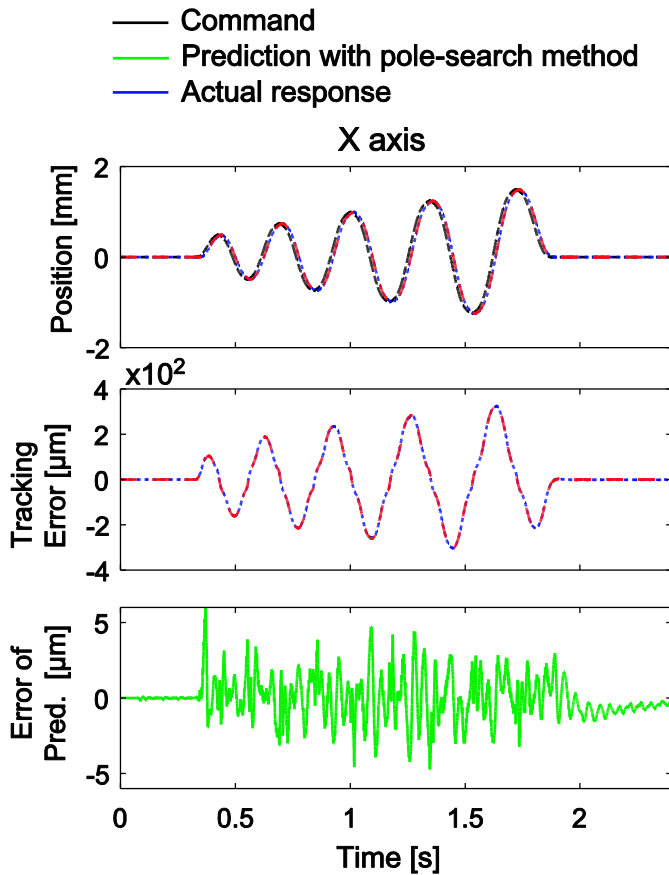
Fig. 5.7. MISO pole-search estimation results (Step 1).

The position, tracking error and error of prediction results of the first identification step are shown in Fig. 5.7. The pole search bounds are shown in Table 5.6. The identified pole, natural frequency and damping ratio can be seen in Table 5.7. As expected, the Step 1 pole search results are similar to the values obtained with the procedure obtained in Section 5.3.
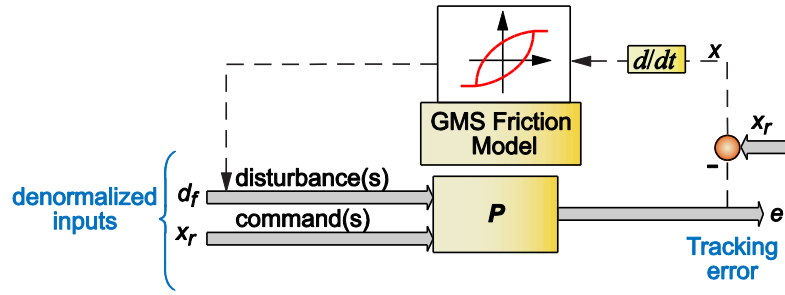
Fig. 5.8. MISO feed drive dynamic model coupled with the GMS friction dynamics (Step 2 schematic).

The schematic of the second step is shown in Fig. 5.8. Here, the Coulomb friction model is replaced with the reduced parameter GMS model. During Step 2, the linear transfer function parameters of P are fixed and only reduced three parameter GMS model coefficients (F_{br}, x_{br}, n) are adjusted. The model predictions obtained after Step 1 (with the Coulomb friction) and after Step 2 (with GMS) are compared in Fig. 5.9. As seen, especially in the zoomed portion around velocity reversals, the GMS friction model helps decrease the prediction error. It is worth mentioning that due to increased complexity of the high order MIMO model identification, Step 3 involving simultaneous adjustment of all parameters (described in Section 5.2) has been omitted. Nevertheless, significant improvement is still obtained with the step up to the reduced parameter GMS model.

The identified reduced parameter GMS friction model parameters are summarized in Table 5.8. RMS and MAX values for the prediction error are given in Table 5.9. Compared to the values given in Table 5.4, the breakaway force shows a 22% difference. There is a 16 µm (28%) difference for the breakaway displacement. The shape factor values are similar. Compared to the previous section's x-axis RMS and MAX improvements obtained in Step 3, the MIMO structure's identification results appear to achieve slightly better improvements over the Coulomb friction case, (17% vs. 12% in RMS and 30% vs. 28% in MAX), but this discrepancy could also just be originating from the different formulation and numerical methods used in the implementation of both approaches. The main result is that correct configuration and use of the MIMO method is established, which in Section 5.5.2 sets the transfer function estimation, to include vibratory dynamics.

89
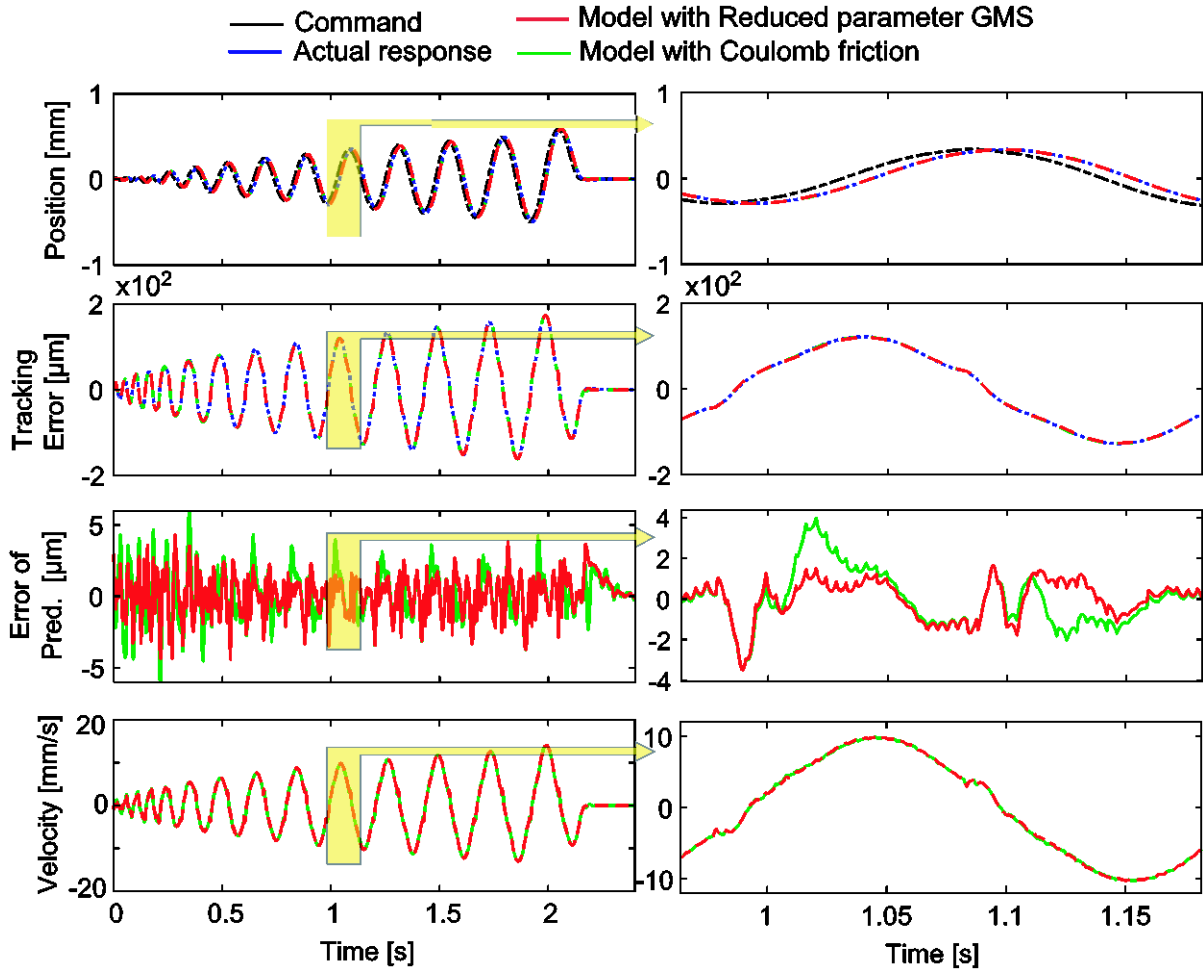
Fig. 5.9. Estimated MISO system response with Coulomb friction and reduced parameter GMS friction models (Step 2).

Table 5.8. Identified reduced parameter GMS friction model for the x-axis of DMU machine tool (Step 2).

	F_{nb}	x_{br} [µm]	n
X axis	419.58	41.8	0.90

Table 5.9. Prediction error RMS and MAX values for the x-axis of DMU machine tool (Step 2).

Discrepancy in Servo Error Prediction	Coulomb	GMS	Improvement
X axis tracking error: RMS (MAX) [µm]	1.63 (6.29)	1.36 (4.41)	16.71% 29.93%

5.5.2. Model Estimation using the Generalized MIMO Algorithm for High Order Dynamics and the Reduced Parameter GMS Friction Model

In order to generate experimental positioning data including a vibratory response, a flexure was used as shown in Fig. 5.10. The flexure design and data collection was realized by Ms. Ginette Tseng as part of her MASc research [99]. Here, this data is applied for identifying higher order dynamics together with a reduced parameter GMS model. To provide context, the following summarizes the experimental procedure.

As shown in Fig. 5.10, the positioning response was collected from two sources. The first one is the feed drive's controller (providing linear encoder measurement information from the moving carriage). This response is also suitable in determining the state of friction, as it can be considered to be collocated with respect to the net friction force acting on the carriage (originating from the guideways, ball-screw mechanism, and bearings). The second measurement is from a Heidenhain KGM grid (2D) encoder mounted on the top of the flexure. This instrument is capable of registering planar movements (in two axes) and is used for inspecting machine-tool dynamic accuracy. Its' measurement resolution is in tens of nanometers, and the instrument has a certified accuracy within ± 2 μm.

The disadvantage of using a KGM is the inconvenience of installing this type of grid encoder inside a real manufacturing machine tool, which is time-consuming and highly intrusive. When a KGM is installed, the actual machine-tool cannot perform production, since tool attachment is impossible. Furthermore, cutting chips conveyed by coolant or lubricant can easily scratch and damage the ultraprecise optical grating. Nevertheless, this is one of the most accurate methods of registering dynamic relative displacement in machine tools, particularly for diagnosis and maintenance purposes. The grid encoders' grid plate is mounted on top of the flexure. The flexure creates a vibration mode in the y-axis direction at 28 Hz. The data was collected from the feed drive's controller (Heidenhain TNC 430N) with a sampling rate of 0.6 ms for 4096 samples. Heidenhain – ACCOM software was used to capture data from the KGM with 0.1 ms intervals for 60 seconds.

As shown in Fig. 5.12, the generalized multivariable model was configured to consider the position command and the 'normalized' friction disturbance as inputs. The output signals were the relative position response collected from the KGM, and the carriage's velocity response obtained by differentiating the linear encoder position. As before in Coulomb friction estimation a saturation function with a $dv = 0.1$ mm/s velocity band was used.
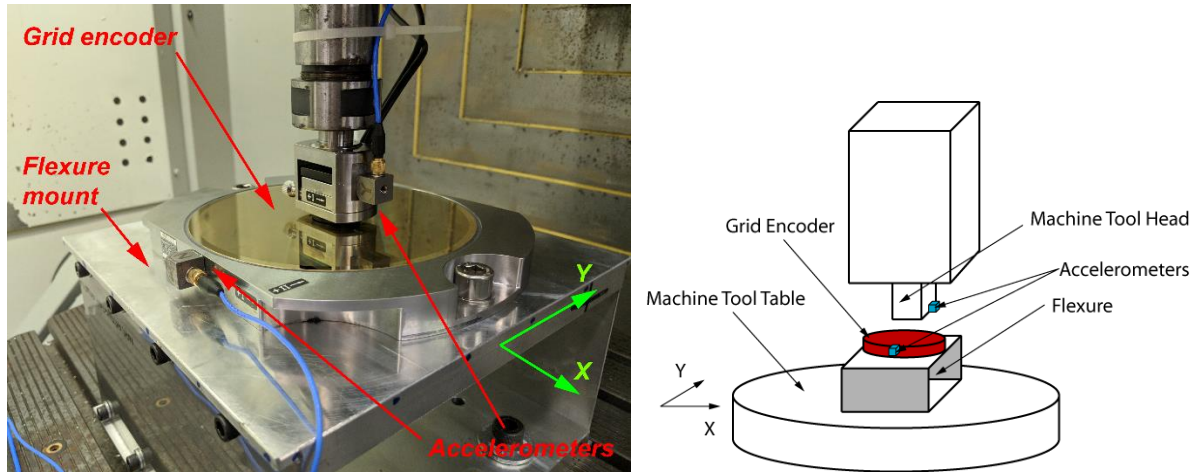
Fig. 5.10. Experimental setup [99].

Forward-backward motion with increasing displacement steps was used, as done in Section 5.5.1. Hence, the analysis focuses on the y-axis, which is the direction with artificially induced flexibility. The KGM grid encoder data was down-sampled and adequately time-offset to match the data collected from the CNC [100]. The pole search bounds are shown in Table 5.10. 833 Hz is the Nyquist frequency and 210 Hz is one quarter of the Nyquist frequency. Generally, poles originating from the servo dynamics or mechanical vibratory response stay within this limit. To enable the estimation of three real poles in a bounded manner, if needed, the upper bound of ζ_1 has been set to 2. When $\zeta \leq 2.0$ is used, upper bound selection of the natural frequency as quarter of the Nyquist frequency helps keep the fastest possible real pole below the Nyquist frequency (since $(p_1 = -\omega_n\left(\zeta + \sqrt{\zeta^2 - 1}\right) \cong -3.73\omega_n)$. Considering the estimated pole locations in Table 5.10, ω_{n1} is identified to be around 30 Hz, which is similar to the rigid body case in Section 5.5.1. ω_{n2} and ζ_2, which relate to the vibratory mechanical response of the flexure are adequately identified as 27.7 Hz and 0.01. As can be seen, the damping ratio is extremely small, indicating the presence of prolonged mechanical vibrations that will dominate the observed response.

Table 5.10. Pole search bounds and identified parameters for y-axis with added flexibility.

Parameters	Min	Max	Identified
p [Hz]	0.02	833	19.54
$\omega_{n,1}$ [Hz]	0.02	210	30.33
ζ_1	0.01	2	0.29
$\omega_{n,2}$ [Hz]	20	40	27.7
ζ_2 []	0.001	0.5	0.01

In Fig. 5.11, output predictions of the multivariable model with Coulomb friction characteristics are overlaid with the true experimental response. Considering that the tracking error reaches 500 μm, error of prediction of around 10 μm roughly indicates 2% accuracy.
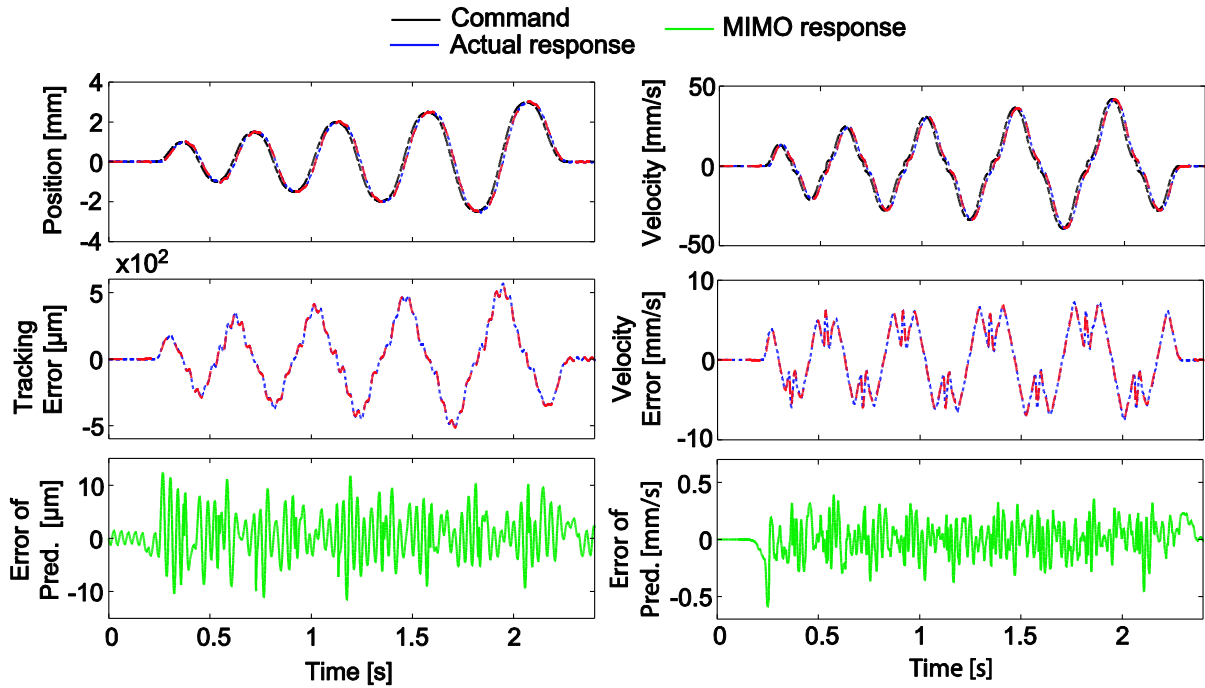
Fig. 5.11. MIMO pole-search (with Coulomb friction) prediction results (Step 1).
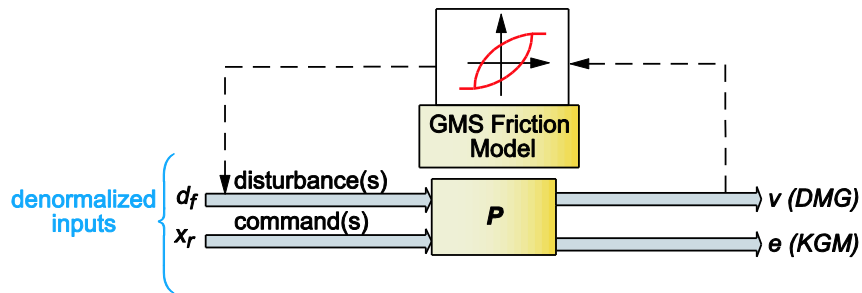
Fig. 5.12. MIMO feed drive dynamic model coupled with friction dynamics (Step 2 schematic).
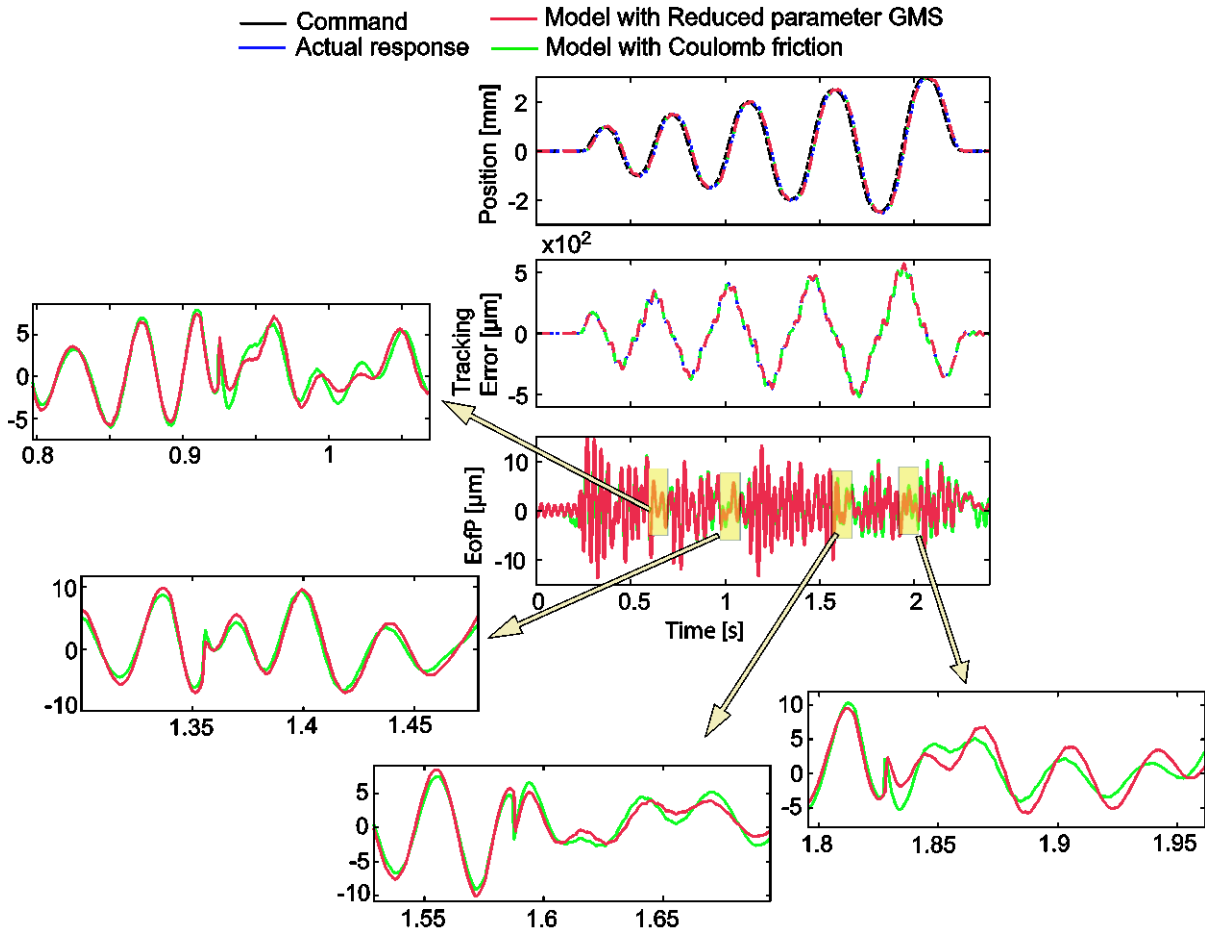
Fig. 5.13. Prediction results for estimated MIMO model with Coulomb and GMS friction dynamics (Step 2).

The results for before and after incorporating the reduced parameter GMS model are shown in Fig. 5.13. As can be seen in the tracking error profile, as the majority of the response is dominated by the mechanical vibrations, which are mainly induced by the commanded trajectory, improving the modeling of the friction input seems to provide no distinguishable improvement. In fact, the model identified in Step 1 (considering only Coulomb friction) was estimated to yield 12% better prediction accuracy up to 1.55 sec. From 1.55-2.4 sec, the GMS model showed around 7% better prediction accuracy. While, in this thesis, this was the first attempt to combine high order model estimation to include vibratory dynamics with GMS-based friction, the identification procedure only carried out Step 1 and Step 2. The simultaneous optimization of GMS friction and multivariable transfer function parameters (i.e., Step 3) was omitted, due to the substantial complexity of implementing this step. Perhaps in future research, its successful realization can help achieve even further model improvement in servo positioning systems with significant flexibility and stick-slip friction.

94

Table 5.11. Prediction error RMS values for y-axis with added flexibility.

Discrepancy in Servo Error Prediction	Coulomb	GMS	Improvement
(0 – 1.55 sec): RMS [µm]	4.34	4.98	-12.85%
(1.55 – 2.4 sec): RMS [µm]	3.75	3.49	6.93%

5.6.   Conclusions

In this chapter, closed-loop dynamics have been jointly estimated with the reduced parameter GMS friction model. After identifying and fixing the estimated tracking and disturbance response transfer functions, the reduced parameter GMS friction dynamics is embedded into the model, replacing Coulomb friction. A three-step identification procedure is proposed, in which the final step concurrently adjusts the transfer function poles and zeros, and the GMS model parameters. In experimental results collected from an industrial machine tool, it is demonstrated that this approach can lead to significant improvement in the prediction accuracy, which has been quantified as 12-44% in RMS and 28-54% in MAX values.

Thus, the two contributions made in earlier chapters, Chapter 3 and Chapter 4, are combined to achieve further impact in automatic estimation and updating of digital models for machine tool servo systems.

While these results are very promising and successful in predicting the response when rigid body dynamics are dominant along with stick-slip friction, application of this approach to a servo system with significant vibratory dynamics was also investigated. In this case, the linear transfer functions and GMS friction parameters were optimized sequentially. The global adjustment step could unfortunately not be implemented in the timeframe of this thesis. It was observed that the vibratory dynamics excited by the trajectory commands overpowered those caused by friction. Therefore, inclusion of the reduced parameter GMS model did not make any observable improvement in the system model's prediction fidelity. This is a topic that is worth investigating in future research, perhaps by also budgeting the magnitude of vibratory response and tracking errors that will be independently caused by the trajectory inputs and the friction.

The novel contribution in this chapter is the combination of reduced parameter GMS model identification with servo response transfer function estimation. Significant improvement was obtained in the resulting output predictions for systems with rigid body response dominance.

Chapter 6

Trajectory Correction using Iterative Learning Control

6.1. Introduction

Following the design and analysis in the previous chapters, this chapter investigates the correction of servo errors in multi-axis positioning and contouring systems. Iterative Learning Control (ILC) is found to be adequate for such algorithm design, since many industrial applications possess repetitive movements. On a real machine, the transient response of the system may not be adequately regulated by the controller, due to factors such as limited tracking and disturbance rejection bandwidth, modeling uncertainty, and parameter variations. ILC aims to enhance the transient response in the presence of such shortcomings, taking advantage of the possibility to perform recursive corrections on the same repetitive trajectory.
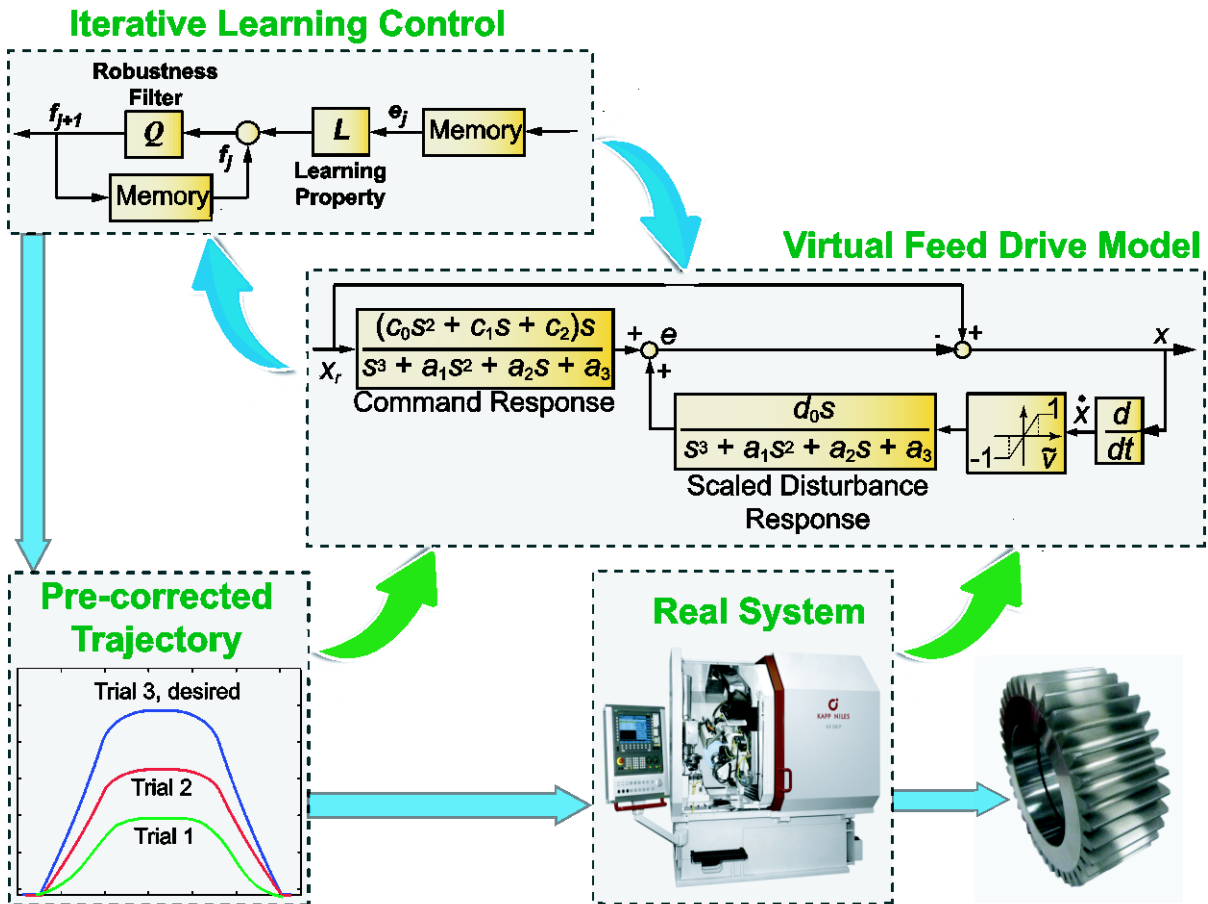

Fig. 6.1. The use of ILC together with a virtual machine.

Implementation and tuning of the learning algorithm can be done during an ongoing manufacturing process. However, this can also result in downtime to a machine's production. Instead, ILC can be used with a virtual feed drive dynamic model to improve positioning accuracy, provided that a sufficiently accurate virtual model is estimated. Also, even if the tool trajectory is not repetitive, the virtual manufacturing environment enables the possibility of performing iterative corrections through recursive simulation. The vital requirement is that the virtual model upon which ILC is based, has to be up-to-date, ideally through continuous monitoring of the real machine during its production. The use of ILC together with a virtual model, as conceptually shown in Fig. 6.1, is the fourth contribution in this thesis.

In the remainder of this chapter, ILC formulation with the virtual feed drive dynamic model is presented in Section 6.2. In Section 6.3, ILC design details are elaborated. In Section 6.4, simulation results are presented which demonstrate the improvement potential on the practical case study of gear grinding wheel dressing. To facilitate safe and reliable industrial scale testing and implementation of the developed ILC approach, the design and fabrication of an experimental platform (based on a state-of-the-art industrial CNC, the Siemens 840D SolutionLine) was initiated by the author during this thesis research. As documented in the Appendix, this implementation (which is just about complete) is expected to enable experimental validation of the developed ILC algorithm, as well as reliable transfer of the research results to industry. The conclusions for this chapter are presented in Section 6.5.

6.2. Iterative Learning Control with the Tracking and Disturbance Dynamics

In ILC, the tracking error is stored from the past iterations and the system's transient performance is improved in consequent iterations, by modifying the command to the plant. Identification of feed drive dynamics using the pole-search method was established in Chapter 3. The friction model was further refined in Chapter 4 and Chapter 5. The focus of this section is the application of ILC jointly with virtual feed drive models estimated through such methods, in order to reduce the positioning errors.

Considering the system diagram shown in Fig. 6.2, the closed-loop system has one input (x_r, periodic command signal), one output (x, actual position output), and the internal control signal (u) due to the control law. Additionally, this structure considers the disturbance signals (d). In Fig. 6.2a, the ILC algorithm is depicted with the P-PI control structure, which is widely used in industry. The ILC control signal (i.e. learning control signal, f) modifies the command that enters the closed-loop system based on the recorded tracking errors from the previous iterations. As the only alteration involves the command signal, a similar configuration of ILC can be used in the same way with the proposed virtual

model, as seen in Fig. 6.2b. In addition, for ease of formulation and simulation purposes, the identified virtual feed drive dynamics is modified to obtain the position response instead of the tracking error as shown in Fig. 3.5.
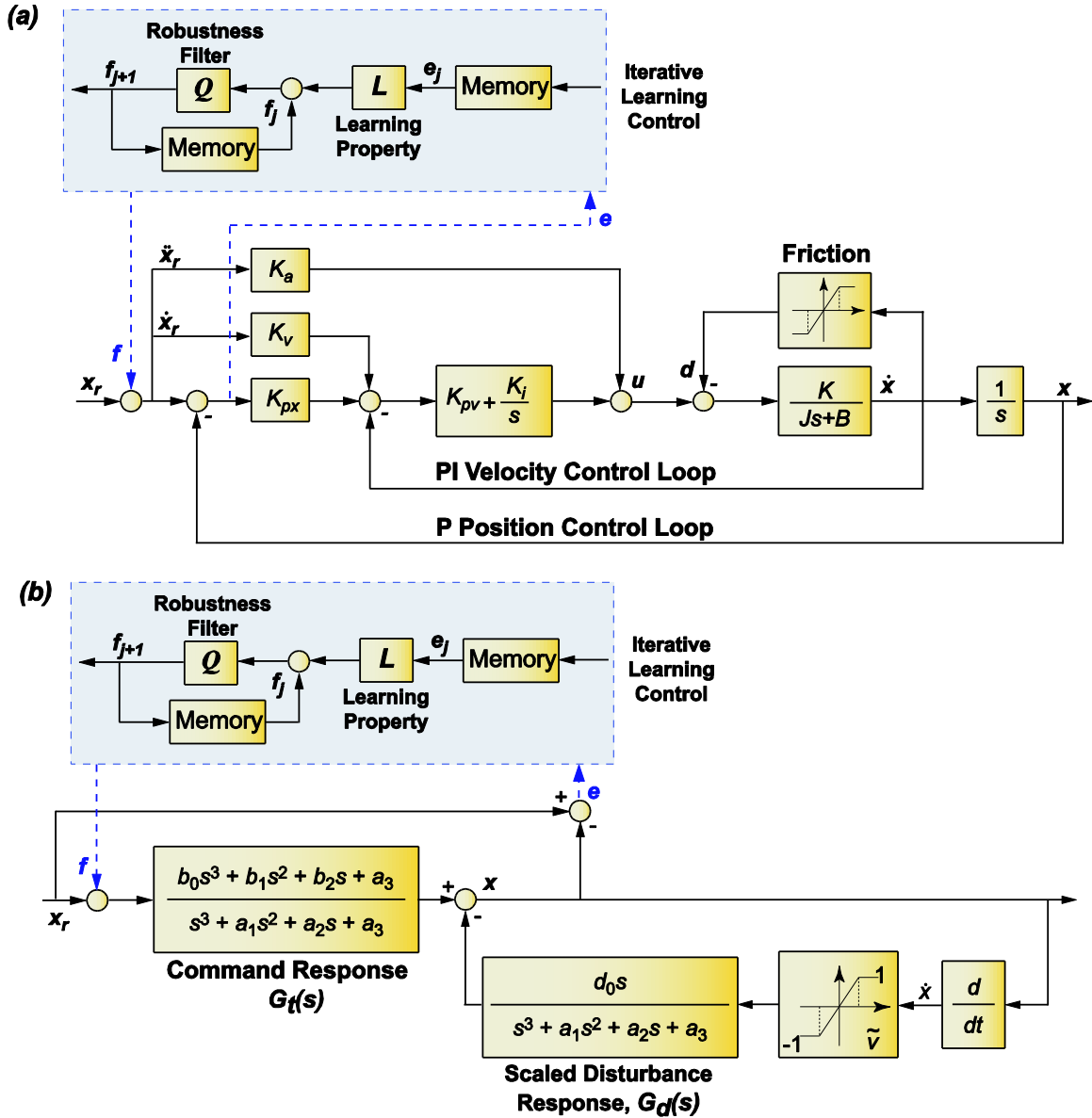
Fig. 6.2. Iterative learning control scheme: a) ILC with a typical P-PI position velocity cascade control system b) ILC with the identified virtual feed drive model.

Between the serial and parallel ILC architectures explained in Chapter 2, the serial architecture is chosen. This is mainly due to the parallel ILC altering the control signal in the feedforward/feedback control law, which is much more difficult to implement in industry. User access is generally very

restricted in industrial machine tools, especially for adjustments to the control structure, due to warranty and safety reasons.

The discrete-time system in Fig. 6.2b can be written as,

$$x[k] = G_t(z)f[k] + G_t(z)x_r[k] - G_d(z)d[k],$$ (6.1)

$G_t(z)$ and $G_d(z)$ represent the discrete-time equivalents of the closed-loop tracking and disturbance transfer functions, respectively. For a continuous time signal $y(t)$ (e.g. $y(t) = x(t)$ or $y(t) = x_r(t)$), the corresponding sampled time signal is denoted by $y[k] \triangleq y(kT_s)$, where T_s is the sampling time. The tracking error ($e[k]$) for all discrete time instants k of every iteration j is recorded as $e_j[k]$ in memory. After each iteration j, using the recorded tracking error sequence $e_j[k]$, a learning control signal f_{j+1} is generated iteratively to be used to feed into the system in the next iteration. In the generation of the learning control signal, the ILC structure in Fig. 6.2 is used. Accordingly, after each iteration j, the signal $f_j[k]$ is updated by

$$f_{j+1}[k] = Q(z)\big(f_j[k] + L(z)e_j[k]\big)$$ (6.2)

Above, $e_j[k] = x_r[k] - x_j[k]$ and $x_j[k]$ denote, respectively, the tracking error $e[k]$ and the position signal $x[k]$ in iteration j. Hence the dynamics given in Eq. (6.1), in each iteration j, takes the form

$$x_j[k] = G_t(z)f_j[k] + G_t(z)x_r[k] - G_d(z)d[k],$$ (6.3)

Here, $L(z)$ is the learning property, and $Q(z)$ is the Q-filter [81] and is chosen as "1" in some references [101], while it is used as a robustness filter (low-pass filter) in some other studies [102]. The simplest way to define the learning property ($L(z)$) of ILC is to use integral-based learning control, which generates a discrete form of integral action as given in Eq. (6.4). The learning property implements one step of integration-based corrective action upon the command input at each time step. This enables the system's error to be diminished through successive iterations [78]. The corrective action in each iteration can be expressed as:

$$f_{j+1}[k] = f_j[k] + \lambda e_j[k+1] = f_0[k] + \lambda \sum_{i=0}^{j} e_i[k+1]$$ (6.4)

The learning function L is defined to be a diagonal matrix (i.e. $L = diag(\lambda, \lambda \dots)$) [103]. However, different learning forms are also described in the literature, including those using causal compensators

[104], linear phase lead with triangular windowing [105], and linear phase lead with causal Butterworth low pass filtering [106], etc. Assuming that the closed-loop control structure is stable and linear time-invariant, the stability condition that guarantees monotonic convergence of the tracking error is given by [102]

$$\|Q(z)[1 - L(z)G_t(z)]\|_2 < 1 \tag{6.5}$$

Performance of the ILC system is assessed via the difference between the converged error $e_\infty[k]$ and the initial error $e_0[k]$, and the relation between the two errors is given by [81]

$$e_\infty[k] = \frac{1 - Q(z)}{1 - Q(z)\big(1 - L(z)G_t(z)\big)} e_0[k] \tag{6.6}$$

Another important feature of the ILC algorithms over traditional feedback and feedforward control is the possibility for ILC to predict and correct possible repeating disturbances [81]. This crucial action of ILC depends on the design of the learning algorithm. Eq. (6.2) is for the causal learning approach. However, the same equation can be reconstructed in a non-causal form as

$$f_{j+1}[k] = Q(z)\big(f_j[k] + L(z)e_j[k + 1]\big) \tag{6.7}$$

The disturbance ($d[k]$) enters the error as,

$$e_j[k] = x_r[k] - \underbrace{(G_t(z)f_j[k] + G_t(z)x_r[k] - G_d(z)d[k])}_{x_j[k]} \tag{6.8}$$

If the learning algorithm is non-causal as in Eq. (6.7), the disturbance ($d[k + 1]$) is anticipated and compensated preemptively.

6.3.   Plant-Inversion Iterative Learning Control Design

Based on Eq. (6.6), the magnitude of ($1 - LG_t$) determines the rate of convergence and successive iterations. For the design of the learning property (L), the plant inversion method is used. Since learning property is the inverse (G_t^{-1}) of the closed-loop transfer function, if G_t^{-1} is non-minimum phase, a stable inverse can be constructed using the zero-phase error tracking controller (ZPETC) [107]. This kind of learning algorithm converges quickly. However, the main shortcoming of plant-inversion learning algorithm is the effect of possible closed-loop dynamic model errors that may degrade the performance of the learning [81]. Due to the closed-loop model uncertainties, a filter (Q) is designed to increase the robustness of the learning algorithm. In addition, a constant learning gain 'λ' is also used

to multiply LG_t to tune the learning. A suitable value for the learning gain is found through trial and error, which in the case of this thesis is realized by virtual simulations.

The choice of the robustness filter (Q) as unity results in zero tracking error based on Eq. (6.6). However, as seen in Fig. 6.3, this choice makes the magnitude of $(1 - \lambda LG_t)$ exceed '1' after 50 Hz, and hence violates the monotonic convergence criterion given in Eq. (6.6). The robustness filter is designed as a second order Butterworth filter with 50 Hz cutoff frequency. The Bode plot of '$Q(1 - \lambda LG_t)$' is shown in Fig. 6.3. As can be seen, once the robustness filter is added to the learning algorithm, calculation of the 2-norm of $Q(1 - \lambda LG_t)$ results in '0.63', and hence meets the monotonic convergence criterion. In addition, as the filtering is implemented in an off-line manner, *filtfilt* function in Matlab is used to carry out the filtering, which results in zero phase error in the filtered signal.
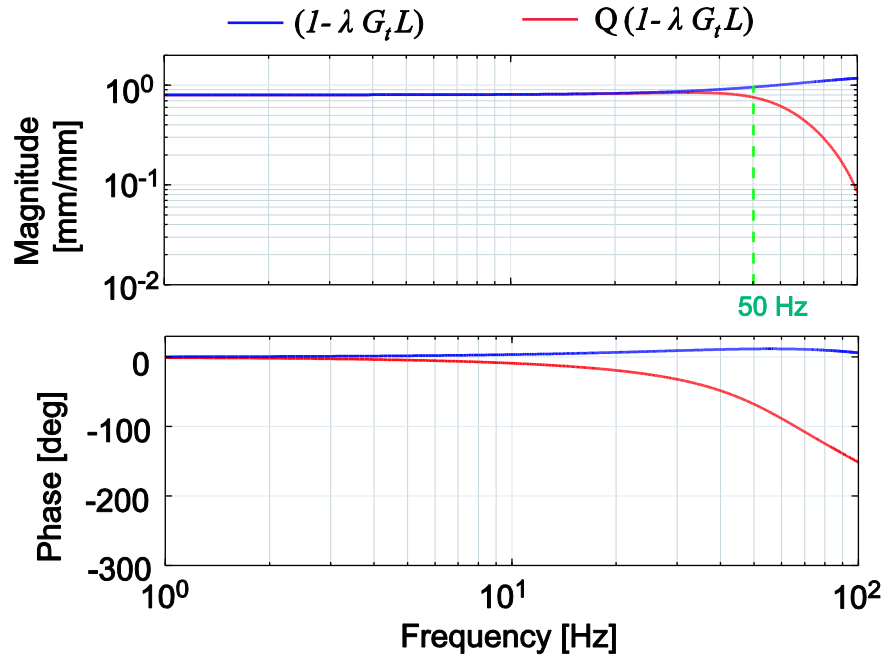
Fig. 6.3. Assessment of the monotonic stability criterion with (red line) and without (blue line) the robustness filter.

6.4. Simulation Results for Plant Inversion Based Iterative Learning Control

The simulation of ILC has been performed using the virtual dynamic model identified in Chapter 3 for the Kapp gear grinding machine tool. In the following, x- and y- axis trajectories for the grinding wheel/dressing operation are used as a case study for improving the servo positioning and contouring accuracy via ILC.
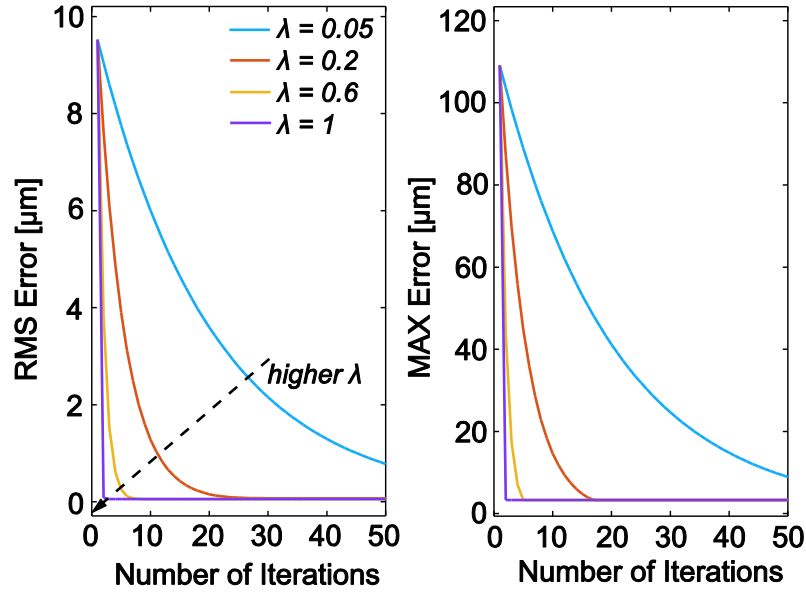
Fig. 6.4. RMS and maximum error values for different learning gains for x- axis.

First, the learning algorithm was implemented and tested for the x-axis, considering various learning gains. As can be seen in Fig. 6.4, a higher learning gain results in more aggressive learning. For example, when $\lambda = 0.05$, the RMS error is 9.53 μm for the first iteration. RMS error is decreased to 5.14 μm when the algorithm reaches its 5th iteration, which corresponds to about 46% reduction. In the case of $\lambda = 1$, this improvement is around 99.4% when the iteration number is 5. In addition, after 5 iterations, the RMS error settles to a constant value and does not change significantly during the consecutive steps. However, there is a drawback for higher learning gains: a higher learning gain results in higher sensitivity to random effects and measurement noise, as pointed out in [108]. In [108], the learning gain is selected between 0 and 2 ($\lambda \in (0, 2)$). In this thesis, the learning gain is kept below '2'. On the other hand, keeping the learning gain too small reduces the learning speed, requiring a much larger number of iterations.

ILC results for the dressing command trajectory profile are shown in Fig. 6.6. The toolpath, with the critical corner section being zoomed in, is presented at the top of the figure. The evolution of axis level tracking error profiles is shown at the bottom. RMS and MAX values for the x-axis tracking error up to 50 iterations are shown in Fig. 6.4. A learning gain of '$\lambda = 0.2$' was used for both axes. As can be seen in Fig. 6.5, similar convergent improvement behavior was also observed for the y-axis.
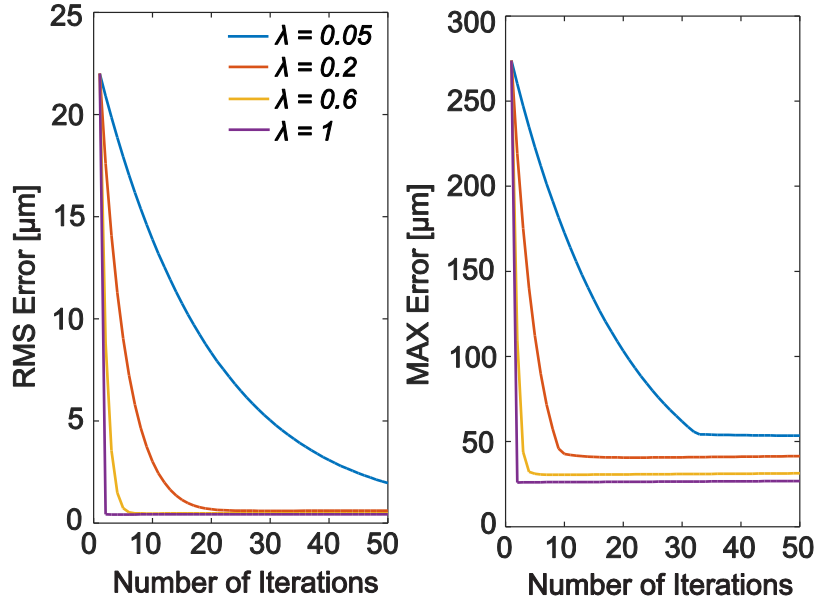
Fig. 6.5. RMS and maximum error values for different learning gains for y- axis.

Considering the top right-hand panel in Fig. 6.6, it is seen that the servo response in this contouring operation can successively be brought much closer to the desired toolpath. Tracking error in the x-axis has been decreased from an RMS value of 9.5 µm to nearly 0.07 µm, indicating two orders of magnitude improvement. The MAX value of the servo error is reduced from 109 µm to 3.3 µm after 20 iterations. These results are highly promising, and motivate experimental implementation which is on-going.

Furthermore, in Fig. 6.7, contour error results for different ILC iterations are depicted. As can be seen, the contour error is reduced from 3 µm to about 1 µm. Hence, almost 67% improvement is observed, which again shows the effectiveness of the ILC technique in simulations.

6.5.   Conclusion

In this chapter, plant inversion based ILC algorithm is designed and jointly used with the estimated virtual feed drive model to reduce positioning errors. Error reduction can be achieved while avoiding possible interruptions to the machine tool's production, which would typically occur during conventional modeling, parameter identification, or iterative trajectory correction trials. To avoid non-minimum phase or unstable closed-loop dynamics while inverting the closed-loop transfer function, the ZPETC algorithm has been used.
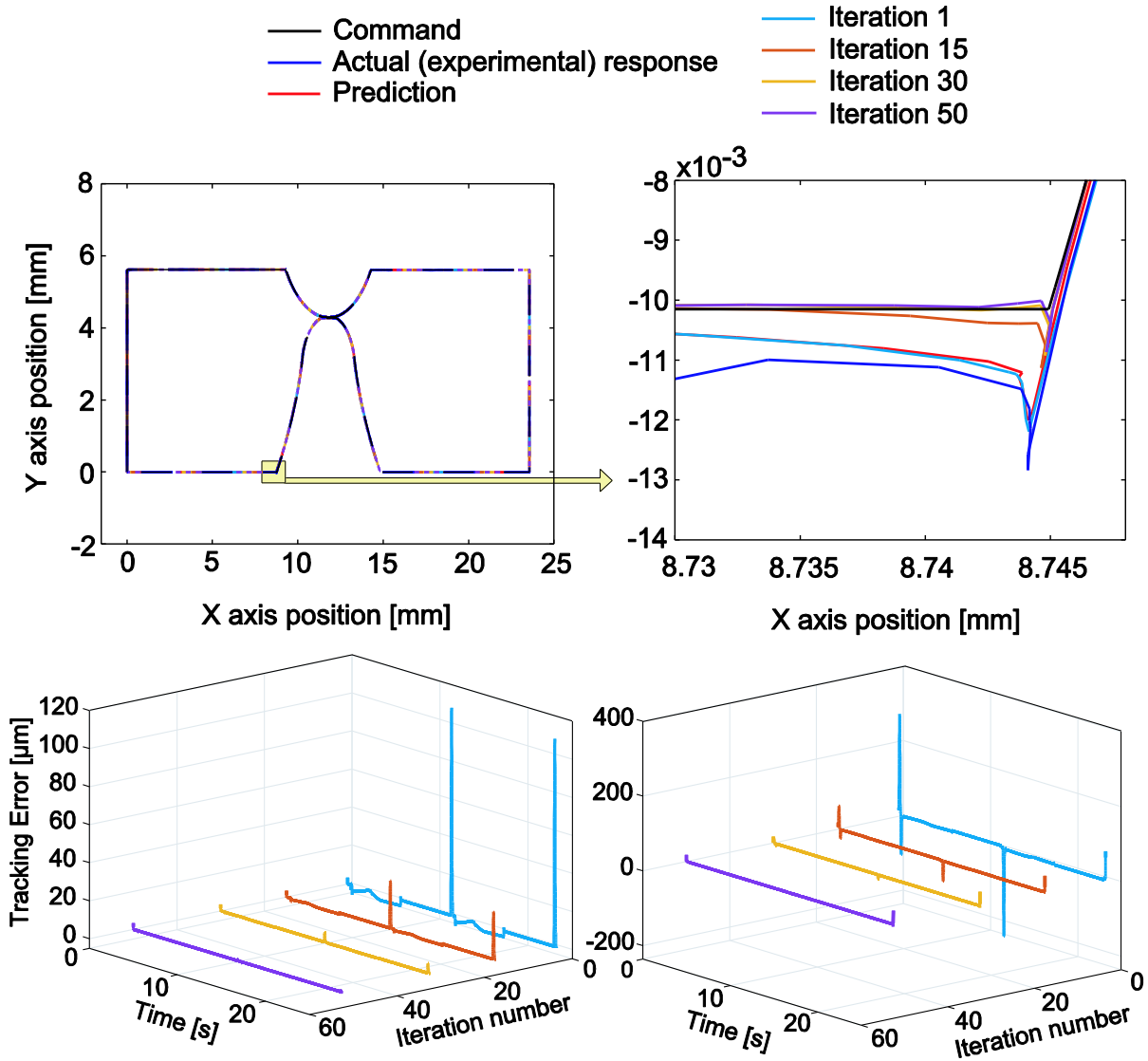
Fig. 6.6. ILC simulation results for dressing command trajectory profile.

Considering the gear grinding wheel dressing application, implementation of ILC based correction to the dressing trajectories, using in-process estimated virtual models of the grinding machine tool's x- and y-axes, has resulted in two orders of magnitude reduction in the servo errors, as predicted by simulations.

Of course, on an experimental or industrial platform, expecting such a dramatic improvement may be overly optimistic. Nevertheless, even if several-fold reduction in the servo and contouring errors are achieved, this would be a major gain towards enhancing the productivity and part quality in multi-axis manufacturing operations. Therefore, the commissioning of the experimental platform, documented in

the Appendix, for reliably testing and implementing the ILC on industry scale machine tools, is rapidly progressing.
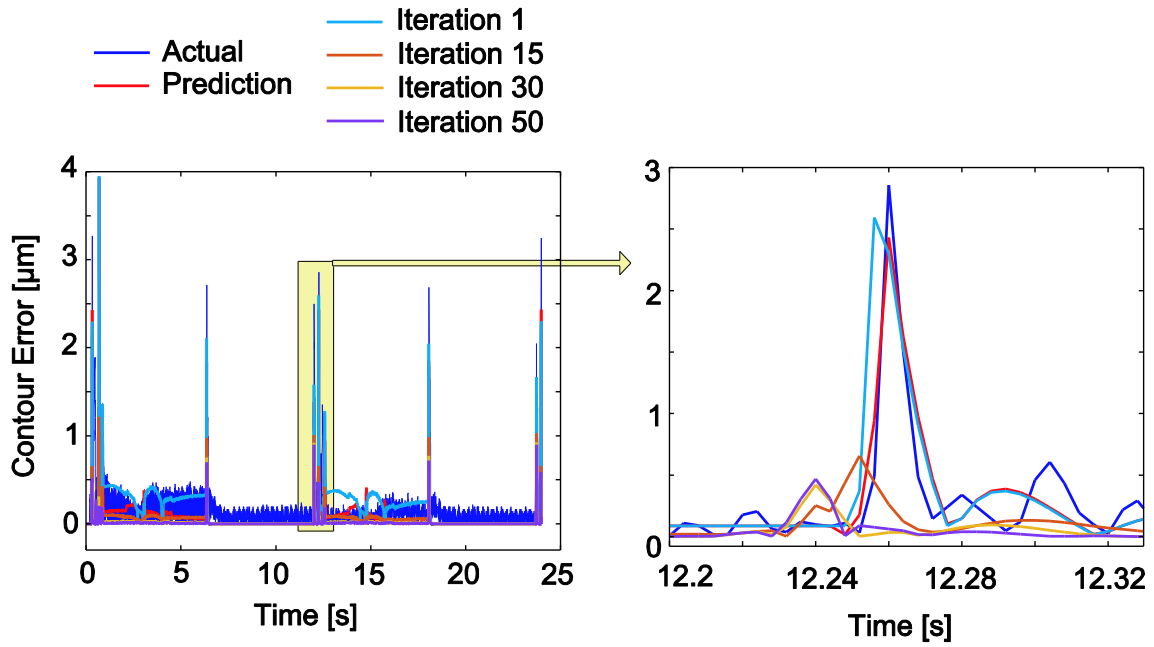
Fig. 6.7. Contour errors for different iterations for dressing toolpath profile.

Chapter 7
Conclusions and Future Work

7.1.   Thesis Conclusions

This thesis has studied new and nonintrusive model identification techniques for characterizing the dynamic response of machine tool servo drives, and a method of command trajectory correction to reduce servo errors using Iterative Learning Control (ILC).

As the first contribution, a new method for identifying the command tracking and disturbance transfer functions, from in-process data, has been proposed. The new method, based on the utilization of pole search in conjunction with least squares (LS) projection (for identifying the participation factors and the Coulomb friction magnitude), does not require the differentiation of measurement signals inside the regressor matrix. Compared to an earlier proposed rapid identification approach, based on the utilization of Least Squares in simultaneously estimating all transfer function and friction model parameters, the number of unknown variables in the LS step has been reduced from 8 to 4. This has dramatically improved the numerical conditioning, convergence, and prediction accuracy of the resulting models. With the new approach, servo errors can be predicted to within 2% accuracy. The improved estimation capability also reduces the amount of data required for training, thus allowing model identification with only real-time manufacturing data collected from a machine tool, in-line with the principles of Industry 4.0. Two experimental case studies from industry, involving a gear grinding machine tool and the multi-axis machining center, are utilized to demonstrate the new approach.

Friction remains to be one of the dominant sources of inaccuracy in machine tools. While elaborate friction models, such as the Generalized Maxwell Slip (GMS) model, can better represent and compensate friction, the number of parameters to identify to capture its most crucial (pre-sliding) portion is quite high, typically 8, 10, 12, etc. This complexity hinders the use of such sophisticated models in practical application. *As the second contribution in this thesis, a new way to formulate the pre-sliding behavior of the GMS friction model is proposed.* The new approach considers only 3 parameters: the breakaway force, breakaway displacement, and a shape factor which determines the overall geometry of the pre-sliding virgin curve. The parameterization of a suitable spline function, that can adequately synthesize GMS virgin curve patterns which agree with the data reported earlier in literature, and which are observed experimentally on additional ball-screw drive and linear motor setups, is the main novelty. The 'reduced parameter' GMS model therefore significantly accelerates

and simplifies the identification of complex friction dynamics, using only limited amounts of data. The approximation is validated through a series of experimental results, and comparison with data published earlier in the literature.

The combination of the new transfer function estimation method with the reduced parameter GMS friction model is the third contribution in this thesis. A three-step procedure is proposed, in which the transfer function estimation and reduced parameter GMS friction model identification is first conducted sequentially, and then all parameters (i.e., transfer function poles and zeros, as well as the three parameters that describe the pre-sliding behavior) are concurrently optimized. It is shown that through this process, additional 12-54% model prediction improvement is obtained, compared to only using the transfer function estimation which assumes a simplified Coulomb friction model. Attempt is also made to jointly identify high-order vibratory dynamics with GMS -type stick-slip friction. In this case, due to the dominance of the vibratory response to the commanded trajectory, significant improvement is not obtained by replacing the Coulomb friction model with reduced parameter GMS. The lack of success in this last step could also be attributed to the omission of the third step of jointly optimizing transfer function and GMS friction parameters, in order to keep the implementation manageable and straightforward.

The identified models can be used to virtually correct the commanded trajectories using Iterative Learning Control (ILC). *Development of ILC to achieve positioning accuracy improvement on an industrial case study of gear grinding wheel dressing is the fourth contribution, and its experimental implementation is still in-progress.* Simulation results based on the earlier identified virtual models have indicated up to two orders of magnitude improvement in the MAX and RMS values of the servo error, and several fold improvement in the resulting contouring accuracy. An industrial testing and validation platform, based on the Siemens 840D CNC system, has been designed and fabricated by the author and his colleagues at the University of Waterloo Precision Controls Laboratory. This setup, which is just about to be commissioned, will facilitate the experimental validation of ILC, and more importantly, safe and robust testing on an actual gear grinding machine tool in industry, such as the one at the industry partner, Ontario Drive & Gear Ltd.

7.2.   Future Research

Based on the results and experience gained through this thesis, the following short-term and long-term research tasks are proposed:

Short-term research tasks:

1 - The proposed model estimation was very successful in cases involving rigid body dynamics. Similar success could not be obtained for vibratory dynamics. Additional research into improving the estimation for feed drive systems with significant vibrations and stick-slip effects is certainly worthwhile. Analyzing the expected magnitudes of vibrations induced by different input sources would be a good step towards gaining a better understanding of the factors that are limiting the identifiability.

2 - Developing a fully automated system that continuously estimates and updates servo system transfer function and frictional dynamics from on-line manufacturing data would be highly beneficial, in terms of exploring the potential industrial applications of the methods developed in this thesis. Some possible uses could be model-based trajectory optimization, or achieving more precise prediction of the dynamic positioning accuracy in a Computer-Aided Manufacturing (CAM) environment.

3 - Experimental completion of the Iterative Learning Control implementation on the Siemens 840 CNC, and detailed testing of this approach, along with real-time virtual model estimation, in industry.

Long-term research directions:

1 - The identification methods in this thesis have considered linear and decoupled dynamics. However, in machine tools with direct drive rotary axes, and also in robotic applications, there is strong inertial coupling between the different moving axes. Extension of the identification formulation presented in Chapter 3 to such nonlinear models, and making comparisons with established methods from robotic system parameter identification literature, would be highly interesting.

2 – Full integration of high-order multi-input multi-output (MIMO) transfer function estimation capability with multiple independent reduced parameter GMS friction models, which are identified simultaneously. Automatic estimation of such models could pave the way to identify and update dynamic representations for multi-axis machines, in which there can also be cross-coupling effects

between the different axes, due to vibratory mode shapes of the machine tool structure, as well as minor but inevitable alignment errors.

3 – The ILC implementation covered in this thesis is only one of many possibilities. Researching the use of more advanced ILC approaches, such as Hankel norm ILC or H∞ norm ILC, is also recommended in the context of seeking further robustness and faster determination of corrective actions, compared to the currently implemented approach.

References

[1] Y. Altintas, C. Brecher, M. Weck, and S. Witt, "Virtual machine tool," *CIRP Annals*, vol. 54, no. 2, pp. 115–138, 2005.

[2] O. B. Abouelatta and J. Mádl, "Surface roughness prediction based on cutting parameters and tool vibrations in turning operations," *Journal of Materials Processing Technology*, vol. 118, no. 1–3, pp. 269–277, 2001.

[3] S. Engin and Y. Altintas, "Mechanics and dynamics of general milling cutters.," *International Journal of Machine Tools and Manufacture*, vol. 41, no. 15, pp. 2195–2212, 2001.

[4] E. Budak, Y. Altintas, and E. J. A. Armarego, "Prediction of milling force coefficients from orthogonal cutting data," *Journal of Manufacturing Science and Engineering*, vol. 118, no. 2, p. 216, 1996.

[5] T. Arvajeh and F. Ismail, "Machining stability in high-speed drilling—Part 1: Modeling vibration stability in bending," *International Journal of Machine Tools and Manufacture*, vol. 46, no. 12–13, pp. 1563–1572, 2006.

[6] O. Ozturk and E. Budak, "Modeling of broaching process for improved tool design," *Manufacturing*, 2003.

[7] S. Malkin and C. Guo, *Grinding Technology*. New York: Industrial Press, 2008.

[8] Y. Altintas and S. D. Merdol, "Virtual high performance milling," *CIRP Annals*, vol. 56, no. 1, pp. 81–84, 2007.

[9] Y. Altintas, P. Kersting, D. Biermann, E. Budak, B. Denkena, and I. Lazoglu, "Virtual process systems for part machining operations," *CIRP Annals*, vol. 63, no. 2, pp. 585–605, 2014.

[10] C.-H. Yeung, Y. Altintas, and K. Erkorkmaz, "Virtual CNC system. Part I. System architecture," *International Journal of Machine Tools and Manufacture*, vol. 46, no. 10, pp. 1107–1123, 2006.

[11] W. W. Wong, "Rapid identification of virtual CNC drives," M. S. thesis, University of Waterloo, Waterloo, ON, 2007.

[12] T. Chang, R. Wysk and H. Wang, *Computer-Aided Manufacturing*. Upper Saddle River, N.J.: Prentice Hall, 1998.

[13] Y. Hosseinkhani, "Control methods for improving tracking accuracy and disturbance rejection in ball-screw feed drives," Ph. D. thesis, University of Waterloo, Waterloo, ON, 2013.

[14] K. Erkorkmaz and Y. Altintas, "High speed CNC system design. Part III: High speed tracking and contouring control of feed drives," *International Journal of Machine Tools and Manufacture*, vol. 41, no. 11, pp. 1637–1658, 2001.

[15] P. Boucher, D. Dumur, and P. Rodriguez, "Robustification of CNC controllers for machine tools Motor Drives," *CIRP Annals*, vol. 52, no. 1, pp. 293–296, 2003.

[16] Y. Altintas, K. Erkorkmaz, and W.-H. Zhu, "Sliding mode controller design for high speed feed drives," *CIRP Annals*, vol. 49, no. 1, pp. 265–270, 2000.

[17] Y. Koren, *Computer Control of Manufacturing Systems*. New York, NY, USA: McGraw-Hill, 1983.

[18] K. Erkorkmaz and Y. Altintas, "High speed CNC system design. Part II: Modeling and identification of feed drives," *International Journal of Machine Tools and Manufacture*, vol. 41, no. 10, pp. 1487–1509, 2001.

[19] D. J. Ewins, *Modal Testing: Theory and Practice*. Baldock, England: Research Studies Press, 2000.

[20] C. E. Okwudire and Y. Altintas, "Hybrid modeling of ball-screw drives with coupled axial, torsional, and lateral dynamics," *Journal of Mechanical Design*, vol. 131, no. 7, 2009.

[21] D. Gordon, "Precision control of high speed drives using active vibration damping," M. S. thesis, University of Waterloo, Waterloo, ON, 2010.

[22] A. Kamalzadeh and K. Erkorkmaz, "Accurate tracking controller design for high-speed drives," *International Journal of Machine Tools and Manufacture*, vol. 47, no. 9, pp. 1393–1400, 2007.

[23] C. Okwudire, "Modeling and control of high speed machine tool deed drives," Ph. D. thesis, University of British Columbia, Vancouver, BC, 2009.

[24] D. J. Gordon and K. Erkorkmaz, "Precision control of a T-type gantry using sensor/actuator averaging and active vibration damping," *Precision Engineering*, vol. 36, no. 2, pp. 299–314, 2012.

[25] K. K. Varanasi and S. A. Nayfeh, "The dynamics of lead-screw drives: Low-order modeling and experiments," *Journal of Dynamic Systems, Measurement, and Control*, vol. 126, no. 2, p. 388, 2004.

[26] S. Frey, A. Dadalau, and A. Verl, "Expedient modeling of ball screw feed drives," *Production Engineering*, vol. 6, no. 2, pp. 205–211, 2012.

[27] G. Holroyd, "The modeling and correction of ball-screw geometric, thermal and load errors on CNC machine tools," Ph. D. thesis, The University of Huddersfield, Huddersfield, UK, 2007.

[28] R. D. Cook, *Concepts and Applications of Finite Element Analysis,* John Wiley & Sons, 2007.

[29] A. Kamalzadeh, "Precision control of high speed ball-screw drives," Ph. D. thesis, University of Waterloo, Waterloo, ON, 2008.

[30] H. Van Brussel, P. Sas, I. Nemeth, P. De Fonseca, and P. den Braembussche, "Towards a mechatronic compiler," *IEEE/ASME Transactions on Mechatronics*, vol. 6, no. 1, pp. 90–105, 2001.

[31] C. Okwudire, "Finite element modeling of ball-screw feed drive systems for control purposes," M. S. thesis, University of British Columbia, Vancouver, BC, 2005.

[32] D. A. Smith, "Wide bandwidth control of high-speed milling machine feed drives," Ph. D. thesis, University of Florida, Gainesville, FL, 1999.

[33] M. F. Zaeh and T. Oertli, "Finite element formulation of pre-stressed ball-screw drives," in *ASME 7th Biennial Conference on Engineering Systems Design and Analysis*, 2004, pp. 289-296.

[34] C. Pislaru, D. G. Ford, and G. Holroyd, "Hybrid modelling and simulation of a computer numerical control machine tool feed drive," *Proc. I MECH E Part I J. Syst. Control Eng.*, 2004, pp. 111–120.

[35] V. Lampaert, "Modeling and control of dry sliding friction in mechanical systems," Ph. D. thesis, University of Leuven, Belgium, 2003.

[36] B. Armstrong-Hélouvry, P. Dupont, and C. C. De Wit, "A survey of models, analysis tools and compensation methods for the control of machines with friction," *Automatica*, vol. 30, no. 7, pp. 1083–1138, 1994.

[37] P. Dahl, "A solid friction model," Aerospace Corp., El Segundo, CA, Tech. Rep. TOR-0158(3107-18)-1, 1968.

[38] P. Bliman and M. Sorine, "Friction modeling by hysteresis operators. Application to Dahl, stiction and Stribeck effects," *Pitman Research Notes in Mathematics Series,* pp. 10-10, 1993.

[39] P. Bliman and M. Sorine, "A system-theoretic approach of systems with hysteresis. application to friction modelling and compensation," in *Proceedings of the 2nd European control conference*, 1993, pp. 1844-1849.

[40] P. Bliman and M. Sorine, "Easy-to-use realistic dry friction models for automatic control," in *Proceedings of 3rd European Control Conference*, 1995, pp. 267-272.

[41] C. C. De Wit, H. Olsson, K. J. Astrom, and P. Lischinsky, "A new model for control of systems with friction," *Automatic Control, IEEE Transactions on,* vol. 40, pp. 419-425, 1995.

[42] J. Swevers, F. Al-Bender, C. G. Ganseman, and T. Projogo, "An integrated friction model structure with improved presliding behavior for accurate friction compensation," *IEEE Transactions on Automatic Control*, vol. 45, no. 4, pp. 675–686, 2000.

[43] F. Al-Bender, V. Lampaert, and J. Swevers, "The generalized Maxwell-slip model: a novel model for friction simulation and compensation," *IEEE Transactions on Automatic Control*, vol. 50, no. 11, pp. 1883–1887, 2005.

[44] J. Y. Yoon and D. L. Trumper, "Friction modeling, identification, and compensation based on friction hysteresis and Dahl resonance," *Mechatronics*, vol. 24, no. 6, pp. 734–741, 2014.

[45] X. Dong, X. Liu, D. Yoon, and C. E. Okwudire, "Simple and robust feedforward compensation of quadrant glitches using a compliant joint," *CIRP Annals*, vol. 66, no. 1, pp. 353–356, 2017.

[46] F. Al-Bender, "Fundamentals of friction modeling," in *Proc. ASPE Spring Topical Meeting on Control of Precision Systems*, 2010, pp. 117-122.

[47] Z. Jamaludin, "Disturbance compensation for machine tools with linear motor drives," Ph. D. thesis, University of Leuven, Belgium, 2008.

[48] M. Boegli, T. De Laet, J. De Schutter, and J. Swevers, "A smoothed GMS friction model suited for gradient-based friction state and parameter estimation," *IEEE/ASME Transactions on Mechatronics*, vol. 19, no. 5, pp. 1593–1602, 2014.

[49] T. Piatkowski, "GMS friction model approximation," *Mechanism and Machine Theory*, vol. 75, pp. 1–11, 2014.

[50] F. Villegas, R. L. Hecker, and M. Peña, "Two-state GMS-based friction model for precise control applications," *International Journal of Precision Engineering and Manufacturing*, vol. 17, no. 5, pp. 553–564, 2016.

[51] A. Dumanli and B. Sencer, "Pre-compensation of servo tracking errors through data-based reference trajectory modification," *CIRP Annals*, vol. 68, no. 1, pp. 397–400, 2019.

[52] J. Y. Yoon and D. L. Trumper, "Friction micro-dynamics in the time and frequency domains: Tutorial on frictional hysteresis and resonance in precision motion systems," *Precision Engineering*, vol. 55, pp. 101–109, 2019.

[53] C. C. de Wit and P. Lischinsky, "Adaptive friction compensation with partially known dynamic friction model," *International Journal of Adaptive Control and Signal Processing*, vol. 11, no. 1, pp. 65–80, 1997.

[54] U. Parlitz, A. Hornstein, D. Engster, F. Al-Bender, V. Lampaert, T. Tjahjowidodo, S. D. Fassois, D. Rizos, C. X. Wong, K. Worden, and G. Manson, "Identification of pre-sliding friction dynamics," *Chaos*, vol. 14, no. 2, pp. 420–430, 2004.

[55] K. Worden, C.X. Wong, U. Parlitz, A. Hornstein, D. Engster, T. Tjahjowidodo, F. Al-Bender, D.D. Rizos, and S.D. Fassois, "Identification of pre-sliding and sliding friction dynamics: Grey box and black-box models," *Mech. Syst. Signal Process.*, vol. 21, no. 1, pp. 514–534, 2007.

[56] D. D. Rizos and S. D. Fassois, "Friction identification based upon the LuGre and Maxwell slip models," *IEEE Trans. Control Syst. Technol.*, vol. 17, no. 1, pp. 153–160, 2009.

[57] V. Lampaert, S. D. Fassois, D. D. Rizos, K. Worden, D. Engster, a Hornstein, and U. Parlitz, "Measurement and identification of pre-sliding friction dynamics," *Nonlinear Dyn.*, pp. 0–20, 2003.

[58] S. J. Kim and I. J. Ha, "A frequency-domain approach to identification of mechanical systems with friction," *IEEE Trans. Automat. Contr.*, vol. 46, no. 6, pp. 888–893, 2001.

[59] Y. Y. Chen, P. Y. Huang, and J. Y. Yen, "Frequency-domain identification algorithms for servo systems with friction," *IEEE Trans. Control Syst. Technol.*, vol. 10, no. 5, pp. 654–665, 2002.

[60] R. H. A. Hensen, M. J. G. van de Molengraft, and M. Steinbuch, "Frequency domain identification of dynamic friction model parameters," *IEEE Trans. Control Syst. Technol.*, vol. 10, no. 2, pp. 191–196, 2002.

[61] M. Ruderman and T. Bertram, "FRF based identification of dynamic friction using two-state friction model with elasto-plasticity," in *2011 IEEE Int. Conf. Mechatronics, ICM 2011 - Proc.*, 2011, pp. 230–235.

[62] M. Hermann, T. Pentek, and B. Otto, "Design principles for industry 4.0 scenarios," in *Proceedings of the Annual Hawaii International Conference on System Sciences*, 2016.

[63] S. J. Qin, "An overview of subspace identification," *Comput. Chem. Eng.*, vol. 30, no. 10–12, pp. 1502–1513, 2006.

[64] U. Forssell and L. Ljung, "Closed-loop identification revisited," *Automatica*, vol. 35, no. 7, pp. 1215–1241, 1999.

[65] J. Jeng and Y. Lin, "Closed-loop identification of dynamic models for multivariable systems with applications to monitoring and redesign of controllers," *Ind. Eng. Chem. Res,* pp. 1460–1472, 2011.

[66] I. Gustavsson, L. Ljung, and T. Söderström, "Survey paper: Identification of processes in closed loop-identifiability and accuracy aspects," *Automatica*, vol. 13, no. 1, pp. 59–75, 1977.

[67] Q. G. Wang, Y. Zhang, and X. Guo, "Robust closed-loop identification with application to auto-tuning," *J. Process Control*, vol. 11, no. 5, pp. 519–530, 2001.

[68] R. Silva, D. Sbárbaro, and B. A. León de la Barra, "Closed-loop process identification under PI control: A time domain approach," *Ind. Eng. Chem. Res.*, vol. 45, no. 13, pp. 4671–4678, 2006.

[69] U. Forssell and L. Ljung, "Identification for control: some results on optimal experiment design," in *Proc. 37th IEEE Conf. Decis. and Control*, Tampa, FL, USA, 1998, pp. 3384-3389.

[70] B. Sencer and Y. Altintas, "Identification of 5-axis machine tools feed drive systems for contouring simulation," *International Journal of Automation Technology*, vol. 5, no. 3, pp. 377–386, 2011.

[71] R. Neugebauer, S. Ihlenfeldt, A. Hellmich, and H. Schlegel, "Modelling feed drives based on natural excitation—improving accuracy," *CIRP Ann. - Manuf. Technol.*, vol. 66, no. 1, pp. 369–372, 2017.

[72] A. Hellmich, K. Hipp, H. Schlegel, and R. Neugebauer, "Parameter identification of NC-axes during regular operation of a machine tool," *Advanced Materials Research,* vol. 1018, pp. 419-426, 2014.

[73] K. Erkorkmaz and W. Wong, "Rapid identification technique for virtual CNC drives," *International Journal of Machine Tools and Manufacture*, vol. 47, no. 9, pp. 1381–1392, 2007.

[74] W. W. Wong and K. Erkorkmaz, "Constrained identification of virtual CNC drives using a genetic algorithm," *Int. J. Adv. Manuf. Technol.*, vol. 50, no. 1–4, pp. 275–288, 2010.

[75] H. Ahn, K. Moore and Y. Chen, *Iterative Learning Control*. New York: Springer, 2007.

[76] J. Xu, S. Panda and T. Lee, *Real-Time Iterative Learning Control*. London: Springer, 2009.

[77] S. Arimoto, S. Kawamura, and F. Miyazaki, "Bettering operation of robots by learning," *J. Robot. Syst.*, vol. 1, no. 2, pp. 123–140, 1984.

[78] R. Longman, "Iterative learning control and repetitive control for engineering practice," *Int. J. Control*, vol. 73, no. 10, pp. 930–954, 2000.

[79] H.-S. Ahn, Y. Chen, and K. L. Moore, "Iterative learning control: Brief survey and categorization," *IEEE Transactions on Systems, Man and Cybernetics, Part C (Applications and Reviews)*, vol. 37, no. 6, pp. 1099–1121, 2007.

[80] Y. Wang, F. Gao, and F. J. Doyle, "Survey on iterative learning control, repetitive control, and run-to-run control," *Journal of Process Control*, vol. 19, no. 10, pp. 1589–1600, 2009.

[81] D. A. Bristow and M. Tharayil, and A. G. Alleyne "A survey of iterative learning control," *IEEE Control Systems Magazine*, vol. 26, no. 3, pp. 96–114, 2006.

[82] K. L. Moore, M. Dahleh, and S. P. Bhattacharyya, "Iterative learning control: A survey and new results," *Journal of Robotic Systems*, vol. 9, no. 5, pp. 563–594, 1992.

[83] O. Markusson, H. Hjalmarsson, and M. Norrlöf, "Iterative learning control of nonlinear non-minimum phase systems and its application to system and model inversion," in *Proc. IEEE Conf. Decis. Control*, 2001, pp. 4481-4482.

[84] T. J. Harte, J. Hätönen, and D. H. Owens, "Discrete-time inverse model-based iterative learning control: stability, monotonicity and robustness," *International Journal of Control*, vol. 78, no. 8, pp. 577–586, 2005.

[85] K. L. Barton and A. G. Alleyne, "A Cross-Coupled Iterative Learning Control Design for Precision Motion Control," *IEEE Transactions on Control Systems Technology*, vol. 16, no. 6, pp. 1218–1231, 2008.

[86] W. Chen and M. Tomizuka, "Dual-stage iterative learning control for MIMO mismatched system with application to robots with joint elasticity," *IEEE Trans. Control Syst. Technol.*, vol. 22, no. 4, pp. 1350–1361, 2013.

[87] C. Wang, Y. Zhao, Y. Chen, and M. Tomizuka, "Nonparametric statistical learning control of robot manipulators for trajectory or contour tracking," *Robotics and Computer-Integrated Manufacturing*, vol. 35, pp. 96–103, 2015.

[88] C. Wang, M. Zheng, Z. Wang, C. Peng, and M. Tomizuka, "Robust Iterative Learning Control for Vibration Suppression of Industrial Robot Manipulators," *Journal of Dynamic Systems, Measurement, and Control*, vol. 140, no. 1, 2017.

[89] G. K. Parmar, "Dynamics and control of flexure-based large range nano-positioning systems", Ph. D. thesis, University of Michigan, Ann Arbor, MI, 2014.

[90] Kapp, "Gear Centre KX 300P – Operating Instructions", 2008.

[91] Siemens, "Siemens 840D User Manual", 2008.

[92] Y. Shih and S. Chen, "Free-form flank correction in helical gear grinding using a five-axis computer numerical control gear profile grinding machine", *Journal of Manufacturing Science and Engineering*, vol. 134, no. 4, 2012.

[93] L. Ljung, *System Identification Theory for the User.* Englewood Cliffs, NJ: Prantice-Hall, 1987.

[94] H. Olsson and K. J. Åström, "Friction generated limit cycles," *IEEE Trans. Control Syst. Technol.*, vol. 9, no. 4, pp. 629-636, 2001.

[95] V. Lampaert, F. Al-Bender, and J. Swevers, "A generalized Maxwell-slip friction model appropriate for control purposes," in *Proc. IEEE Int. Conf. Physics and Control*, St. Petersburg, Russia, 2003, pp. 1170-1178.

[96] Z. Jamaludin, H. Van Brussel, and J. Swevers, "Quadrant glitch compensation using friction model-based feedforward and an inverse-model-based disturbance observer," in *10th IEEE International Workshop on Advanced Motion Control*, 2008, pp. 212-217.

[97] Global Optimization Toolbox. The MathWorks Inc. 2012.

[98] G. Ellis, *Control System Design Guide a Practical Guide.* Amsterdam: Elsevier Academic Press, 2004.

[99] G. W. G. Tseng, "Digital twin feed drive identification for virtual process planning", M. S. thesis, University of Waterloo, Waterloo, ON, 2018.

[100] G. W. G. Tseng, C. Q. G. Chen, K. Erkorkmaz, and S. Engin, "Digital shadow identification from feed drive structures for virtual process planning," *CIRP Journal of Manufacturing Science and Technology*, vol. 24, pp. 55–65, 2019.

[101] M. Norrlöf and S. Gunnarsson, "Time and frequency domain convergence properties in iterative learning control," *Int. J. Control*, vol. 75, no. 14, pp. 1114–1126, 2002.

[102] G. Parmar, K. Barton, and S. Awtar, "Large dynamic range nano-positioning using iterative learning control," *Precis. Eng.*, vol. 38, no. 1, pp. 48–56, 2014.

[103] M. Phan and R. Longman, "A mathematical theory of learning control for linear discrete multivariable systems", *Astrodynamics Conference*, 1988.

[104] H. Elci, R. Longman, Minh Phan, Jer-Nan Juang and R. Ugoletti, "Discrete frequency based learning control for precision motion control", in *Proceedings of IEEE International Conference on Systems, Man and Cybernetics*, 1994.

[105] Y. Wang, R. Longman, "Use of non-causal digital signal processing in learning and repetitive control", *Astrodynamics*, 1995.

[106] Y. Hsin, P. Longman, R. W. Solcz, J. Jong, "Experiments bridging learning and repetitive control", *Spaceflight mechanics*, 1997.

[107] M. Tomizuka, "Zero Phase Error Tracking Algorithm for Digital Control," *Journal of Dynamic Systems, Measurement, and Control*, vol. 109, no. 1, p. 65, 1987.

[108] T. Oomen, C. R. Rojas, "Sparse Iterative Learning Control (SPILC): When to Sample for Resource-Efficiency?" in *IEEE 15th International Workshop on Advanced Motion Control,* 2018.

Appendix A

Siemens 840D SL Controller

Sinumerik 840D SL is a universal and flexible CNC system that has SINAMICS S120 drive components. This system has been built to be used as a universal validation and development testbench to support modeling, controls, and trajectory optimization research and facilitate easy industrial migration. Mr. Chia-Pei Wang and Mr. Jay Woo were also involved in Siemens controller assembly. Also, the servo enclosure was designed and built by the visiting graduate student Mr. Rens Slenders (TU Eindhoven). Electrical connections were completed by Mr. James Merli (Department technician). The assembled picture of this controller and the connection schematic can be seen in Fig. A.1 and Fig. A.2, respectively.
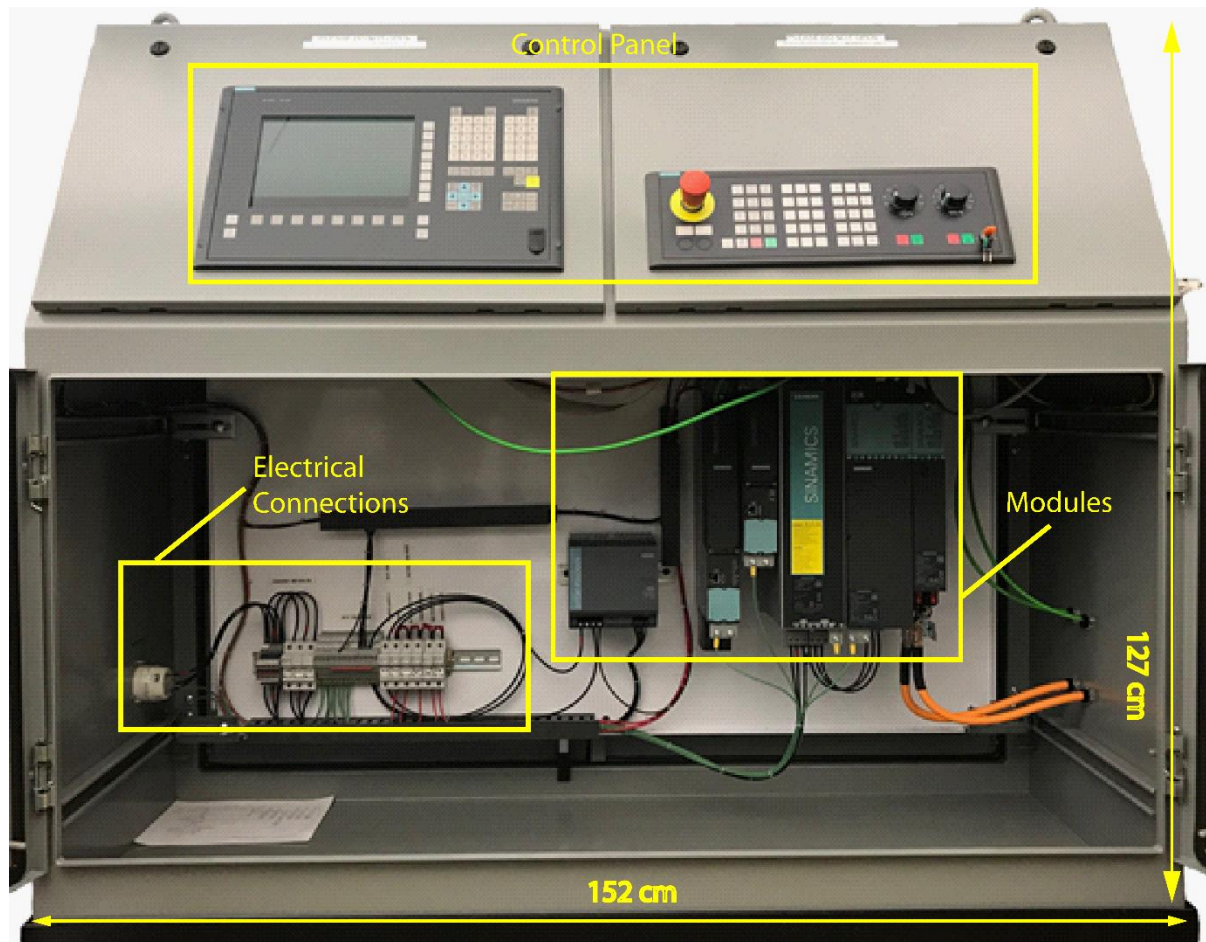

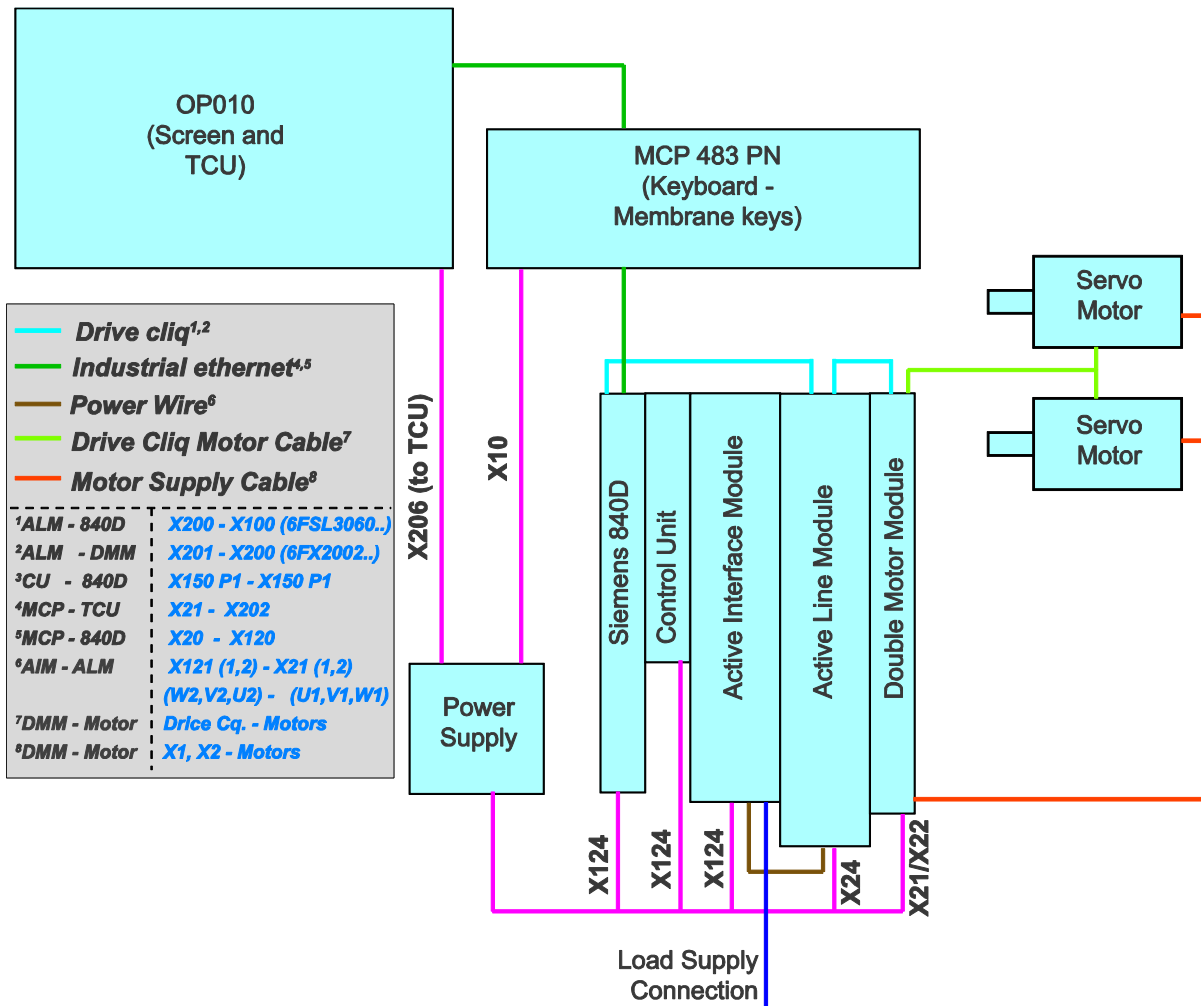Fig. A.1. Assembled Siemens 840D SL controller.

OP010
(Screen and
TCU)

MCP 483 PN
(Keyboard -
Membrane keys)

Servo
Motor

Servo
Motor

Drive cliq[1,2]
Industrial ethernet[4,5]
Power Wire[6]
Drive Cliq Motor Cable[7]
Motor Supply Cable[8]

[1]ALM - 840D	X200 - X100 (6FSL3060..)
[2]ALM - DMM	X201 - X200 (6FX2002..)
[3]CU - 840D	X150 P1 - X150 P1
[4]MCP - TCU	X21 - X202
[5]MCP - 840D	X20 - X120
[6]AIM - ALM	X121 (1,2) - X21 (1,2)
	(W2,V2,U2) - (U1,V1,W1)
[7]DMM - Motor	Drice Cq. - Motors
[8]DMM - Motor	X1, X2 - Motors

X206 (to TCU)

X10

Siemens 840D

Control Unit

Active Interface Module

Active Line Module

Double Motor Module

Power
Supply

X124

X124

X124

X24

X21/X22

Load Supply
Connection

Fig. A.2. Connection topology.

There are four main modules, produced by Siemens, to actuate the servo motors (Figure 1).

1- *Siemens 840D SL or the Numerical Control Unit (NCU):* Combines HMI, PLC, closed-loop position control, and communication tasks. Up to 8 axes can be implemented and the number of controllable axes can be expanded by using other Siemens modules, such as NX or Control Unit (CU) modules.

2- *Active Interface Module (AIM):* Contains line reactors, low-frequency/switching frequency filters, line filters etc.

3- *Active Line Module (ALM):* This module generates DC voltage in the DC link from the 3 phase line supply voltage.

4- *Double Motor Module (DMM):* This module provides power to connected motors with the connection of DC link to the active line module.
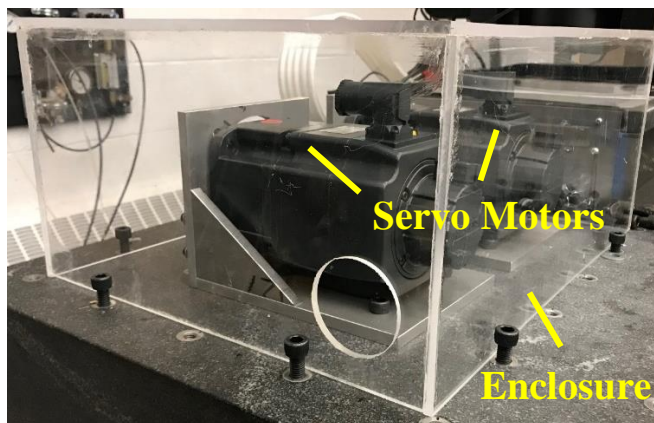
119

Fig. A.3. Assembled controller modules.

Fig. A.4. Servo motor and its enclosure.